COOLING THE CENTER-OF-MASS MOTION OF A DIAMOND NANOCRYSTAL IN A MAGNETO-GRAVITATIONAL TRAP

by

Jen-Feng Hsu

B.S. in Physics, National Central University, 2006

M.S. in Physics, University of Pittsburgh, 2010

Submitted to the Graduate Faculty of

the Kenneth P. Dietrich School of Arts and Sciences in partial fulfillment

of the requirements for the degree of

Doctor of Philosophy

University of Pittsburgh

2016

UNIVERSITY OF PITTSBURGH

KENNETH P. DIETRICH SCHOOL OF ARTS AND SCIENCES

This dissertation was presented

by

Jen-Feng Hsu

It was defended on

July 29th 2016

and approved by

Brian R. D'Urso, Ph.D., Department of Physics and Astronomy

Andrew Daley, Ph.D., Department of Physics, University of Strathclyde

Maarten P. de Boer, Ph.D., Department of Mechanical Engineering, Carnegie Mellon University

M. V. Gurudev Dutt, Ph.D., Department of Physics and Astronomy

Michael Wood-Vasey, Ph.D., Department of Physics and Astronomy

Dissertation Director: Brian R. D'Urso, Ph.D., Department of Physics and Astronomy

ABSTRACT

COOLING THE CENTER-OF-MASS MOTION OF A DIAMOND NANOCRYSTAL IN A MAGNETO-GRAVITATIONAL TRAP

Jen-Feng Hsu, PhD

University of Pittsburgh, 2016

A magneto-gravitational trap for micro/nanometer sized diamagnetic particles, such as diamond nanocrystals, is tested and characterized. After exploring various other systems, such as a suspended graphene beam and an optical trap, this magneto-gravitational nanomechanical trapping system for diamond with nitrogen-vacancy (NV) centers presents unique advantages for experiments in fundamental quantum mechanics. Those include, for example, the generation of large quantum superposition states and tests of quantum gravity. Features are demonstrated for this system, such as stable and passive levitation from atmospheric pressure to high vacuum, low resonant frequencies and damping rates, and cooling of the center-of-mass motions to below 1 K. The construction of the trap, vacuum system, optics, and motion detection electronics are described in detail.

Keywords: Magnetic trapping, nanomechanical oscillator, feedback cooling, quantum ground state, and diamond nanocrystal.

TABLE OF CONTENTS

LIST OF TABLES

LIST OF FIGURES

PREFACE

This Ph.D. study has been a journey of knowing myself better, including my limits, weaknesses, and sometimes surprises to myself. It is also a journey of learning good physics and knowing good physicists.

Along the road, I am very grateful for many many physicists and friends with great advise and encouragement. Thank you, Professor Sasha Tikhonov, Professor Chih-kuan Tung, Professor Hsuan-Yi Chen, Professor Hsiang-nan Li, Professor Yi Yang, Dr. Xiaopeng Li, Dr. Dan Qu, Dr. Chungwei Lin, Dr. Fei Yan, Dr. Yung-Chang Lin, Dr. Zhititng Li, and Dr. Fangyong Yan.

Professor Wolfgang Choyke has very kindly blessed our lab and my experiment with many valuable vacuum parts, equipment, and materials, including the main chamber in which the experiments were performed. On top of those, I am very grateful for his helpful advise.

The Physics and Astronomy administrative staff are always helpful, and I am especially thankful to Leyla Hirschfeld, Laura Provolt, Beth Dummer, Caitlyn Hunter, Lou Lane, and Bob Breze.

The machinists in of The Dietrich School Machine Shop provided tremendous machining help to my study. Thank you, Tom Gasmire, Shawn Artman, Josh Byler, Jeff Tomaszewski, Bill Strang, and Jeff Sicher. Also, Lori Neu of the Glass Shop made several beautiful and useful glass pieces for the my study.

Special thanks be to collaborators on the graphene project, which have produced nice results: Professor Jeremy Levy, Dr. Giriraj Jnawali, Dr. Mengchen Huang, Shivendra Tripathi, Arthur Jianan Li, Qing Guo, and Lucy Lu Chen.

I would like to thank all my lab mates and friends who have laughed and mourned with me, and have put up with me: Dr. Shonali Dhingra, Dr. Elliot Jenner, Charlie Lewandowski, Brad Slezak, Peng Ji, Stephen Hemmerle, Mia Rossi, Fan Yang, and Chris Bracken.

My dissertation committee members probably have gone through more annual review meetings

than many others. I thank them, Professor Brian D'Urso, Professor Andrew Daley, Professor Maarten de Boer, Professor Gurudev Dutt, and Professor Michael Wood-Vasey, for being patient, helping me clarify my own reasonings, improving my presentation skills, and providing insights.

Of course my adviser, Professor Brian D'Urso, who provides experimental help, theory guidance, Pythics techsupport, cooking recipes, home plumbing tips, carrier advise, babycare consultancy, and, most importantly, as far as this dissertation concerns, a role model of an excellent physicist and engineer (no slightest disrespect intended.) Of course my adviser, Professor Brian D'Urso, who provides experimental help, theory guidance, Pythics techsupport, cooking recipes, home plumbing tips, carrier advise, babycare consultancy, and, most importantly, as far as this dissertation concerns, a role model of an excellent physicist. He drives me to think in a broad, leaping, and strategic manner and to have an optimized management of time and resources. So, I really can not thank him enough. Beyond this dissertation, he is a gentle and smart friend, really smart. Also, Kelly D'Urso's wonderful cookies in the lab always provide enough sugar for me to work for a little longer.

Thanks be to my parents and family members, for they are always supportive and encouraging. Without them I would not have started at all.

I thank my PCCO brothers and sisters, especially the Sweeties, for your support and prayer through these years.

Thank you, my dear wife Fei, as we walked together through our first married years while doing this dissertation work. I know in the future we will have so much of these years to talk and laugh about.

Thanks and glory be to my Lord, for you see me through.

1.0 INTRODUCTION

Physics is the study of why objects move (or accelerate) and why they stay still. The formulation founded by Newton says that a net force results in acceleration. A constant force, such as gravity pulling down near the surface of the earth, results in a constant acceleration and runaway motion. The next simplest force is a linear one in position, and beyond which the problem gets much harder.

A linear force results in a simple harmonic oscillator system, characterized by its amplitude, frequency, and phase. However, realistically, the system suffers energy loss due to damping, which modifies the resonant frequency and decreases the amplitude over time. In addition to non-conservative forces, such as damping, another non-conservative force can add energy into the system over time, which is called driving.

It is much more interesting to ask why or how objects stay still in the quantum regime than in the classical. There is no absolute stillness for a harmonic oscillator, since it posses a minimum amount of energy that can not be removed, or cooled.

This dissertation work pursues removing energy from a mechanical harmonic oscillator system, with the intermediate-term goal of reaching the quantum ground state of the harmonic oscillator. This work fits in the overall scope of physics research to prepare a harmonic oscillator in a well-defined quantum state, and to facilitate interactions between this degree of freedom to the other. In the system presented here, accessible other degrees of freedom include a nitrogen-vacancy (NV) defect center from diamond, harmonic oscillators from the other two directions, and an added optical cavity.

1.1 MOTIVATION

In recent decades, extending quantum mechanics to the macroscopic level has been a main goal of many physicists and engineers. Especially now, this is a time that the physicists are getting closer [2, 3] to preparing a superposition of microscopically distinguishable states of a mechanical oscillator. A Schrödinger's cat [4], which was originally presented to rebuke the idea of superposition of quantum states, is a macroscopic object (cat) in a superposition of two distinguishable states (live and dead.) This is the reason for an exciting time. The first motivation is the simple curiosity of seeing if there is a size limit to which quantum mechanics still applies. Additionally, once prepared in a well-defined quantum state, other fundamental quantum experiments can be performed based on this system. The experiments include, but are not limited to, large superposition [5, 6] (Schrödinger's cat) and quantum gravity [7, 8] by testing the decoherence due to gravity. Finally, a great amount of research effort is to use quantum mechanics, specifically the superposition of states, to make a tremendous boost of computation speed in quantum computers [9]. The core element for quantum computation is, of course, a quantum bit, or qubit. The focus of current research along this line is to build such robust qubit against decoherence, which is the loss of quantum superposition due to interaction with the environment [10, 11].

With the above motivation, this dissertation work aims to provide a new and viable implementation of a well-behaved mechanical oscillator system for experiments such as quantum ground state preparation and Schrödinger's cat generation.

1.2 OTHER SYSTEMS

In a very broad sense, many research projects have studied the interaction between a quantum system, e.g., a spin or a cavity and a mechanical system, either classical or quantum [12, 13, 14, 15, 16, 17, 18]. Among those, efforts are put into cooling a harmonic oscillator down to near the ground state [19, 20, 21, 22, 23, 24, 25, 26]. Loosely related, the Laser Interferemeter Gravitational-Wave Observatory (LIGO) detects a mechanical motion due to gravitational waves

that is comparable to the quantum mechanical wave packet [27, 28, 29].

In efforts to suppress decoherence, extreme isolation from the surrounding environment makes optically trapped particles in vacuum an attractive system towards mechanical systems in the quantum regime [30, 31, 32]. If the trapped particle is a diamond nanocrystal with nitrogen-vacancy (NV) defect centers, the spin of the NV centers can be manipulated [33] to provide a quantum handle into the system. The spin state can be used to alter the magnetic moment of the trapped particle and spectroscopy on spin transitions can measure the local magnetic field [34, 35]. A diamond nanocrystal with NV centers levitated in an optical trap has been proposed as a platform for experiments to generate macroscopic superposition (Schrödinger's cat) states [5, 6] and to test quantum gravity [8, 7].

Trapping in vacuum is critical for decreasing the natural damping of the mechanical motion and opening the possibility of cooling the mechanical motion to near the quantum ground state. However, there is a gap in experiments with optically trapped diamond nanocrystals: trapping at high vacuum has not been demonstrated, although multiple experiments show diamond nanocrystals trapped at higher pressures [36, 37]. Recent evidence shows that some nanodiamonds burn or graphitize in an optical trap whenever the pressure is less than 10 Torr [38], providing a likely explanation for the challenge of high vacuum trapping. While it may be possible to reduce the absorption of the trapping laser by using higher purity nanodiamonds, a more robust solution would be to levitate nanodiamonds with an alternative trap which does not require high intensity oscillating electromagnetic fields.

1.3 THE SYSTEM

In this dissertation work, the use of a combination of static magnetic field gradients and gravity for stable trapping of a diamond nanocrystal cluster in high vacuum is demonstrated. The weak diamagnetism of diamond provides the force needed to levitate the nanodiamonds [39]. Unlike previous experimental studies of systems with diamagnetic levitation [40, 41, 42, 43], trapping in vacuum is demonstrated, the harmonic center-of-mass motion of trapped particles is characterized, and the motion is cooled by up to a factor of 490 using position detection

and feedback. In contrast with other proposed quantum magnetomechanical systems [24, 23], superconducting particles for levitation is not required. The diamagnetism of many common materials, such as diamond, is adequate for levitation with a strong magnetic field gradient. Since the trap utilizes only static fields, there is no intrinsic heating of the particle, making it an attractive alternative to optical traps. The low stiffness and large size scale of the trap (relative to optical traps) result in low oscillation frequencies of 10 to 150 Hz, which makes the detection simple. For example, the motion of a particle when equilibrated at ambient temperature in the trap can be easily observed and recorded with a high-speed camera.

1.4 CONTRIBUTIONS BY THIS DISSERTATION WORK

The major contribution of this dissertation work in the field of quantum nanomechanics is the establishment of the magneto-gravitational trapping technique. This technique, as reported [44], achieved trapping of diamond nanocrystals in high vacuum for the first time among all trapping techniques. Mass calibration and cooling of the center-of-mass motion of a trapped diamond nanocrystals were also reported. The lowest recordable effective temperature is 600 mK, cooled from room temperature, 295 K.

A few other mechanical systems as approaches towards quantum nanomechanics were also explored and reported by the author. These include suspended graphene devices [45] and optical trapping [46].

Many necessary techniques developed for preparing these mechanical systems were also significant and publishable, including graphene synthesis on ultra-flat copper [47] and a cost-efficient mirror galvanometer system [48]. The graphene synthesized and transferred partially by the author were used in other research projects through collaboration and generated a few publications as well [49, 50, 51].

1.5 STRUCTURE OF THIS DISSERTATION

The chapters of this dissertation are arranged as follows.

Chapter 2, first tours the lab space where the experiments are carried out, laying out all the relevant vacuum chamber, pumps, optics, and electronics that support this study.

Chapter 3 then describes and analyzes the core technique of magnetic trapping. Loading procedures and various concerns are also summarized here.

Chapter 4 covers the standard and non-standard optics and electronics techniques to obtain signals from the trapped particle. Full data analysis for the motion and cooling can be found here.

Chapter 5 examines the most important physics question of this study – what this system would look like in a quantum state, and how to get there.

Chapter 6 recapitulates the alternative approaches to a quantum nanomechanical system that have been explored prior to the magneto-gravitational trapping. Those include graphene clamped devices, optical trapping, and optical trapping-related techniques.

Chapter 7 briefly summarizes the work done and prioritizes future directions for improvement in order to approach the quantum ground state and beyond.

Appendix A and Appendix B are supplementary details for calculations.

Appendices C to F contain all relevant lab technique or design files, in the hope that this study can be reproduced with ease.

2.0 OVERVIEW OF THE EXPERIMENT SYSTEM

This short chapter displays the lab setup where the the actual experiments being performed. It elaborates the ground-level vacuum, optics, and electronics needed to support this dissertation study.

2.1 EXPERIMENT VACUUM FACILITY

2.1.1 Experiment Vacuum Chamber

A large bell-shaped vacuum chamber with numerous ConFlat-sealing ports is used to host the trap and all the experiments. This chamber is called the main chamber hereafter, as shown in Fig. 1(a). The wide opening at the bottom of the chamber converts to a 8" tube going through an 18" by 18" hole in the optics table, and to the vacuum pump line underneath the table.

This chamber is a generous gift from Prof. Wolfgang Choyke at University of Pittsburgh. He and his graduate student originally designed this chamber for a semiconductor material study with the radiation beam from the Van de Graaff accelerator at University of Pittsburgh [52], but has been modified to fit the needs of this dissertation work. The ports usage is laid out in Fig. 2.[1] The most important ports are the ones for optical accesses, both illumination input and scattering light output from the trapped particle.

To minimize the distortion an vacuum glass window introduces, the largest ports with 8" ConFlat seals are chosen for the optical access. Also, there are two such large ports that are oriented 90 degrees from each other. While the experiment design of this dissertation work

[1] Parts of Fig. 2 and Fig. 3 and are reproduced from Robert M. Wallace's Ph.D. dissertation [52].

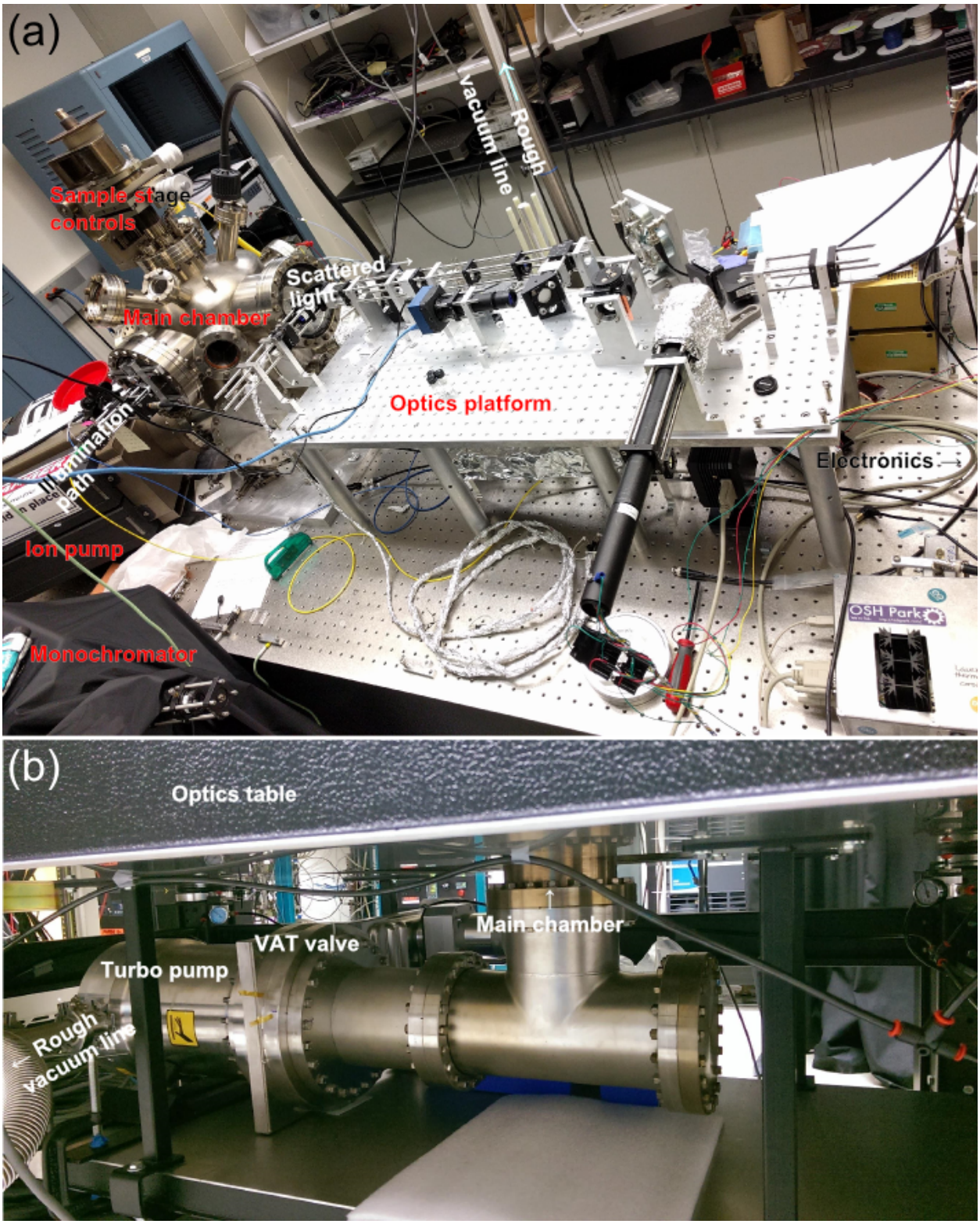

Figure 1: The full view of the experiment system (a) above the optics table and (b) underneath the table.

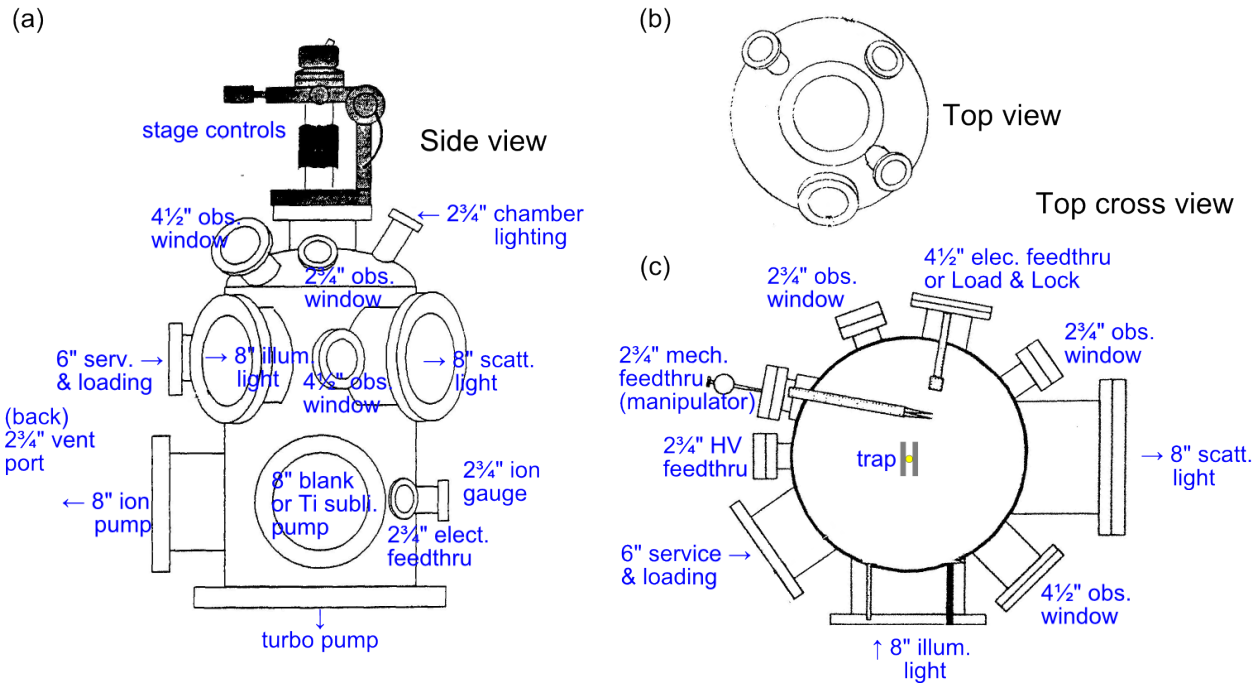

Figure 2: (a) The side, (b) top, and (c) top cross-sectional views of the main chamber.

requires the illumination path and the scattered light collection path to be perpendicular to each other, the port arrangement of this chamber fits the design very well.

The 6" port is chosen to be the service and loading port, and every task and object inside the main chamber is through this port. Those include mounting optics and the trap assembly on the stage, making electric contacts from the feedthroughs, loading droplets, and pre-neutralizing the charges on the droplets.

Three electric feedthroughs are installed, one over a $4^1/_2''$ port and two in $2^3/_4''$ ports. One of the $2^3/_4''$ feedthrough is a specialty high voltage (HV) one with ceramic insulations. The field emission point, which requires voltages up to 2 kV, is a dominant user of the feedthrough. The rest of the electric connections, including feedback drive, pole pieces biasing, and the heater share the other two feedthroughs, depending on the convenience of the location. As seen in Fig. 2(a) and 2(c), there are plenty of observation windows, primarily of glass, at various angles. One of them is used to flood light in the chamber from a lamp outside when aligning or mounting. One

other electric contact is for the thermal couple temperature monitoring, which is through a $1^1/_3''$ port attached to the 6" stage control flange.

Mechanical access, other than the 6" service and loading port, is available through the manipulator. It is particularly useful if manipulation under vacuum is desired, such as moving a radioactive source closer after pumping down. A load-and-lock is also available if replacing the $4^1/_2''$ electric feedthrough.

The most important mechanical access is, of course, the stage movement. Figure 3 shows the detailed drawings of the sample stage movement controls from outside of the main chamber. In addition to three translations at micrometer resolution, there are sample spinning (about sample axis that is perpendicular to the stage surface), rotation (about the stage long axis), and the tilting of the stage long axis. The length of the actual sample stage is 32 mm. These degrees of freedom provide an abundance of trap manipulation capability.

As can be seen, this large chamber and and number of vacuum ports grants great flexibility for adding new electronics or vacuum pumps. Therefore, this is an ideal chamber to be used in exploratory experiments.

2.1.2 Vacuum Pumps and Gauges

Several vacuum generating pumps and pressure measurement parts are employed in this work, for various vacuum levels from 10^{-2} to 10^{-8} Torr. Proper valvings are implemented in several places as well, for experiment controls.

2.1.2.1 Pumps Because the main chamber is large, a large volume of air molecules must be evacuated for vacuum applications. The team of pumps that does this work starts from a rough vacuum line connected to the system through a turbomolecular (turbo) pump underneath the optics table (Fig. 1). The vacuum in the shared roughing line is sourced from a dry pump (Edwards QDP 40) in another room. Ultimately the rough vacuum is as good as approximately 5 mTorr.

In-line with the rough vacuum, a turbo pump (TG1110EM, Osaka Vacuum, with power supply TD700/1100) with 1100 L/s (nitrogen) is installed to facilitate vacuum down to about

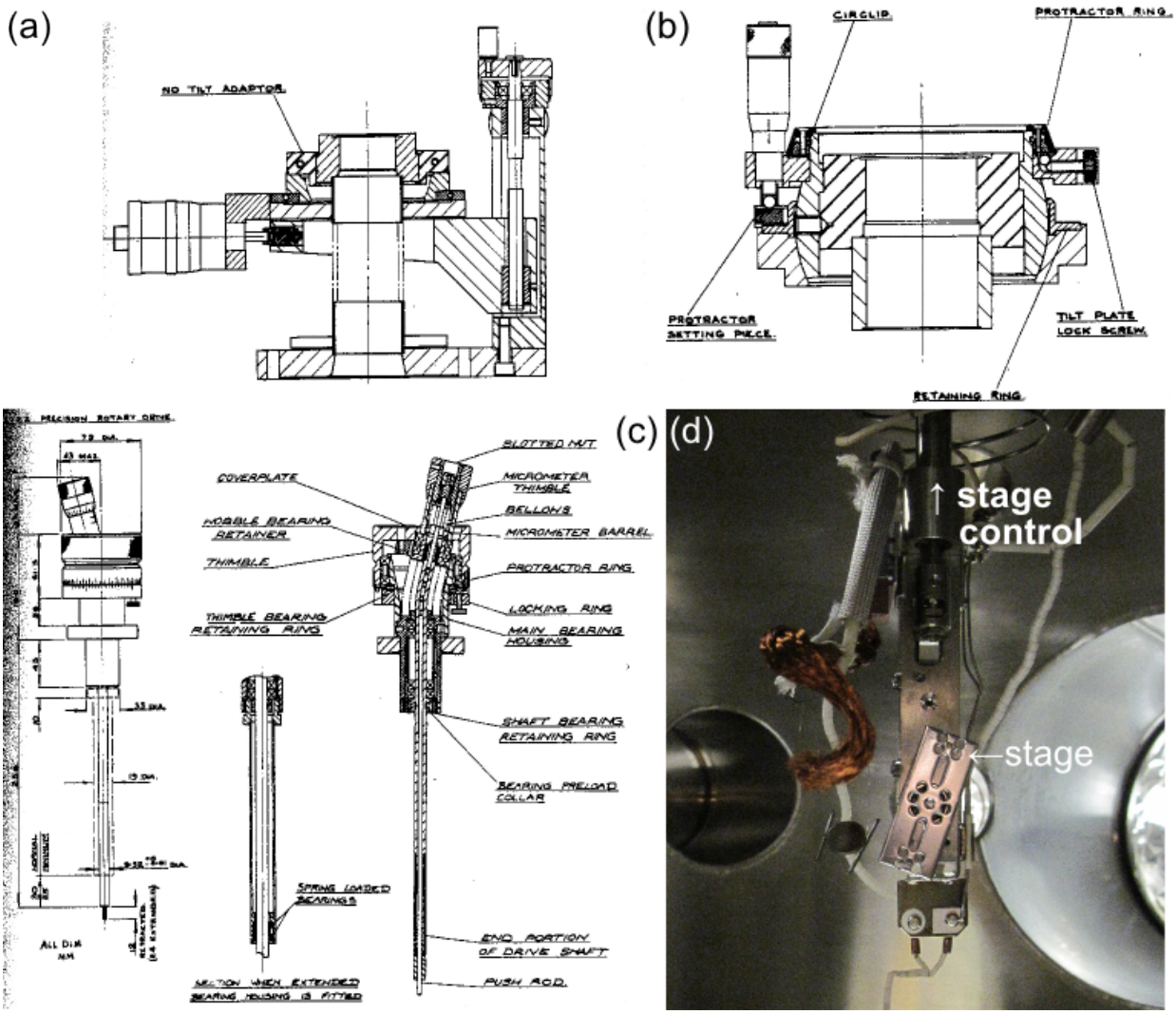

Figure 3: (a) and (b) are the design drawings of the sample stage graduated controls, showing all three knobs for translation. (c) shows the rotation and spinning control mechanisms. (d) is a photograph of the sample stage in side the chamber. The stage is spun.

5×10^{-8} Torr. See Fig. 1(b) However, in effort to incorporate this large pump the vacuum chamber had to be extended, so that the total volume of the system is very crudely estimated to be at the order of 100 L. The turbo pump relies on a good backing pressure from the rough pump to rotate up to speed.

The next pump is an ion pump (with Varian controller 920-0066) through a 8" port (Fig. 2). Ion pump is useful due to lack of vibration and this one was tested to give about a factor of two improvement to bring the vacuum down to 2.8×10^{-8} Torr.

2.1.2.2 Gauges

There are four vacuum gauges attached to the main chamber:

1. A convectron gauge covers the vacuum reading from atmospheric pressure to about 1 mTorr.
2. A cold cathode gauge, working from 10 mTorr to about 10×10^{-8} Torr.
3. A hot cathode gauge, or ion gauge, working from 10×10^{-4} to 10×10^{-9} Torr.
4. A baratron (627A, MKS) is calibrated from 1 to 50 mTorr, for data analysis.

One thermal couple gauge is attached to the back of the turbo pump, in order to monitor the backing pressure while the turbo is running.

2.1.2.3 Valves

Valves are added at various stages along the vacuum line, for ease of control:

1. A metal valve, sharing the same port for the convectron gauge, is attached to a $2^3/_4''$ on the main chamber for venting.
2. A valve can close from the rough vacuum line.
3. There is a 10" VAT valve right in front of the turbo pump (Fig. 1), in case of some operations requiring higher pressures in the main chamber, e.g., thermalization of the particle at high pressures.

2.1.3 Vibration Noise Control

All the mechanically linked parts, including the trap, main chamber, ion pump, and turbo pump are mounted on a optics table. Therefore, outside vibration noises should be damped down. However, the link between the sample stage and the control through the long axis is a little weak, might be susceptible to some "dangling."

2.2 OPTICS

Since the lens being used as the objective has a very short working distance (< 2.75 mm), it has to be inside the main chamber. The challenge now is integrating the optics in or around the chamber, with HV or UHV compatible materials only.

For the scattering light path, where the objective is in, a spider structure holding cage plates is built to establish a cage optics system in that path. The feet are made of polyether ether ketone (PEEK), a strong, UHV-compatible polymer that can tolerate up to 250° C. They stretch and span the inner tube of the 8" vacuum port for mechanical stability. See Fig. 4(a) for those in the scattering light path. A piece similar to an optics cage plate links all the feet and can hold four cage rods. The centering of the plate can then be adjusted by the threads to the feet.

The objective in a custom-made holder is mounted on a like-wise custom-machined stainless steel tip-tilt mount (replicated from a Thorlabs KC1-T), and it is in turn mounted on the in-chamber cage structure. See Fig. 4(b) for the lens holder, tip-tilt mount, and the cage system in the main chamber.

An optics platform (Fig. 1(a)) is designed and built on top of the optics table, matching the height of the light coming out of the chamber.

Figure 4(c) shows the solution for the illumination light optics integration. A sliding rail system is attached to the 8" flange. This provides a flexibility to follow the exact position of the trap.

A complete map of the optics elements can be found in Fig. 20.

2.3 ELECTRONICS

2.3.1 Outside of the Main Chamber

There are several pieces of electronics, customized or bought off-the-shelf, to aid in the experiment control and data acquisition. The off-the-shelf parts include diode current suppliers (LDC 205C or higher, Thorlabs), gauge controllers (146, MKS and senTorr, Varian), VAT valve controller,

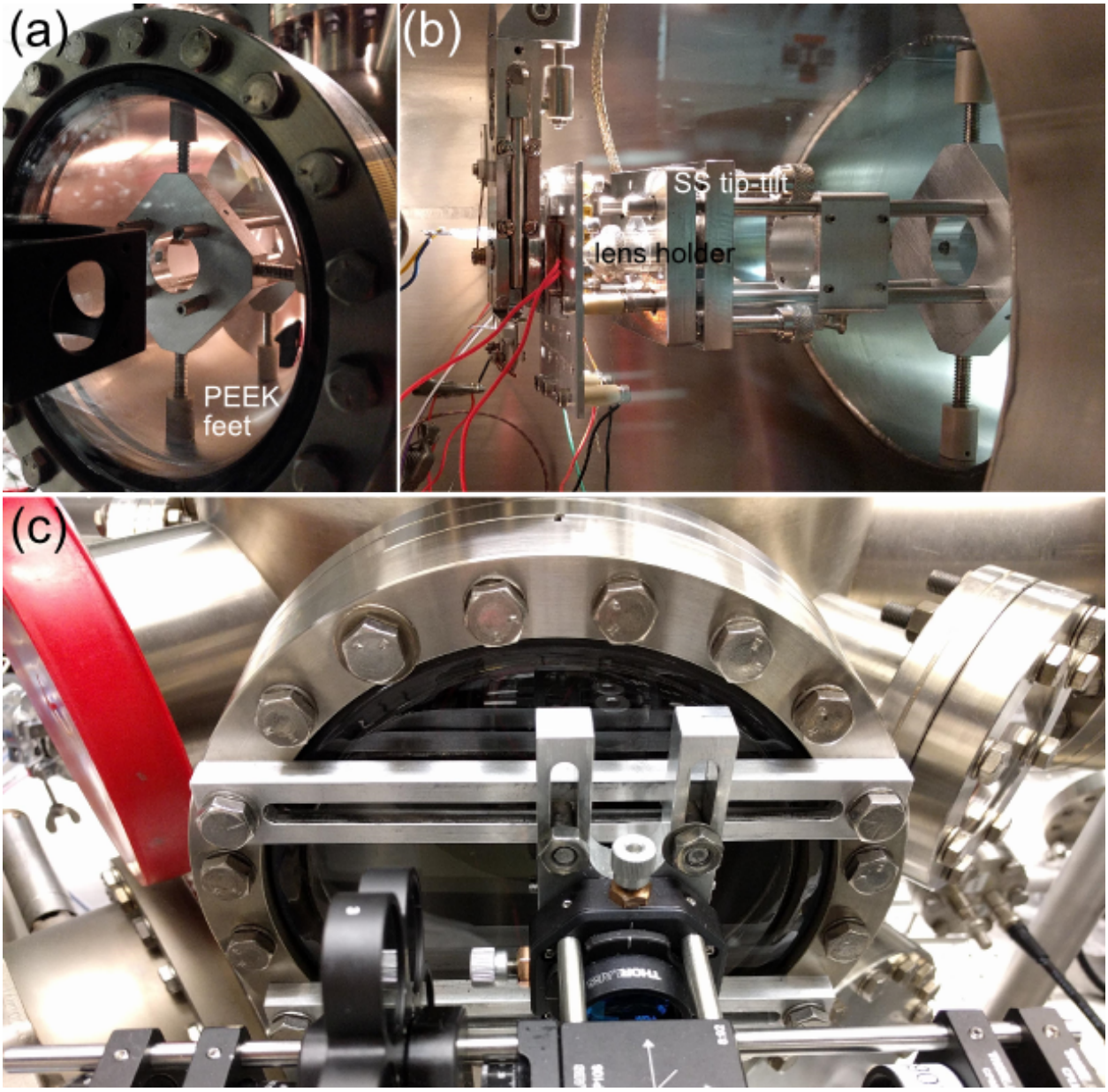

Figure 4: (a) The infrastructure for holding cage rods inside the main chamber with PEEK feet. (b) The objective and tip-tilt assembly inside the main chamber. (c) Axial illumination optics setup.

turbo pump controller (TD700/1100, Osaka Vacuum), ion pump controller (920-0066, Varian).

The custom-made electronics, analog or digital, include the position-sensitive detector amplifier, filters, feedback drive, spectrum analyzer, galvo mirror control, synchronized scanning, photon counter, thermal electric laser cooler. The details of those shall be elaborated in later chapters or appendices. Unless otherwise specified, the power is sourced from shared ± 18 V supplies (A18H1400, Acopian). While the off-the-shelf boxes are a little harder to communicate with a computer, most custom-made electronics are controlled through a microcontroller board Arduino DUE, and eventually a python-based graphical user interface Pythics [53].

2.3.2 Inside the Chamber

The pieces and functionalities of the electronic devices inside the chamber and around the magnetic trap will be elaborated in later chapters. Therefore, only the basic construct is described.

Again for UHV compatibility, the options of construction materials are much limited. Ceramic standoffs (94335A115 and 94335A110, McMaster) isolate any live voltage from the base aluminum trap plate (Fig. 4. The wires running on the standoffs are either bare metal, kapton insulated (Accu-Glass), or teflon (PTFE) insulated (Omega), as other regular jacket materials tend to outgas under vacuum. Most wires connecting from the trap plate to the electrical feedthroughs are PTFE insulated.

3.0 MAGNETIC TRAPPING

The core of this dissertation work, the magneto-gravitational trapping, is described in detail in this chapter. Trapping techniques that work in vacuum are first surveyed and summarized. Magneto-gravitational trapping is then conceptually described. A multipole expansion study for the trap geometry in this work is presented. The actual design and manufacturing of the trap pole pieces are reported. Finally, the technique of loading nanodiamonds into the trap with sacrificial liquid is presented.

3.1 SURVEY OF TRAPPING TECHNIQUES IN VACUUM

3.1.1 Penning Trap

A penning trap consists of a strong homogeneous static magnetic field and a weak electrostatic quadrupole field [54, 55, 56]. This trap is used for an ion or a single electron. It relies on the Lorentz force, $q\left(\vec{E}+\vec{v}\times\vec{B}\right)$, as a restoring force. Therefore, the particle must be charged to be trapped. While the other two degrees of freedom can be stably trapped, the magnetron motion is only metastable, i.e., the trapped particle will eventually decay out radially, though over a time longer than any relevant scale. Most importantly, it is not clear if the trapping condition can be extended to a mesoscopic object, e.g., a $\sim$1 μm sphere.

3.1.2 Paul Trap

A cylindrical Paul trap can be defined by a grounded cylindrical wall with caps at an oscillating potential (~ 1500V), generating an electric quadrupole field with high amplitude [57, 58]. The

electric field oscillation frequency depends on the charge-to-mass ratio of the trapped particle.

The linear variation of the Paul trap is defined by four linear electrodes and two endcap electrodes. This configuration is widely used in ion trap experiments [59, 60].

Attempts have been made to adopt a Paul trap to trap silica (3 μm diameter) beads for mechanics experiments, such as in [61]. What has been found is that the required electric field oscillation frequency is around 1.5 kHz, very close to the mechanical oscillation frequencies, which interferes with the cooling of the motion. Also, similar to an optical trap, the oscillating nature of the trap fields means energy is added to the trapped particle and can cause excessive heating.

3.1.3 Optical Trap

A pure optical trap uses the gradient force of a focused laser beam on a dielectric particle as a restoring force [62, 63, 64]. A side effect from a particle near the laser focus is heating of the particle and the air molecules around it. This introduces another trapping mechanism of photophoretic trapping, which is, strictly speaking, not an optical effect [65, 66, 67, 68]. This effect finds some applications in ambient pressure [69, 70, 71, 72, 73]. But as the mean-free-path of air molecules increases with the decrease of the pressure, the photophoretic force or thermal force changes quickly in a complicated way, and eventually the trapping force vanishes due to lack of surrounding air molecules.

There are quite a few research groups employing a pure optical trap as an approach to quantum nanomechanics, for nanodiamonds in partial vacuum or silica beads in high vacuum [74, 32, 75, 76, 77]. Recent results may explain the barrier to trapping nanodiamonds in high vacuum: The diamond, due to its absorption, might be burning or graphitizing [38].

Therefore, to pursue trapping nanodiamonds in high or ultra-high vacuum as a quantum nanomechanics system, there has to be an alternative for trapping.

3.1.4 Ioffe-Pritchard Trapping

An Ioffe-Pritchard uses static magnetic fields to trap atoms with the magnetic moments that are antiparallel to the trap field. The trap can be defined by two "pinch coils," forming a Helmholtz-like configuration, and four "clip coils." The original design and variations can be found in the

bibliography [78, 79, 80, 81, 82, 83]. When DC currents run through the coils, there is a quadratic field and a homogeneous field in the axial direction, and an energy minimum is formed at the center for atoms with the correct magnetic moment orientation. Therefore, this trap works for neutral atoms, too. However, the trap field generated by the currents might not be strong enough for diamagnetic bulk materials this dissertation is interested in. Furthermore, the magnetic field at the trap center is not zero, and is nowhere zero. This could cause problems for spin-related experiments, including applications involving nitrogen-vacancy (NV) in diamond.

3.1.5 Quadrupole (Anti-)Magnetic Trapping

Seeing the heating nature of an optical trap, the focus of this work has then turned to a static and passive trap. However, Ernshaw's theorem rules out the possibility of a static electromagnetic field maximum in freespace [84, 39]. This means that trapping for strong-field seekers is not possible, and all materials with positive electric or magnetic susceptibilities would have no chance. While negative-electric-susceptibility materials do not exist, diamagnetic materials have a negative magnetic susceptibility. Despite the weakness of the effect ($|\chi| \sim 10^{-5}$), diamagnetic levitation for various materials, including a frog, has been demonstrated [39, 40].

A special case for magnetic trapping is superconducting materials, which, by definition, has magnetic susceptibility of -1. Proposals are already made for quantum ground state cooling of magnetically trapped superconducting spheres [24, 23], superconducting particles.

3.2 MAGNETO-GRAVITATIONAL TRAPPING

In this dissertation work, a hybrid trap of magnetic and gravitational forces is designed. The confinement in vertical and transverse directions is defined by a linear quadrupole magnetic field configuration, produced by two permanent magnets and four magnetic pole pieces. The symmetry in the axial direction is intentionally broken to allow gravity to pull the particle back to the center of the trap, resulting in the axial confinement. See Fig. 5 for an illustration of the trap design. The detail of the trap design is presented in Sec. 3.4.

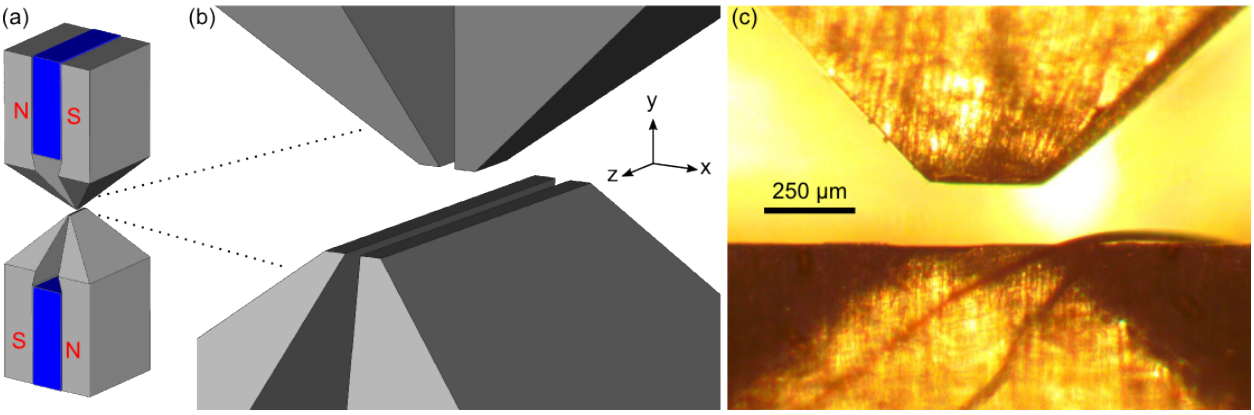

Figure 5: (a) Illustration of the trap design and (b) a zoom-in view. (c) Microscopic image of the trap along the y axis.

3.3 MULTIPOLE EXPANSION OF TRAP POTENTIAL

To gain better insight of the trap geometry and to make it easier for future theoretical modeling, a multipole expansion of the trap potential is described. Starting with the symmetry properties of the trap, a few spherical harmonics are picked to expand the trapping magnetic potential. Since there are three measurable quantities once a particle is trapped in the system, i.e., the center-of-mass (CM) oscillation frequencies in all three directions, three spherical harmonics are chosen. At the end of the calculation, observed CM oscillation frequencies are used to solve for the coefficients of each term. Afterwards, the magnetic fields derived from the determined potential can be plotted against the finite-element calculation result of teh actual trap configuration. The results showed that this comparison is satisfactory, proving that the choice of spherical harmonics according to the symmetry is effective.

3.3.1 Coordinate System Convention

The following coordinate axes definitions are used (consistent with the axes designation in Fig. 5):

- z-axis: "Axial", the side illumination axis (light towards $+z$.)
- y-axis: "Vertical", gravitation towards -y.

- x-axis: "Transverse", scattered/photoluminescence light towards -x.

3.3.2 Spherical Harmonics

The following are the relevant spherical harmonics for the expansion:

$$Y_{2,-2}(\theta,\phi) = \frac{1}{4}\sqrt{\frac{15}{2\pi}}\sin^2\theta e^{-2i\phi} \tag{3.1}$$

$$Y_{31}(\theta,\phi) = \frac{-1}{8}\sqrt{\frac{21}{\pi}}\sin\theta\left(5\cos^2-1\right)e^{i\phi} \tag{3.2}$$

$$Y_{4,-4}(\theta,\phi) = \frac{3}{16}\sqrt{\frac{35}{2\pi}}\sin^4\theta e^{-4i\phi} \tag{3.3}$$

Using the relationship Eq. (3.54) [85]

$$Y_{l,-m}(\theta,\phi) = (-1)^m Y^*_{l,m}(\theta,\phi), \tag{3.4}$$

real spherical harmonics (as opposed to complex) can be formed by taking the combinations of positive and negative m. Furthermore, these spherical harmonics can be re-written in Cartesian coordinate variables using the relationships

$$\cos\theta = \frac{z}{r} \tag{3.5}$$

$$\sin\theta = \sqrt{1-\frac{z^2}{r^2}} \tag{3.6}$$

$$e^{i\phi} = \frac{x}{r\sin\theta} + \frac{iy}{r\sin\theta}. \tag{3.7}$$

Since the trap assembly follows the Cartesian (rectangular) coordinate system, the following real spherical harmonics in Cartesian coordinates are the ones used in the expansion of the trapping potential:

$$RY_{2,-2}(x,y,z) = i\sqrt{\frac{1}{2}}\left(Y_{2,-2}-Y_{22}\right) = \frac{1}{2}\sqrt{\frac{15}{\pi}}\frac{xy}{r^2}, \tag{3.8}$$

$$RY_{31}(x,y,z) = \sqrt{\frac{1}{2}}\left(Y_{3,-1}-Y_{31}\right) = \frac{1}{4}\sqrt{\frac{21}{2\pi}}\frac{x(4z^2-x^2-y^2)}{r^3}, \tag{3.9}$$

$$RY_{4,-4}(x,y,z) = i\sqrt{\frac{1}{2}}\left(Y_{4,-4}-Y_{44}\right) = \frac{3}{4}\sqrt{\frac{35}{\pi}}\frac{xy(x^2-y^2)}{r^4}. \tag{3.10}$$

Figure 6 shows spherical harmonics up to $l = 4$ with all possible m.

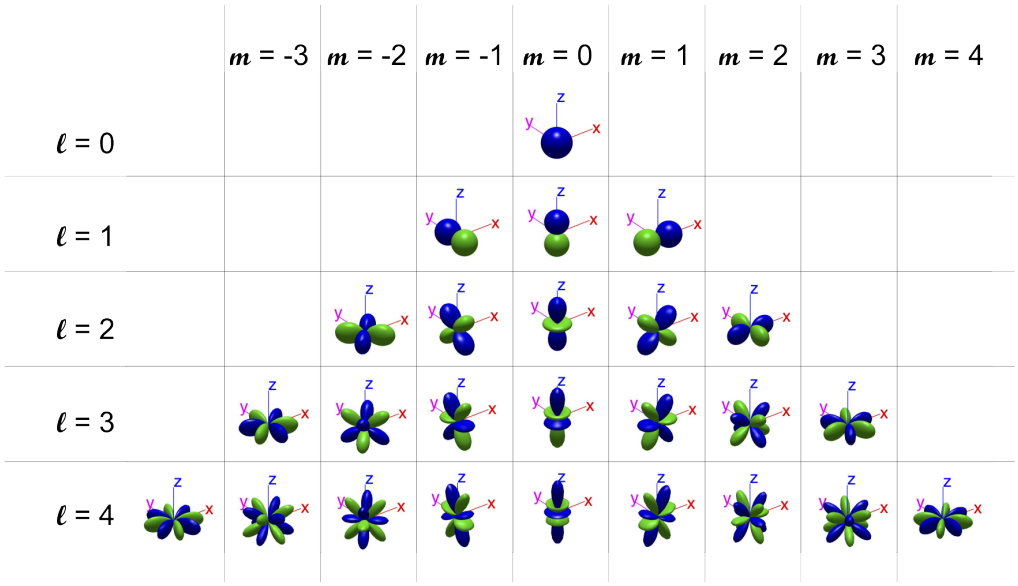

Original image: Archontis Politis
http://se.mathworks.com/matlabcentral/fileexchange/43856-real-complex-spherical-harmonic-transform--gaunt-coefficients-and-rotations

Figure 6: Spherical harmonics from $l = 0$ to $l = 4$. [1]

3.3.3 Symmetry Justification for Choice of Harmonics

The lowest order approximation to the trap potential is a quadrupole potential, particularly $RY_{2,-2}$ in Eq. (3.8) for the specified coordinate convention of this system. The key features are zero field along the axial direction, linear in x and y, and reversing signs crossing either the x-z or y-z planes. In terms of symmetry, this requirement can be stated as being symmetric along z-axis and anti-symmetric along x- or y-axes.

Two more requirements pertain to a realistic potential approximation: distinct resonant frequencies in the vertical and transverse directions and the bounding in the axial direction.

In order to break the symmetry between the transverse and the vertical directions, a second spherical harmonic function as a small perturbation to the quadrupole term needs to be added. This is to reflect the fact that the pole pieces are not distributed with four-fold symmetry, and that they are polished flat horizontally and the top and bottom pairs are each brought closer together to increase the available numerical aperture for light collection in the transverse direction. This should be anti-symmetric in both the vertical and transverse directions, same as for the quadrupole

	Quadrupole $RY_{2,-2}$	Octupole $RY_{4,-4}$	Hexapole RY_{31}
Axial (z)	symmetric	symmetric	symmetric
Vetical (y)	anti-symmetric	anti-symmetric	anti-symmetric
Transverse (x)	anti-symmetric	anti-symmetric	symmetric

Table 1: Symmetry table for multipole moment terms.

term. However, this will add and subtract to the quadrupole term differently in the vertical and transverse directions, to result in the distinct frequencies. This one should likewise be zero along the axial direction. An octopole, $l = 4$, fits in these requirements well.

Since in the experiment the top pieces are cut shorter than the bottom pieces in the axial direction, the line of zero magnetic field curves vertically upward as z increases or decreases from zero. This brings about the confinement in the z direction. A potential that is symmetric along the z-axis is needed. However, unlike the previous two, which are mostly zero along the z-axis, this one needs to have symmetric finite values along the z-axis. This one does not alter the potential in the vertical direction, hence, one that is mostly zero in the y-axis is chosen. It shall not alter the potential in the transverse direction, hence, still antisymmetric.

From the above arguments, symmetry alone is not enough to determine the proper spherical harmonics, but largely acts a guide in the selection process.

The above symmetry requirements are summarized in Table 1.

With the particular choice of axes, the octupole spherical harmonic $RY_{4,-4}$ splits the vertical and transverse frequencies and satisfies all the symmetry requirements. Th hexapole spherical harmonic RY_{31} add the axial bound, and satisfies all the symmetry requirements as well. Hence, these three spherical harmonic functions, $RY_{2,-2}, RY_{4,-4}, RY_{31}$, are chosen to expand the trapping potential. With three free parameters, a_2, a_4 and a_3, the potential can be spanned by the above three harmonic functions. Since there are only three measurables, resonant frequencies in all three directions, those parameters a_2, a_4 and a_3 can be solved numerically. Hence, it is argued that using only three spherical harmonic functions should suffice to describe this system.

3.3.4 Potential, Field, Energy, and Small-Oscillation Frequencies

The region of interest is the free space between the pole pieces, near the center of the trap. There is no current source, $\vec{J} = 0$, so Maxwell's equations reduce to Laplace's equation for the magnetic scalar potential Sec. 5.9B[85]:

$$\nabla^2 \Phi_M = 0. \tag{3.11}$$

The general solution to the Laplace equation can be expanded by spherical harmonics, Eq. (3.62) [85],

$$\Phi_M(r, \theta, \phi) = \sum_{l=0}^{\infty} \sum_{m=-l}^{l} \left[A_{lm} r^l + B_{lm} r^{-(l+1)} \right]. \tag{3.12}$$

In the near-field approximation, where the region of interest is around $r = 0$ and all the source distribution is "outside," $B_{lm} = 0$ for all l, m. Hence, together with the symmetry argument in Sec. 3.3.3, the magnetic potential in this trapping system is

$$\begin{aligned} \Phi_M(x, y, z) = &\left(\frac{a_2 y_0}{2}\right) \left(\frac{1}{y_0}\right)^2 r^2 R Y_{2,-2}(x, y, z) \\ &+ \left(\frac{a_4 y_0}{4}\right) \left(\frac{1}{y_0}\right)^4 r^4 R Y_{4,-4}(x, y, z) \\ &+ \left(\frac{a_3 y_0}{3}\right) \left(\frac{1}{y_0}\right)^3 r^3 R Y_{3,1}(x, y, z), \end{aligned} \tag{3.13}$$

and all other terms are ignored. Here, a_2, a_4 and a_3 are the parameters to be solved using the observed frequencies. y_0 is a length scale, chosen to be the tightest spacing among the trap dimensions, which is the vertical size. The seemingly complicated arrangement of the factors in front of the terms will become clear when the magnetic fields are derived.

The magnetic field $\vec{B}$ ("magnetic induction" in [85]) is the gradient of $\Phi_M(x, y, z)$:

$$\vec{B}(x, y, z) = -\nabla \Phi_M(x, y, z), \tag{3.14}$$

in units of Tesla (T). With the definition of the potential in Eq. (3.13), the individual terms of the magnetic field now scale as

$$\vec{B}(x, y, z) \sim \left(\frac{a_2 y_0}{2}\right) \left(\frac{1}{y_0}\right)^2 r + \left(\frac{a_4 y_0}{4}\right) \left(\frac{1}{y_0}\right)^4 r^3 + \left(\frac{a_3 y_0}{3}\right) \left(\frac{1}{y_0}\right)^3 r^2 \tag{3.15}$$

since r itself is of the same order as y_0. Hence, it can be seen now that this convention for the parameters balance the scales, so the parameters can be of the same order of magnitude. Furthermore, the magnetic field strength at $r \sim y_0$ is ~ 1 T, the surface field strength of the magnets specified. It is still to be reminded that the second and third terms of the potential and field are small perturbation to the leading quadrupole term, though the free parameters a_2, a_4 and a_3 are adjusted to be the same order, and are all in units of T.

The Hamiltonian of a diamond particle of mass m in this magnetic trap consists of three terms,

$$H = K + U_g + U_B. \tag{3.16}$$

The kinetic energy and gravitational potential energy are simply

$$K = \frac{1}{2}m\left(\dot{x}^2 + \dot{y}^2 + \dot{z}^2\right), \text{and} \tag{3.17}$$

$$U_g = mgy, \tag{3.18}$$

respectively.

The magnetic potential energy is [39] (see derivation in Appendix B)

$$U_B = -\frac{\chi\left(B(x,y,z)\right)^2 V}{2\mu_0}. \tag{3.19}$$

Near the equilibrium positions, (x_{eq}, y_{eq}, z_{eq}), the motion of the trapped particle can be approximated by harmonic oscillation with frequencies ω_x, ω_y, and ω_z. The following then explains how the equilibrium positions are calculated and the relationships between the Hamiltonian and the oscillation frequencies.

Employing the symmetry argument again, it is clear that in the x- and z- direction, there should not be any mechanism to favor any other points than the origin. Hence, $x_{eq} = z_{eq} = 0$. For the y direction, since gravity is involved, y_{eq} is expected to be slightly negative, towards the earth. The exact position can be solved from the equation

$$F_y(y) = -\frac{d}{dy}U(x_{eq} = 0, y, z_{eq} = 0) = 0, \tag{3.20}$$

where $U(x,y,z) = U_g(x,y,z) + U_B(x,y,z)$.

The small-oscillation frequencies are calculated from Hamilton's equations, Eq. (32.30) [86],

$$\ddot{x} = -\frac{\partial H}{\partial x} \approx -\omega_x^2 x \tag{3.21}$$

$$\ddot{y} = -\frac{\partial H}{\partial y} \approx -\omega_y^2 y \tag{3.22}$$

$$\ddot{z} = -\frac{\partial H}{\partial z} \approx -\omega_z^2 z, \tag{3.23}$$

meaning the coefficients in the linear terms of the derivatives are the frequencies squared. Here $H = U(x, y, z)$. See Sec. 3.3.5.1 for the full expression of $\omega_{x,y,z}$.

3.3.5 Full Expressions and Beyond Linear Terms

The full expression for the total potential energy per unit mass is

$$\begin{aligned}
\mathcal{U} = U/m = &+gy - \frac{15a_2^2\chi}{32\pi\mu_0\rho y_0^2}\left(x^2+y^2\right) + \frac{\sqrt{\frac{35}{2}}a_2a_3\chi}{4\pi\mu_0\rho y_0^3}\left(\frac{5}{4}x^2y + \frac{1}{4}y^3 - yz^2\right) \\
&- \frac{15\sqrt{21}a_2a_4\chi}{64\pi\mu_0\rho y_0^4}\left(x^4 - y^4\right) \\
&+ \frac{7a_3^2\chi}{\pi\mu_0\rho y_0^4}\left(-\frac{3}{64}x^4 - \frac{5}{96}x^2y^2 - \frac{5}{24}x^2z^2 - \frac{1}{192}y^4 + \frac{1}{24}y^2z^2 - \frac{1}{12}z^4\right) \\
&+ \frac{7\sqrt{\frac{15}{2}}a_3a_4\chi}{16\pi\mu_0\rho y_0^5}\left(\frac{11}{4}x^4y - \frac{3}{2}x^2y^3 - 3x^2yz^2 - \frac{1}{4}y^5 + y^3z^2\right) \\
&- \frac{315a_4^2\chi}{512\pi\mu_0\rho y_0^6}\left(x^6 + 3x^4y^2 + 3x^2y^4 + y^6\right).
\end{aligned} \tag{3.24}$$

Eq. (3.24) contains the magnetic energy from the three multipole expansion terms and gravitational potential energy.

3.3.5.1 Linear Force Terms

With the kinetic energy per unit mass

$$\mathcal{T} = T/m = \frac{1}{2}\left(\dot{x}^2 + \dot{y}^2 + \dot{z}^2\right), \tag{3.25}$$

the Lagrangian per unit mass is

$$\mathcal{L} = \mathcal{T} - \mathcal{U}. \tag{3.26}$$

The Lagrange's equation of motion is

$$\frac{\partial \mathcal{L}}{\partial \zeta} = \frac{d}{dt}\left(\frac{\partial \mathcal{L}}{\partial \dot{\zeta}}\right), \tag{3.27}$$

where ζ stands for x, y and z. $\dfrac{d}{dt}\left(\dfrac{\partial \mathcal{L}}{\partial \dot{\zeta}}\right)$ in this system is simply $\ddot{\zeta}$. On the other hand, the $\dfrac{\partial \mathcal{L}}{\partial \zeta}$ is very complicated. Linear algebraic techniques to analyze the normal modes of motion can be used for only linear terms in $\dfrac{\partial \mathcal{L}}{\partial \zeta}$. The eigenvectors represent the normal axes of motion. Generally, this can be a linear combination of the orthogonal axes x, y, and z.

A further assumption to be made is that the Lagrangian shall be analyzed around the equilibrium point. As seen in Sec. 3.3, the equilibrium coordinates are $x_{\text{eq}} = z_{\text{eq}} = 0$, by symmetry; $y_{\text{eq}} < 0$, due to gravity. Therefore, the coordinates are replaced by the equilibrium plus a small displacement and then expanded: $x \to \Delta x$, $z \to \Delta z$, and $y \to y_{\text{eq}} + \Delta y$. Taking the first partial derivative with respect to ζ, expanding around ζ_{eq}, and keeping only the linear terms, Lagrangian's equations are

$$\ddot{x} = \frac{\chi}{8\pi\mu_0\rho y_0^2}\left(\frac{15a_2^2}{2} - \frac{\sqrt{\frac{35}{2}}a_2a_3}{y_0}y_{\text{eq}} + \frac{35a_3^2}{6y_0^2}y_{\text{eq}}^2 + \frac{21\sqrt{\frac{15}{2}}a_3a_4}{2y_0^3}y_{\text{eq}}^3 + \frac{945a_4^2}{32y_0^4}y_{\text{eq}}^4\right)\Delta x \tag{3.28}$$

$$\begin{aligned}\ddot{y} = h_{y0} + \frac{\chi}{8\pi\mu_0\rho y_0^2}\Bigg(&\frac{15a_2^2}{2} - \frac{3\sqrt{\frac{35}{2}}a_2a_3}{y_0}y_{\text{eq}} + \frac{7a_3^2}{2y_0^2}y_{\text{eq}}^2 \\ &- \frac{45\sqrt{21}a_2a_4}{2y_0^2}y_{\text{eq}}^2 + \frac{35\sqrt{\frac{15}{2}}a_3a_4}{2y_0^3}y_{\text{eq}}^3 + \frac{4725a_4^2}{32y_0^4}y_{\text{eq}}^4\Bigg)\Delta y\end{aligned} \tag{3.29}$$

$$\ddot{z} = \frac{a_3\chi}{2\pi\mu_0\rho y_0^3}\left(\sqrt{\frac{35}{2}}a_2y_{\text{eq}} - \frac{7a_3}{6y_0}y_{\text{eq}}^2 - \frac{7\sqrt{\frac{15}{2}}a_4}{4\rho y_0^3}y_{\text{eq}}^3\right)\Delta z$$

where the constant term h_{y0} is

$$h_{y0} = -g + \frac{15a_2^2\chi}{16\pi\mu_0\rho y_0^2}y_{\text{eq}} - \frac{3\sqrt{\frac{35}{2}}a_2a_3\chi}{16\pi\mu_0\rho y_0^3}y_{\text{eq}}^2 - \frac{15\sqrt{21}a_2a_4\chi}{16\pi\mu_0\rho y_0^4}y_{\text{eq}}^3 \tag{3.30}$$
$$+ \frac{7a_3^2\chi}{48\pi\mu_0\rho y_0^4}y_{\text{eq}}^3 + \frac{35\sqrt{\frac{15}{2}}a_3a_4\chi}{64\pi\mu_0\rho y_0^5}y_{\text{eq}}^4 + \frac{945a_4^2\chi}{256\pi\mu_0\rho y_0^6}y_{\text{eq}}^5 \approx 0$$

near the equilibrium.

Equation (3.28) to (3.30) thus give the analytical first-order approximation for the oscillation frequencies $\omega_{x,y,z}$ in Sec. 3.3. Hence, the basic characteristics can be seen for all three degrees of freedom. First, zeroth order terms are approximately zero, giving only restoring forces. Second, all degrees of freedom are decoupled to the first order, i.e., x, y and z are still good choices to describe the motion.

3.3.5.2 Non-Linear Force Terms and Its Impact Beyond Harmonic Oscillation

Now consider the higher order terms, which include all terms with $\Delta\zeta_1\Delta\zeta_2$. Lagrangian's equations of

motion are

$$\ddot{x} = (\text{linear terms}) \tag{3.31}$$
$$+ \frac{\chi}{8\pi\mu_0\rho y_0^3}\left(-5\sqrt{\frac{35}{2}}a_2a_3 + \frac{35a_3^2}{3y_0}y_{\text{eq}} + \frac{63\sqrt{\frac{15}{2}}a_3a_4}{2y_0^2}y_{\text{eq}}^2 + \frac{945a_4^2}{8y_0^3}y_{\text{eq}}^3\right)\Delta y\Delta x$$

$$\ddot{y} = (\text{linear terms}) \tag{3.32}$$
$$+ \frac{\chi}{16\pi\mu_0\rho y_0^3}\left(-5\sqrt{\frac{35}{2}}a_2a_3 + \frac{35a_3^2}{3y_0}y_{\text{eq}} + \frac{63\sqrt{\frac{15}{2}}a_3a_4}{2y_0^2}y_{\text{eq}}^2 + \frac{945a_4^2\chi}{8y_0^3}y_{\text{eq}}^3\right)\Delta x^2$$
$$+ \frac{a_3\chi}{4\pi\mu_0\rho y_0^3}\left(\sqrt{\frac{35}{2}}a_2 - \frac{7a_3}{3y_0}y_{\text{eq}} - \frac{21\sqrt{\frac{15}{2}}a_4}{4y_0^2}y_{\text{eq}}^2\right)\Delta z^2$$
$$+ \frac{\chi}{16\pi\mu_0\rho y_0^3}\left(-3\sqrt{\frac{35}{2}}a_2a_3 + \frac{7a_3^2}{y_0}y_{\text{eq}} - \frac{45\sqrt{21}a_2a_4}{y_0}y_{\text{eq}}\right.$$
$$\left. + \frac{105\sqrt{\frac{15}{2}}a_3a_4}{2y_0^2}y_{\text{eq}}^2 + \frac{4725a_4^2}{8y_0^3}y_{\text{eq}}^3\right)\Delta y^2$$

$$\ddot{z} = (\text{linear terms}) + \frac{\sqrt{a_3\chi}}{2\pi\mu_0\rho y_0^3}\left(\sqrt{\frac{35}{2}}a_2 - \frac{7a_3^2}{3y_0}y_{\text{eq}} - \frac{21\sqrt{\frac{15}{2}}a_3}{4y_0^2}y_{\text{eq}}^2\right)\Delta y\Delta z \tag{3.33}$$

From the above expressions it is clear that to second order, the motion in x and z are both coupled to y, which is expected since gravity shifts the y equilibrium point. On the other hand, the motion in y is mixed with x and z in quadratic forms. All parameters a_2, a_3, and a_4 come in in all directions.

3.3.6 Numerical Results

To solve for the numerical values of the parameters and the vertical equilibrium point, a few constants are specified. Diamond has a magnetic susceptibility of $\chi = -2.2 \times 10^{-5}$ (SI units), and mass density of 3500 kg/m^3. Typical values of the observed oscillation frequencies are $\omega_{x,exp} \approx 2\pi \times 100$, $\omega_{y,exp} \approx 2\pi \times 150$, $\omega_{z,exp} \approx 2\pi \times 10$ Hz. The trap dimensions are ∼250 μm in the x direction, ∼150 μm in the y direction, and ∼250 μm in the z direction. Therefore, $y_0 =$ 75 μm.

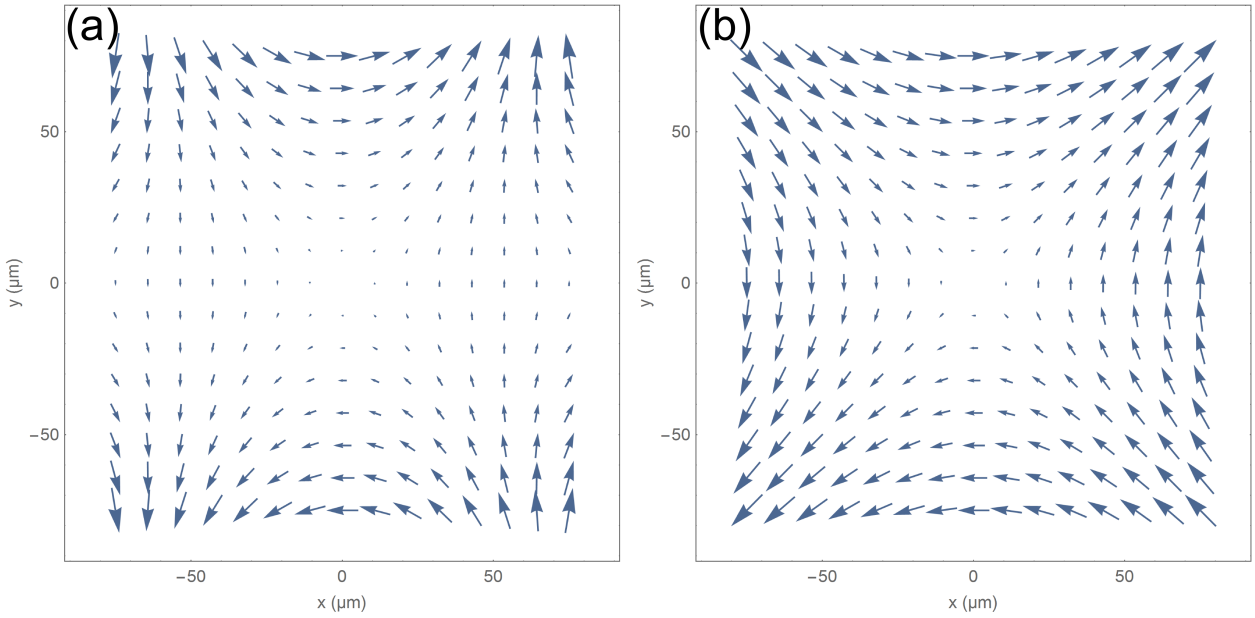

Figure 7: Vector plots of the magnetic fields in the $x-y$ plane. Parameters used are (a) $a_2 = -1.2$ T and $a_4 = 0.72$ T and (b) $a_2 = -1.2$ T and $a_4 = 0$. a_3 is arbitrary.

The effect of the octopole can be seen explicitly in Fig. 7, where in (a) the field strength from top to bottom is weakened and across the top or bottom pieces are strengthened. As a reference, Fig. 7(b) shows a perfect quadrupole field distribution, where the fields going side to side and top to bottom are equal in strength.

With the parameters same for generating Fig. 7(a), the equilibrium point in the vertical direction is numerically solved to be $y_{eq} \approx 17.9$ μm, roughly one-quarter way towards the vertical trap boundary in one direction. Because of gravity, the equilibrium point for the particle has a finite magnetic field strength, ~ 0.17 T. Compared with the zero-field splitting of the NV, ~ 0.1 T, the field offset can interfere with the splitting field. Equating the expressions containing $a_{2,4,3}$ for the frequencies in Eq. (3.21) with the observed ones, the parameters are numerically solved: $a_2 \approx -1.21$ T, $a_4 \approx 0.72$ T, $a_3 \approx 0.018$ T.

The octopole also manifests itself in the oval shape of field in Fig. 8(b), as opposed to a perfect circle.

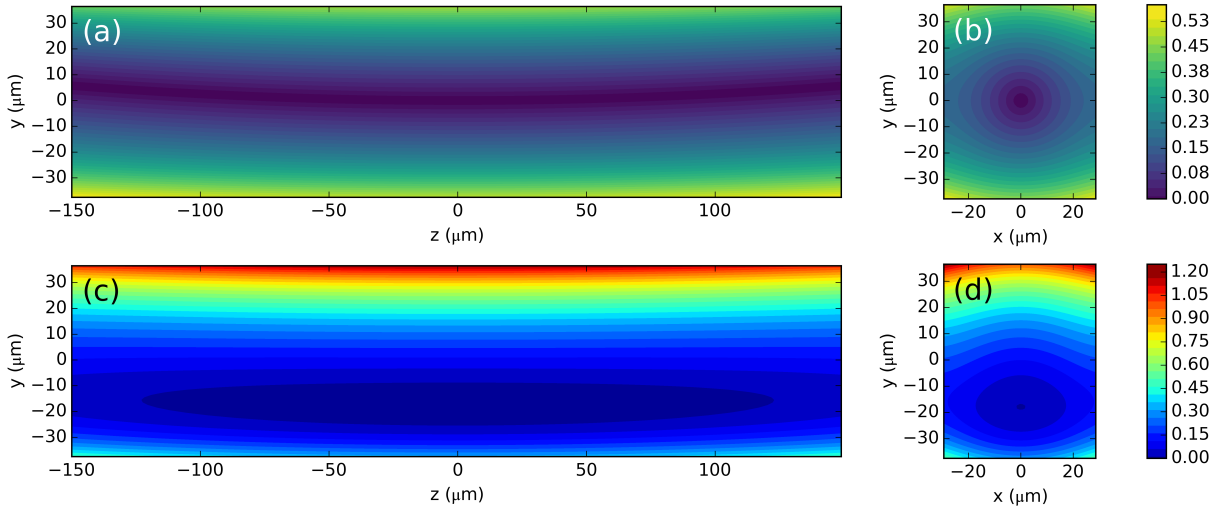

Figure 8: Plots of magnetic fields and energy per mass near the trap region, with parameters $a_2 \approx -1.3, a_4 \approx 0.72, a_3 \approx 0.018$, in units of T. (a) and (b) are the magnetic field profiles in the $y-z$ and $y-x$ planes, respectively. (c) and (d) are the total energy (including gravity) per mass in the $y-z$ and $y-x$ planes, respectively. Shifting due to gravity is clear.

3.3.7 Comparison with ANSYS Results

Parameters $a_{2,3,4}$ can always be solved with any three chosen spherical harmonics. Therefore, though the fields and energy plots in Fig. 8 look similar to a quadrupole magnetic field plus gravity, it is reasonable to ask whether this expansion reflects the behavior of the actual trap geometry.

A commercial finite-element analysis software ANSYS [87] was used to check the field and energy distributions. See Fig. 9 for typical calculation results of the magnetic fields and energies after taking into account gravity. It can be seen in Fig. 9(b) a long, closed volume (in light blue) near the trap center.

With ANSYS, such qualitative features are about as much as one can get for a trapping system in this dissertation work, for several practical reasons. First, the results depend on the material parameters settings. The material Hiperco 50A (Sec. 3.4) is not in ANSYS' database, causing less accuracy in the calculation. Second, even though the calculation volume is reduced to one quarter of the whole system, the calculation is still time-consuming and can crash the computer. Third, as is manifested in Fig. 10, possibly due to the rounding error in the position meshing process of the finite-element calculation, the numerical values are very noisy, as opposed to a smooth curve. Lastly, this kind of "brute force" calculation presents the trapping strength of a particular geometry and set of parameters, but can not provide a direction to improve. Trial-and-error with different parameters each time was the best option.

Nevertheless, after the multipole expansion technique was established, the ANSYS results can then be used as a realistic map to compare against. This can provide insight near the center region of the trap, where the behaviors of the expansion and the finite-element calculation agree with each other.

Figure 10(a)-(j) compare all the magnetic field profiles along all the axes (through zero) between the two approaches.

Except for Fig. 10(a) in which the ANSYS result is too noisy, all of the plots that the fields are non-zero, Fig. 10(b), (d), and (h), agree with each other near the geometrical center. Since this distance encloses the actual trapping center, $y_{eq} \approx 17.9$ μm, the multipole expansion is valid and satisfactory, without a lot of computational resources.

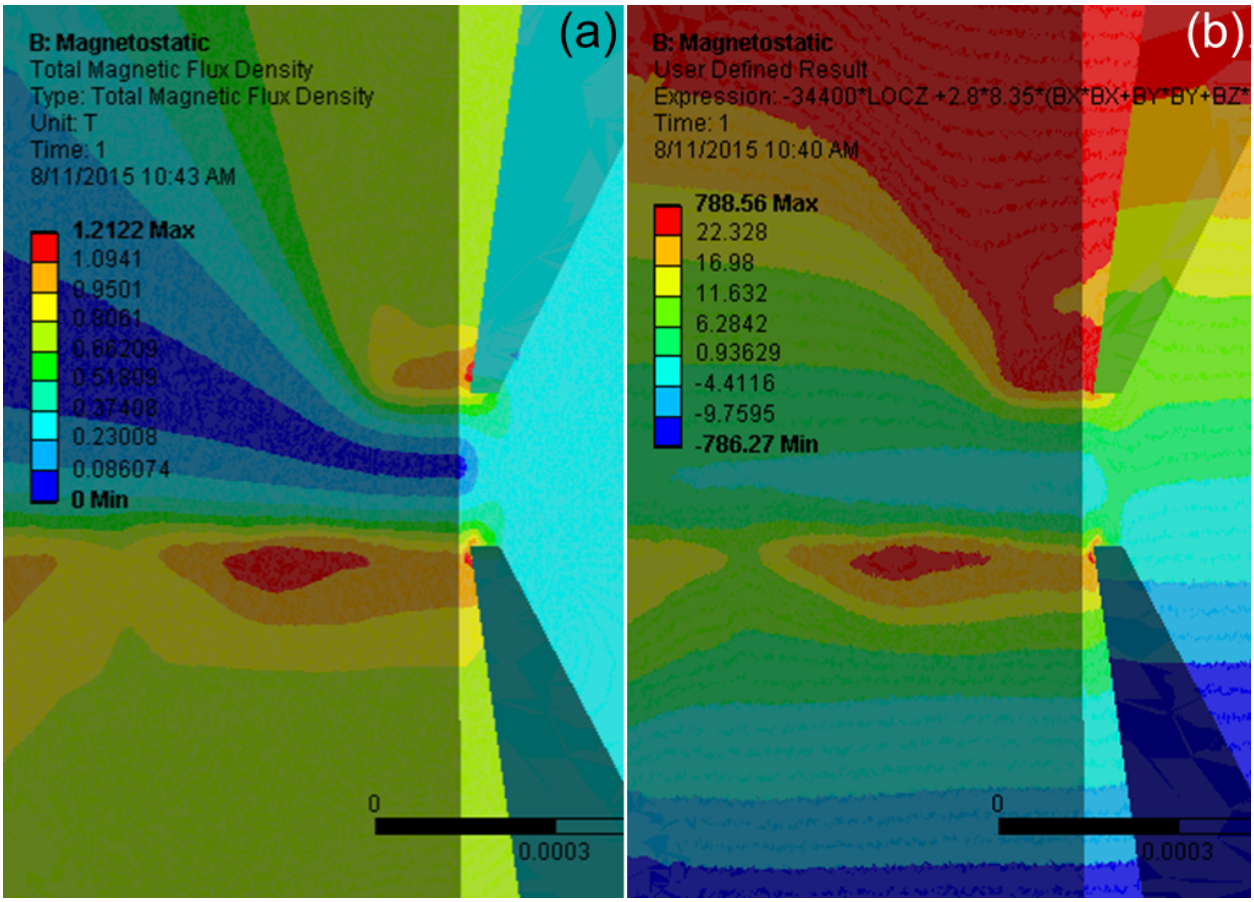

Figure 9: (a) ANSYS-calculated magnetic field, $|B|$, exposing two cross-sections, $y-z$ and $x-y$. (b) Energy-per-unit-mass plot, $\frac{U}{m} \sim gy - \frac{\chi B^2}{2\rho\mu_0}$.

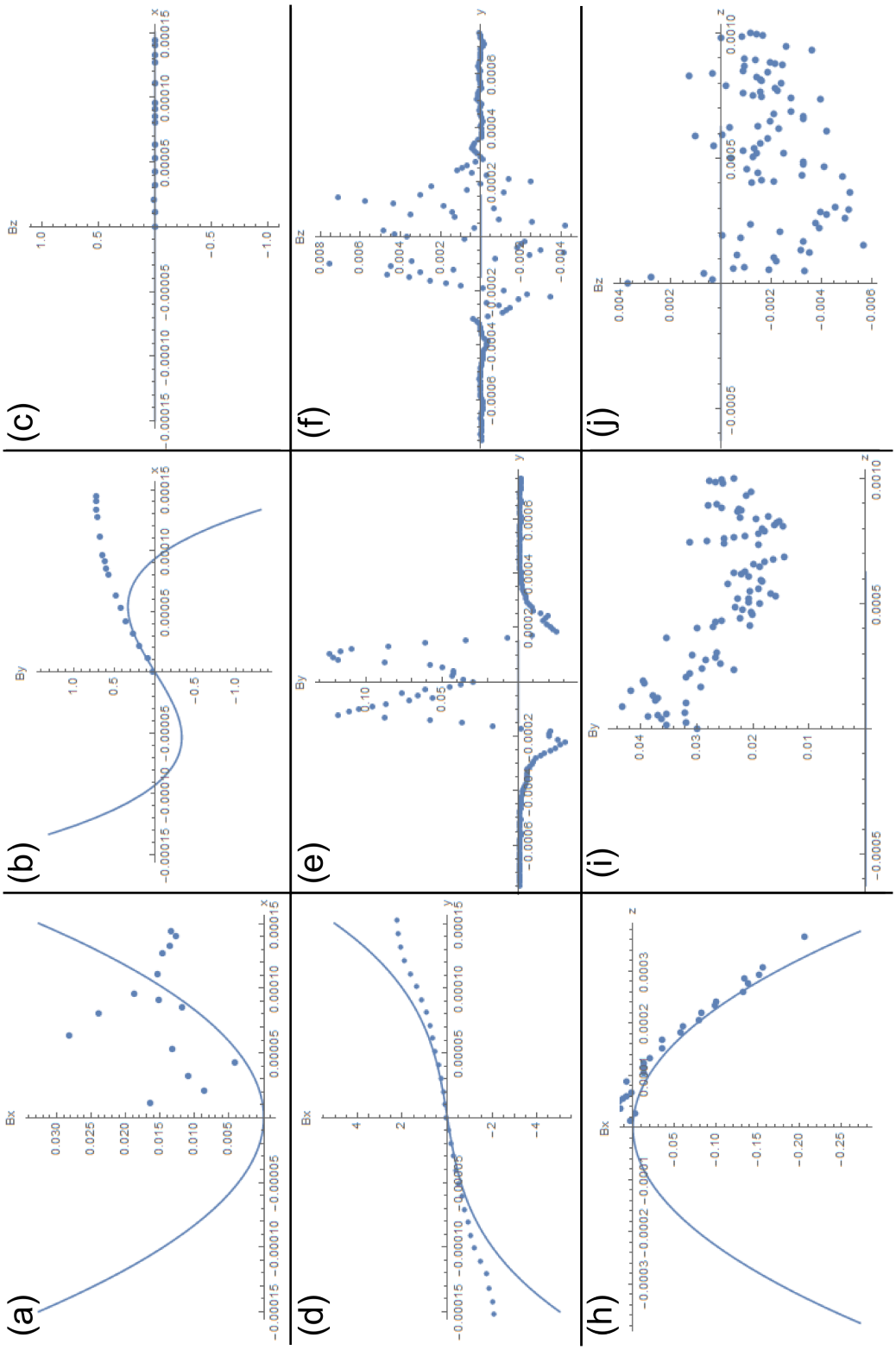

Figure 10: (a) B_x, x component of the trapping magnetic field in Tesla (T), along the x direction, in meter. The dots are ANSYS calculation data points, and the curve is from multipole expansion. (b) - (j) Other components along other directions.

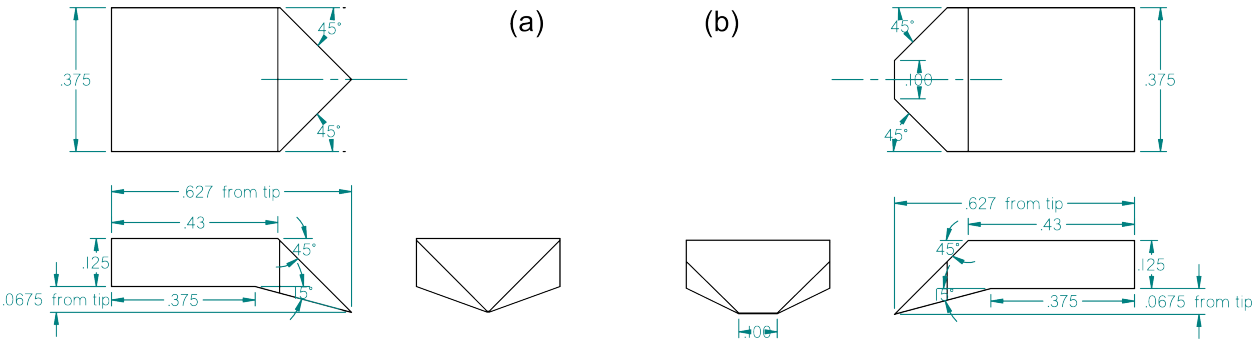

Figure 11: Mechanical design of the pole pieces. (a) Top piece. The target length of tip is 250 μm. (b) Bottom piece. Dimensions are in units of inches.

3.4 TRAP SETUP

3.4.1 Pole Piece Machining

The pole pieces are machined out of the material Hiperco 50A (Ed Fagan Inc.), an iron-cobalt alloy that has the highest magnetic saturation of 2.4 T [88]. Ductile iron (65-45-12 alloy) and magnetic stainless steel (430FR, M. Vincent & Associates) have also been tested. The advantage of hiperco 50A and the stainless steel over the ductile iron is that they are corrosion resistant to moisture.

The initial machining of the pole pieces is done by the Dietrich School of Arts and Sciences machinists, where the pole tips are left with sharp finishes. See Fig. 11 for the mechanical design of the pole pieces.

Afterwards, the tips are lapped against a fine emery cloth to attain the desired flat surfaces in design. Figure 12, showing the flat tip parts, compares the finishes from emery cloth lapping and traditional machining (milling, etc.) Lapping indeed makes the edges more uniform and avoids large chipping of the material. Appendix C contains the full step-by-step procedure of the pole pieces lapping and relevant design files.

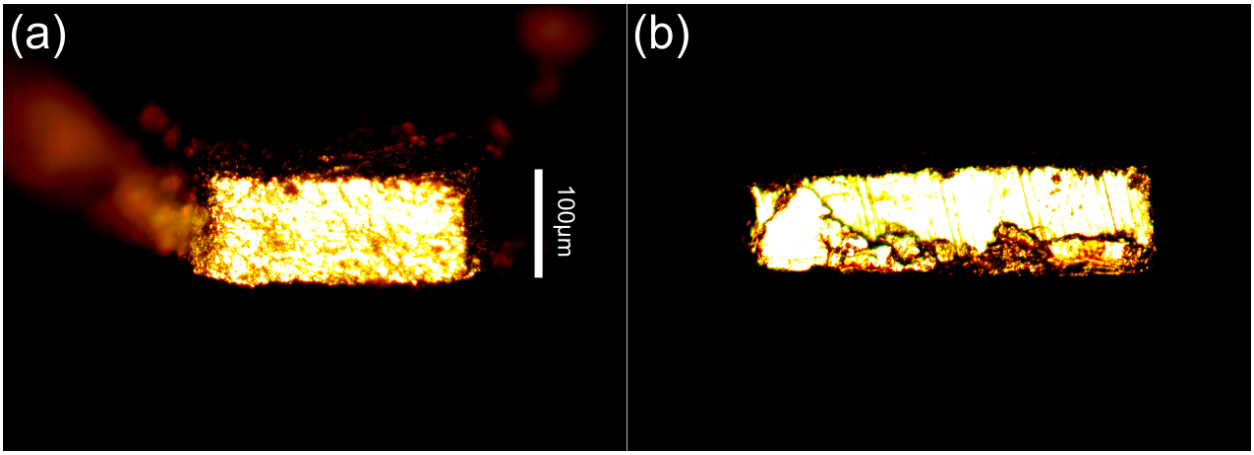

Figure 12: (a) Flat tip surface that is lapped after initial machining. (b) Finish with a milling machining.

3.4.2 Trap Assembly

Two lapped identical top and bottom pieces and a SmCo magnet of dimensions $\frac{3}{8}" \times \frac{3}{8}" \times \frac{1}{8}"$ are stacked together with proper stainless steel shims of 75 to 175 μm thick in between to maintain the desired spacing. Pieces of polyimide (kapton) films are added as needed for electric insulation. See Fig. 13(a) for the pole piece assembly diagram. Since the bare drive wire touches the bottom pieces, in order not to provide a leak path for the drive current, the bottom pole pieces are insulated from each other and the plate by kapton films. On the other hand, a uniform potential is desired at the top pole pieces at this stage, so no insulating films are needed.

3.4.3 Mounting

Both stacks of pole pieces are clamped down to an aluminum plate (Fig. 14(a)). The gap between the top and bottom pieces are then fine adjusted. Figures 13(b) and (c) show how the gap size affects the available NA of light collection. The nominal gap, at which the now-imaginary pole tips just touch, gives an NA of ≈ 0.7 from the geometry of the pieces. While the available NA is larger than what the objective demands (0.55), the two stacks can be brought closer to have a gap of $0.053"$, if a stronger trap is desired (Fig. 13(c)). See Fig. 14(d) (viewing from transverse

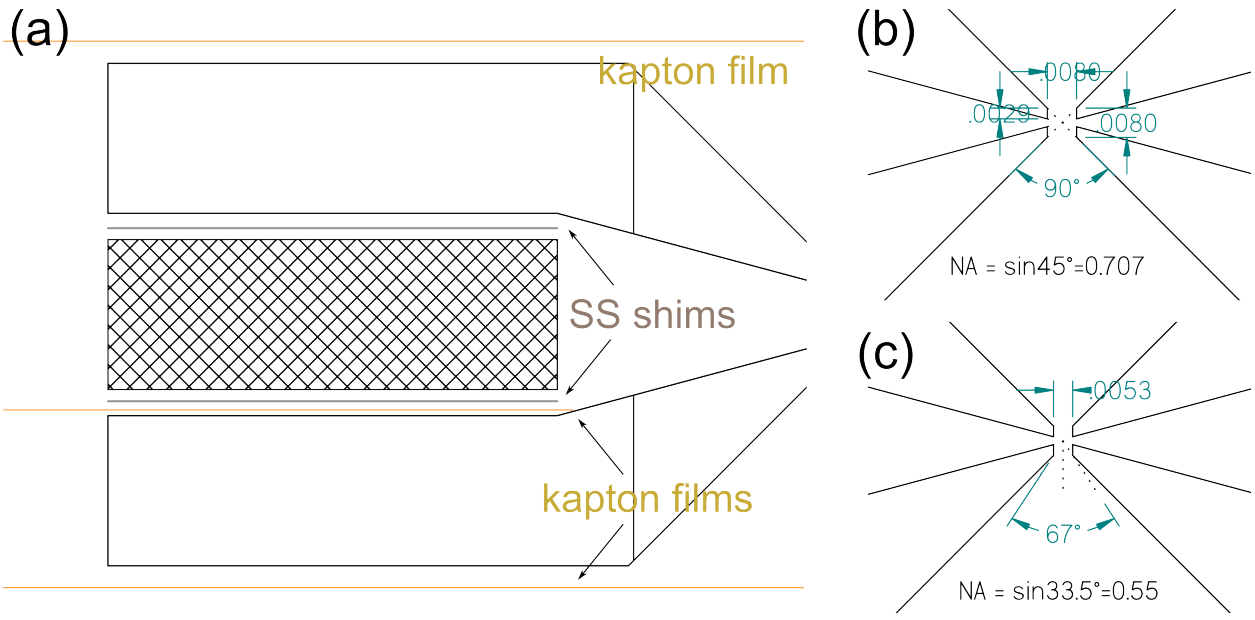

Figure 13: Assembly detail of the pole pieces stack. (a) Typical insulation sheets and spacing shims arrangement. (b) $0.7\ NA$ option of gap spacing. (c) $0.55\ NA$ option of gap spacing. Dimensions are in units of inch.

direction) and (e) (from axial) for the microscope photographs of the assembled trap aiming for the 0.55 NA option. The dissertation work uses this NA option throughout.

Upon finalizing the position of the trap itself, peripheral devices such as the drive wire, biasing wire, field emission point, and thermal couple are mounted on the aluminum plate as needed. See Fig. 14(a) for the additional devices to be mounted. Though it might not be ultra-high vacuum compatible, the drive wire (30 μm diameter gold-plated tungsten, Luma Metal) is strapped across the bottom pieces very close to the trapping volume and is held down to the flat part of the pieces by kapton tape. The plate with the fully assembled trap and peripherals are then mounted on the moving stage in the chamber, with the heater film sandwiched in between. The electrical connections from the assembly plate to chamber feedthroughs are subsequently made.

3.5 LOADING PARTICLES INTO TRAP

Loading micron/submicron-sized particles into an optical or here a magnetic trap is actually not trivial, dominantly due to the fact that the Van der Waals force is no longer small and negligible as the overall particle volume decreases to this scale. This section therefore describe the loading method employed in this dissertation work in detail.

3.5.1 Overcoming the Sticky Van der Waals Force – Ultrosonic Vibration

The diamond nanocrystals primarily used in this dissertation work are ND-1600NV-140nm from Adámas Nanotechnologies in isopropanol (Fig. 25(a)), with a size distribution centered around 140 nm. For micron or submicron particles, the "pull-off" force required to separate them from other surfaces is usually much greater than the gravitational force on them [89, 90, 91]. Therefore, these particles would not be "shaken off" by gravitational or hand acceleration. But a fast oscillating actuator at an ultrasonic frequency such as a horn with a piezoelectric element would provide enough force to overcome the Van der Waals force.

3.5.1.1 Titanium Horn Atomizer To be able to reach inside the chamber, a compact loading tool is required. Also, most commercially available nebulizers operate at a frequency in

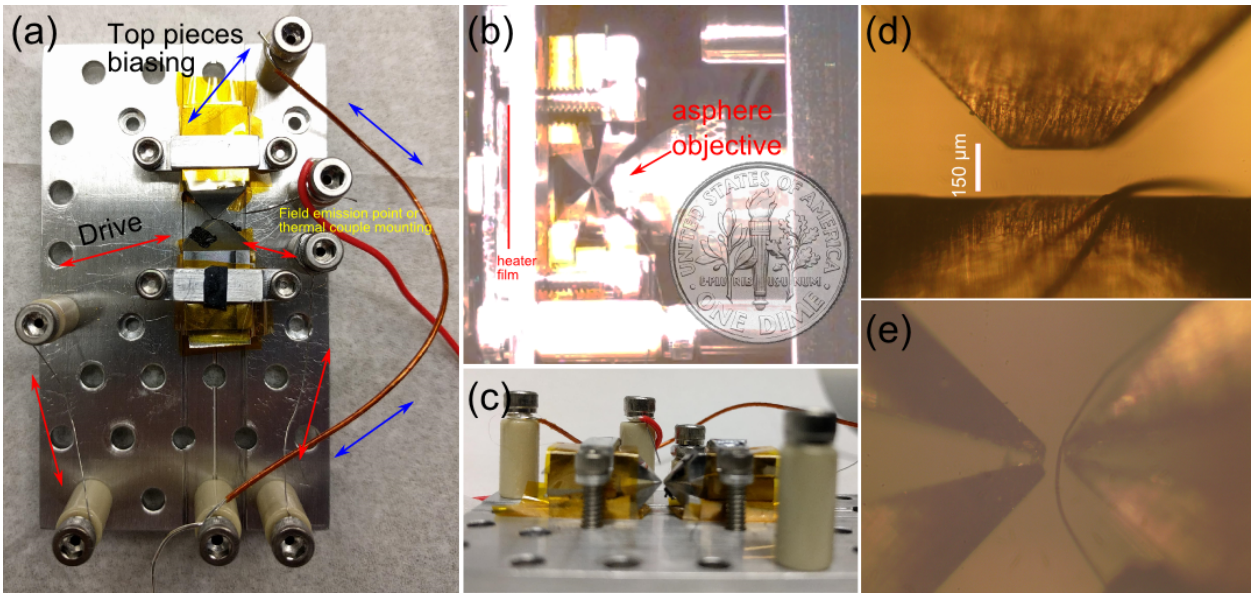

Figure 14: Photographs of the assembled trap. (a) The trap and peripherals on the mounting plate, top view. (b) Side view of the trap and mounted objective in the chamber. (c) Side view of the trap and peripherals on the mounting plate. (d) Microscope photograph of the trapping region, from transverse direction and (e) from axial direction.

Surface potential (V)	Positive	Negative	Neutral or too massive
floating	6 (27%)	14 (64%)	2 (9%)
0, grounded	14 (70%)	5 (25%)	1 (5%)
+25	20 (95%)	0	1 (5%)

Table 2: Charge polarity of the loaded droplet with various loading horn surface potential.

the order of ∼MHz, generating smaller droplets (∼ µm) than desired (10 - 20 µm). Therefore, a titanium horn is designed and used in this work, as shown in Fig. 41, to sweep a frequency range of 100 - 150 kHz. It is similar to a previously published one [92]. A driving circuit that is similar to another previous work [89] was built. See Appendix E.1 for details. The compactness of the design makes it easy to handle inside the experiment chamber and is ready to launch liquid or dry powder typically ∼ 100 nL to 100 fL (∼10 to 20 µm in diameter).

3.5.2 Horn Surface Potential and Charge Polarity of the Loaded Droplets

A strong correlation has been found between the surface potential of the horn while loading and the charge polarity of the loaded droplets in the trap. As shown in Fig. 41(c), the surface potential is defined by attaching a wire from the horn body (typically clamped by a screw) to a voltage power supply (< 30 V, in series with a large resistor, say 1 MΩ, for safety) or simply a ground point. Note that this surface potential is independent of the piezo driving potential, as there are insulating kepton films sandwiching the piezo, to avoid shorting the piezo voltage difference through the metal horn body. The charge polarity can be checked by applying a positive bias voltage on the top pole pieces (Fig. 14), posi (nega)-tively charged droplets would move down (up)-wards.

Table 2 summarizes droplet polarities with various horn surface potentials. Some droplets will have smaller charge-to-mass ratios, and hence the movement is too small to determine the polarity. First, it is surprising that 25 volts of biasing is enough to almost exclusively define the droplet charge state. Secondly, it is indeed sensitive to the horn potential, as increasing the

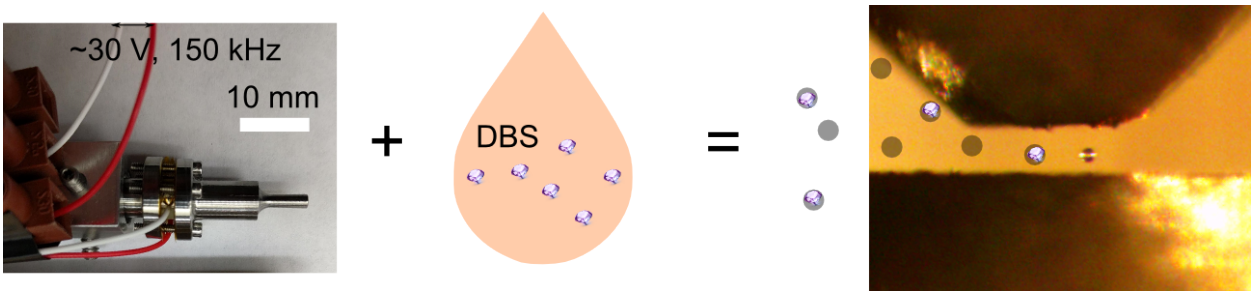

Figure 15: An idea sketch of the sacrificial liquid loading strategy. A drop of slurry of nanodiamond in DBS is placed at the tip of the ultrasonic horn near the trap. The vibration of the horn then atomize the slurry into droplets of 10 to 20 μm. Finally some droplets drift into the trap center.

potential from 0 to +25 volts raised the probability of positive loading from 70 to 95 percent. Thirdly, droplets from an ill-defined potential (floating) surface favor negative charge state.

3.5.3 Transitioning from Air to High Vacuum – Sacrificial Liquid

Though capable of launching and loading the diamond clusters dry, the experiment actually starts with atomizing liquid droplets with diamond nanocrystals mixed in. The reasons are as follows. The desired state is a small and dry cluster or single diamond nanocrystal trapped in high vacuum. Loading the small cluster in air has several mechanisms to knock it out of the trap, including air flow during rough pumping, thermal energy fluctuation, and excitation by the ramp-up of turbomolecular pump. Therefore, it is desirable to start with a larger mass which "slowly" reduces. "Slowly" means comparable or longer than the time for sealing the chamber after loading, and pumping to high vacuum, which amounts to ~ 15 mins. A natural and obvious implementation would be a slowly evaporating sacrificial liquid. A second advantage of loading diamond-containing liquid first is that the trapped particle size can be controlled simply by tuning the concentration of the diamond in the sacrificial liquid. The idea of this approach is illustrated in Fig. 15.

Since the final pressure is high to ultra-high vacuum, the sacrificial liquid must have a very low vapor pressure. Silicone oils have been attempted, but due to their mixture nature, part of the

Liquid name	Vapor pressure (Torr)	Viscosity
Triethylene glycol	1.32×10^{-3} at $25°$C [94]	47.8 cP at $20°$C [95]
Glycerol (glycerin)	1.68×10^{-4} at $25°$C [94]	954 cP at $25°$C [96]
Tetraethylene glycol	4.65×10^{-5} at $26°$C [97]	61.9 cP at $20°$C [98]
Dibutyl sebacate	4.69×10^{-6} at $25°$C [94]	

Table 3: The loading liquids around room temperature, the vapor pressures and viscosity.

loaded liquid had very low vapor pressure and did not pump away. Table 3 lists the other liquids that have been tried in this dissertation work, and their physical properties. Dibutyl sebacate (DBS) has been used in other experiments of levitated droplets [93].

DBS seems to have the most adequate evaporation time scale and the least electric charging problems. Therefore, DBS is mostly used in this work. The DBS is diluted by a factor of 10 with high purity isopropanol (Fisher A464SK) if the original diamond slurry is in isopropanol, and ethanol if the original is in water or ethanol (200 Proof.) Higher atomizer voltages would be required for loading liquids with higher viscosity (Table 3.) The original diamond slurry, Adámas ND-1600NV-140nm, about one tenth the DBS volume, is then mixed in. In summary, a typical solution can be prepared by mixing 1 mL of isopropanol, 100 µL of DBS, and 10 µL of original diamond slurry. This diamond concentration almost always generates a dried cluster after vacuum of a few microns, indicating thousands of nanodiamond in the trap. So, if few or single diamond crystal trapping is desired, the concentration needs to be cut down.

3.5.4 Purifying Droplet – Vacuum Distillation of DBS

It has been observed that even a DBS droplet loaded from the original bottle without mixing in diamond would not be completely pumped away. This indicates that impurities, especially the low vapor pressure part, is significant enough to impact the final size. The impurity is not surprising since the DBS solution (84840, Sigma-Aldrich) is only specified to be 97% or more pure. A loaded droplet is required to dry from typically 10 µm to 1 µm, an evaporation of

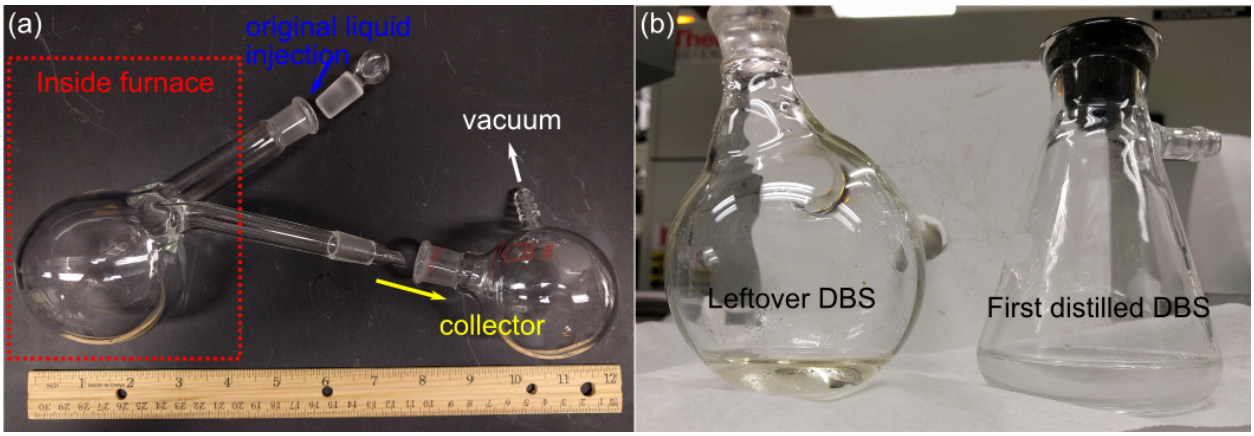

Figure 16: Glasswares for distilling DBS.

99.9% of material. Therefore, a mere 0.1% of high vapor-pressure residue out of a total of 3% is considered significant.

In terms of improving the purity of the off-the-shelf DBS, it is a perfect situation to use a distillation technique, where higher vapor pressure material is distilled to a new container, while the rest of the lower-vapor-pressure material is left behind. However, an added technical complexity is that at a partial vacuum of 3 Torr, the boiling point of DBS is around 180° C, higher than many of the modern distillation designs can handle.

To overcome this technical issue, a customized retort was designed for the purpose of distilling DBS in this work. See Fig. 16(a) for the glasswares used. The retort used in the furnace is made from Pyrex glass, for its good temperature performance. Unlike most modern setups, this retort does not have any glass joints (requiring vacuum grease) in the "hot zone," the whole container can be brought to 180° C safely without worries of vacuum grease degrading or burning.

After the first distillation, it can be seen (Fig. 16(b)) that a yellowish liquid is more concentrated in the leftover DBS, possibly indicating it is of higher vapor pressure. After distilling several times, using caution to clean the glasswares thoroughly after each distillation, it is seen that the purified DBS droplets do eventually shrink and vanish, though not as fast as the initial evaporation.

See Appendix D for the detailed setup and procedure for distillation of DBS.

3.6 POST-LOADING MANIPULATION

Post-loading manipulation includes pre-neutralization of the droplet in air, baking to accelerate drying, and precision neutralization of the dried particle.

3.6.1 Pre-Neutralizing Charge of the Trapped Droplet/Particle – Radioactive Source

In addition to the charge state control by the horn surface potential, as described in Sec. 3.5.2, a radioactive source of Americium-241 (α particle source) is brought close (a few millimeters) to the trapped particle for a few minutes. This practice was found to efficiently reduce the charge on the droplets in air, to the point that they coalesce and movement is no longer seen when biasing the top pole pieces.

The mechanism is believed to be that ionizing air can in turn generate mixes of positive ions and electrons, and then neutralize the droplet [99, 100].

3.6.2 Baking Dry

From the room-temperature vapor pressure of DBS (Table 3), $\sim 10^{-6}$ Torr, to the fact that at around 180° C, DBS can be distilled (evaporated) with $\sim 10^{-3}$ Torr of vacuum (or worse), it should be clear that the evaporation rate changes several orders of magnitude between 25 to 180° C. This implies a large dependency of the evaporation pressure, several orders of magnitude, on the temperature, over the range from 25 to 180°. Also, if there are impurities in the loading liquid with lower vapor pressure than DBS, the chance for them to be baked out in a shorter time is higher.

Therefore, a kapton film heater (Omega KHLV-101/10) is sandwiched in the back of the trap assembly plate (Fig. 14(b)). Although the trapped droplet is thermally isolated from the environment (one reason this system is attractive), it is most likely the black-body radiation from the heated flat surfaces of the pole pieces that heat up the droplet once the heater is turned on. It is found that a temperature of roughly 70°C or less (measured by a thermocouple (Omega WTK-6-36), located on Fig. 14(a)) is adequate to expedite the drying time, from hours to minutes, after the droplet is loaded and the turbo pump is started.

3.6.3 Gaining Control of Charge State

The charge in a big droplet can not be neutralized completely. The energy change associated with an additional charge in a large volume is smaller than that in a small volume, hence the amount of charge has a large uncertainty while the volume is large. As a result, the same amount of the leftover charge stays on a ~ 1000-fold shrunk volume after drying. This could potentially cause problems such as more eddy current lost (and hence a lower Q-factor) or even the particle being pulled out of trap because of electric force.

A mechanism for changing the charge state of the trapped particle "on the fly," after the particle has dried to its ultimate size is needed. Several approaches have been explored and are summarized in the following sub-sub-sections.

3.6.3.1 Second Radioactive Source Exposure Since the Americium-241 radioactive source works well in air, to reduce the net charge, it is only natural to mount it on the manipulator (Sec. 2.1.1) and bring it close to the droplet under vacuum, to see if it can change the charge state.

However, no change of the charge state was observed, for the source approximately 15 mm from the droplet for a few minutes, for a pressure as high as 100 mTorr. The speculations of this absence of action are one, the absence of current amplification from air ionization. Two, the ion beam can be much more directional than diffusive in vacuum, making it more difficult to align it towards the droplet.

3.6.3.2 Field Emission Point Electrons can be "squeezed out" of a metal surface with a strong electric field, generated from a sharp point biased with a high potential in vacuum [101]. This is adopted as one strategy to charge the trapped particle.

The field emission point is prepared by electrochemically etching a long, thin tungsten wire (Alfa Aesar 10408) in strong (≈ 10 M) sodium hydroxide water solution, while the wire is biased with a few volts positively and a large stainless steel sheet is kept grounded in the solution. The etching procedure takes a few minutes and is similar to those published [102, 103]. Figure 17(b) shows one such etched emission point under a microscope, the tip sharpness is $\lesssim 1$ μm.

Figures 14(a) and Fig. 17(a) show a emission point mounted and aimed at the trap, a few millimeters away.

The electrical connection is done via a high-voltage-rated electric feedthrough on the main chamber, as shown in Fig. 17(c). Note the heavy duty ceramic electrical insulation. In series with a large (10 MΩ) resistance, to limit any accidental shorting current to $\lesssim 200$ μA, the voltage is provided by a high voltage, low current power supply (Hewlett Packard 6516A) through an HV cable (Fig. 17(d)). Other wire connections are put in PTFE tubings to ensure insulation and hence safety. The voltage drop, if any, is monitored by a multimeter, e.g., a Fluke handheld model. Though the voltage drop would be on the order of tens of volts, the voltmeter must be able to float to a high potential, ~ 1000 V. Therefore, a Keithley digital multimeter would not be adequate. Also, the whole body of the multimeter is to be isolated from optical table, human hands, or any other conductive surfaces.

A turn-on of the field emission current is indeed observed, at a few micro-amps, and dried particles are charged more negatively. However, the turn-on threshold voltage seems to change dramatically and deteriorate each time. The voltage can be from -650 to -1200 V. Also, a lot of times the dried particle is knocked out as the field emission current turns on abruptly. The speculation of this inconsistency is that while the tip is at a negative high voltage, gas ions from a poor vacuum tend to crash into the tip, corroding the tip and making it duller or oxidized.

Furthermore, it would be ideal if a charging method can work to arbitrarily change the charge state, as opposed to going one-way. Biasing the field emission point to as high as $+1900$ V for about 10 minutes does not charge the particle in any way. This is expected from the large mobility difference between electrons and ions.

In summary, a field emission point provides a way to negatively charge the particle that is difficult to control.

3.6.3.3 UV Lamp – Side A UV lamp (185 nm) is used to radiate on the particle, and to cause atom to absorb photons and ionize the electrons, equivalently charging the particle positively. The lamp is powered again through the high voltage feedthrough, by a transformer (12 VDC input, maybe hundreds of volts output), with typical current of ~ 500 mA.

Figure 17(a) is a photograph of a side UV illumination configuration, while the UV lamp is

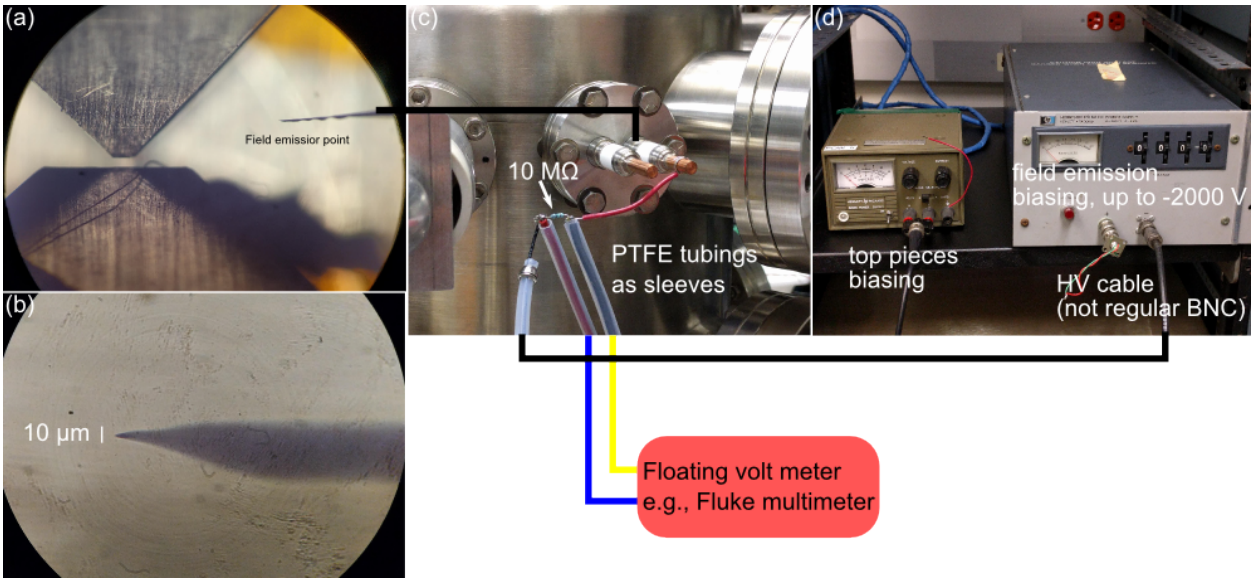

Figure 17: Field emission point setup. (a) The field emission point with the tip a few millimeters from the trap. (b) Zoom-in micrograph of the field emission point tip, showing the sharpness about few microns. (c) and (d) electric connections for the field emission point. A high voltage is sent from a power supply and is sent through properly insulated by polytetrafluoroethylene (PTFE) tubings and a high-voltage electric feedthrough. A 10 MΩ resistor is in series with the field emission point to restrict the current for safety and provide a checkpoint for current.

turned on. But it has been found that the particle is still exclusively negatively charged. The total time scale to see a significant charging is only ~ 10 seconds.

It is probably because the pole pieces, which are metal surfaces, absorb UV photons and emit photoelectrons (photoelectric effect,) which then accumulate on the particle. As a result, the particle is overwhelmed by the photoelectron charging, not UV ionization.

3.6.3.4 UV Lamp – Through Bottom Pieces A possible solution to this surface photoelectric problem is to eliminate as much as possible the UV photons hitting the flat surfaces of the trap, but still have a reasonable amount hitting the particle. Also, it is possible to use a metal mesh as a shield, and as the shield is biased differently, a particle behind the shield could be charged differently [104, 105].

Due to the limitation of the trap geometry, it is not possible to implement the metal shield. The closest attempt is shown in Fig. 17(b), where the UV lamp is in a "slanted" position. The major part that can expose the flat surfaces of the pole pieces is covered by kapton tape. The UV photons ideally would go through between the bottom pieces. Expected advantages are one, the bottom flat surfaces do not see the UV photons, while the trapped particle might still see through the gap. Two, when the top pieces is biased relative to the bottom pieces (kept grounded), the bottom pieces might be able to play the role of a shield.

Rather surprisingly, it works and charges the trapped particle positively. It was found, in repeated trials, now the particles are being positively charged, rather than negatively as before with side UV orientation. However, now it seems hard to charge the particle negatively. Once the top pieces are biased positively (to attract electrons out of the bottom pieces shield), and the UV is on, the particle is knocked out instantaneously. The charge polarity change of the particle is seen, not only by the biasing direction, but also by a lock-in, phase-sensitive detection. As shown in Fig. 18(c), a frequency synthesizer is set to bias the top pieces with a sinusoidal voltage, at, for example, 18 Hz, with some amplitude, say 0.2 V. It was seen that, for a initially negatively charged particle, the phase response decreases after the UV is turned on, crosses over zero, and increase in the opposite sign. This means that the charge has changed sign.

If UV lamps are set up in both positions described in the previous and this subsections, it should be possible to have an arbitrary sign control of the charge on the trapped particle.

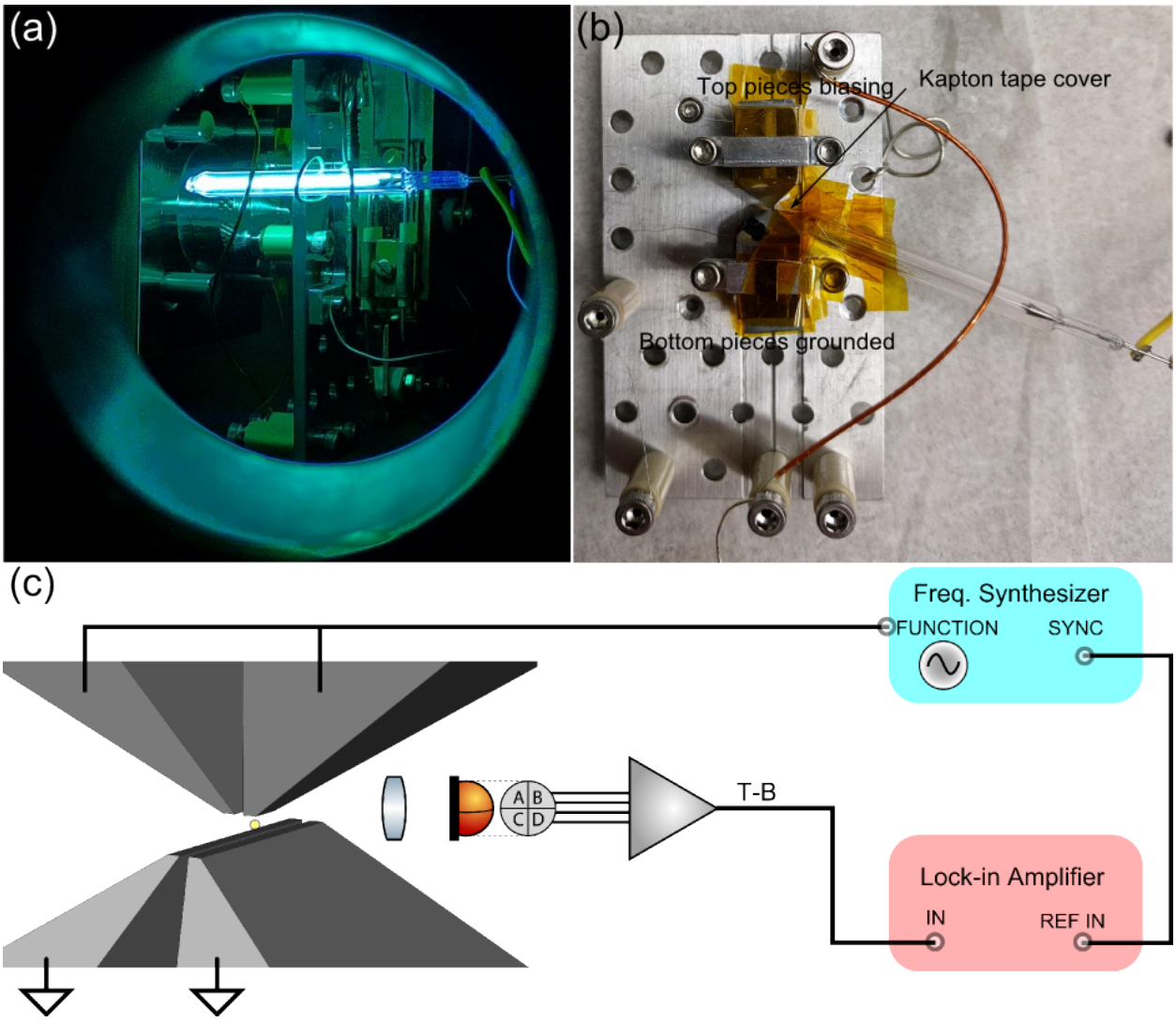

Figure 18: (a) A lit UV lamp in a side position. (b) A slanted UV lamp position with kapton tapes covering the direct light path. Light can only go through between the bottom pieces to reach the trapping region. (c) Set up for phase-sensitive detection while charging.

3.6.4 Loading a Single Droplet

One idea to make the loading process even cleaner is to use a drop-on-demand single droplet generator [106, 107, 108, 109]. This was considered, but not perused very far within this thesis work. This generator consists of a fine glass nozzle from a tube and a liquid chamber. A piezoelectric surface seals this chamber. As a controlled piezo surface pulse movement takes place, a droplet is pushed out from the nozzle. See Appendix E.12 for details.

4.0 MOTION DETECTION AND FEEDBACK COOLING

In this chapter, the experimental details of the trapped particle, including optics and electronics, is described. The fundamental formalism for motion detection is then derived. Survey of cooling techniques for trapped few-body systems in vacuum is presented. Finally, the detail of the linear feedback cooling used in this work, including theory and implementation, is explained and described.

4.1 OVERVIEW OF EXPERIMENT SETUP

Fig. 19 displays the arrangement of the key elements for motion detection and feedback cooling. The particle is illuminated with an 830 nm diode laser for position detection and an 520 nm laser for driving NV center photoluminescence (PL), each coupled through a single-mode fiber. See Fig. 20 for the complete map of the optical elements.

Collimated 830 nm and 520 nm light from single-mode fibers are combined and focused by a long focal length achromat ($f8$), to form a focused illumination spot with a large waist ($\approx$ 72.8 μm) and a long depth of focus ($\sim$ 10 mm). This is to fit the illumination light into the long axial trap length, and also to avoid excessive light pressure on the trapped particle. The 830 nm illumination intensity is typically $\approx$ 1 $\mathrm{nW}/\mu\mathrm{m}^2$. Scattered light and PL are collected by aspheric lens L1 (LightPath 355390-B), after which the scattered 830 nm light and the PL are separated by dichroic beamsplitter BS1. The PL passes through lenses L4 and L5 to compensate for the chromatic aberration of L1 and to couple the light into a multimode fiber for detection in the spectrometer, which consists of a scanning monochromator and single photon counting module (SPCM, Excelitas SPCM-AQRH-14-FC). The scattered 830 nm light is relayed by L2

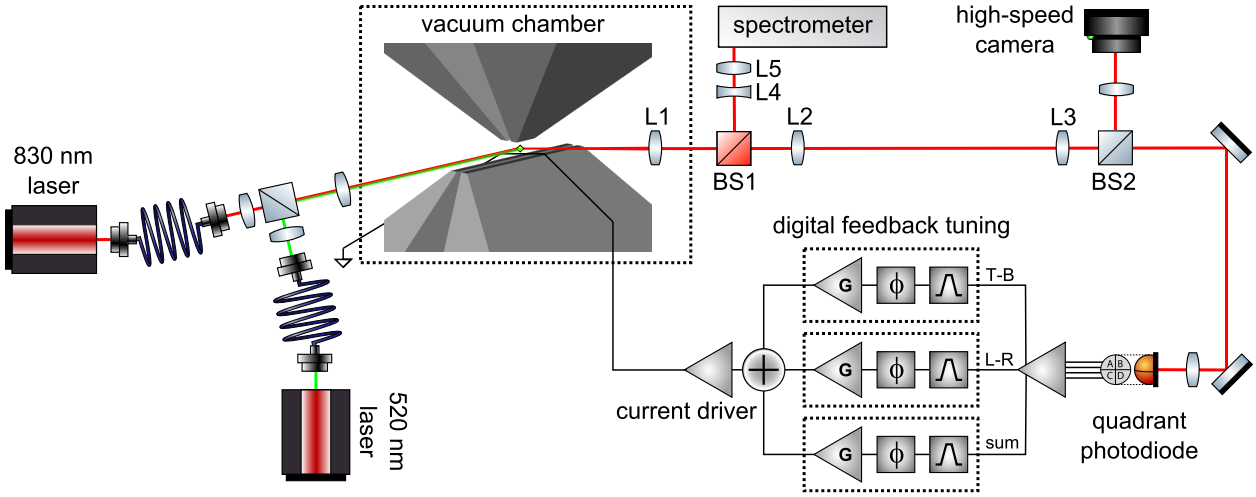

Figure 19: System diagram of trapped particle illumination, imaging, NV spectroscopy, and feedback cooling.

and L3 before being imaged onto the high-speed camera (Mikrotron MC1364) for recording the motion and a home-made position-sensitive detector (quadrant photodiode, Hamamatsu S5980) for feedback cooling with split vertical ($T - B = \text{top} - \text{bottom}$), axial ($L - R = \text{left} - \text{right}$) and transverse (sum) signals.

The light signal detected by the position-sensitive detector is converted to current and is processed again by a home-made amplifier circuit on a printed circuit board. The detail of the amplifier circuit can be found in Appendix E.6. These three position signals, $T - B$, $L - R$, and sum, then go through a series of filters and amplifiers, as shown in Fig. 21 and 22, so that only the signals in the relevant frequency range, $\lesssim 1$ kHz, are extracted and amplified. The "cleaned" signals then enter the microcontrollers for digital processing, either for display/recording or feedback cooling, which will be explained in later sections.

Figure 20: Complete optics setup diagram

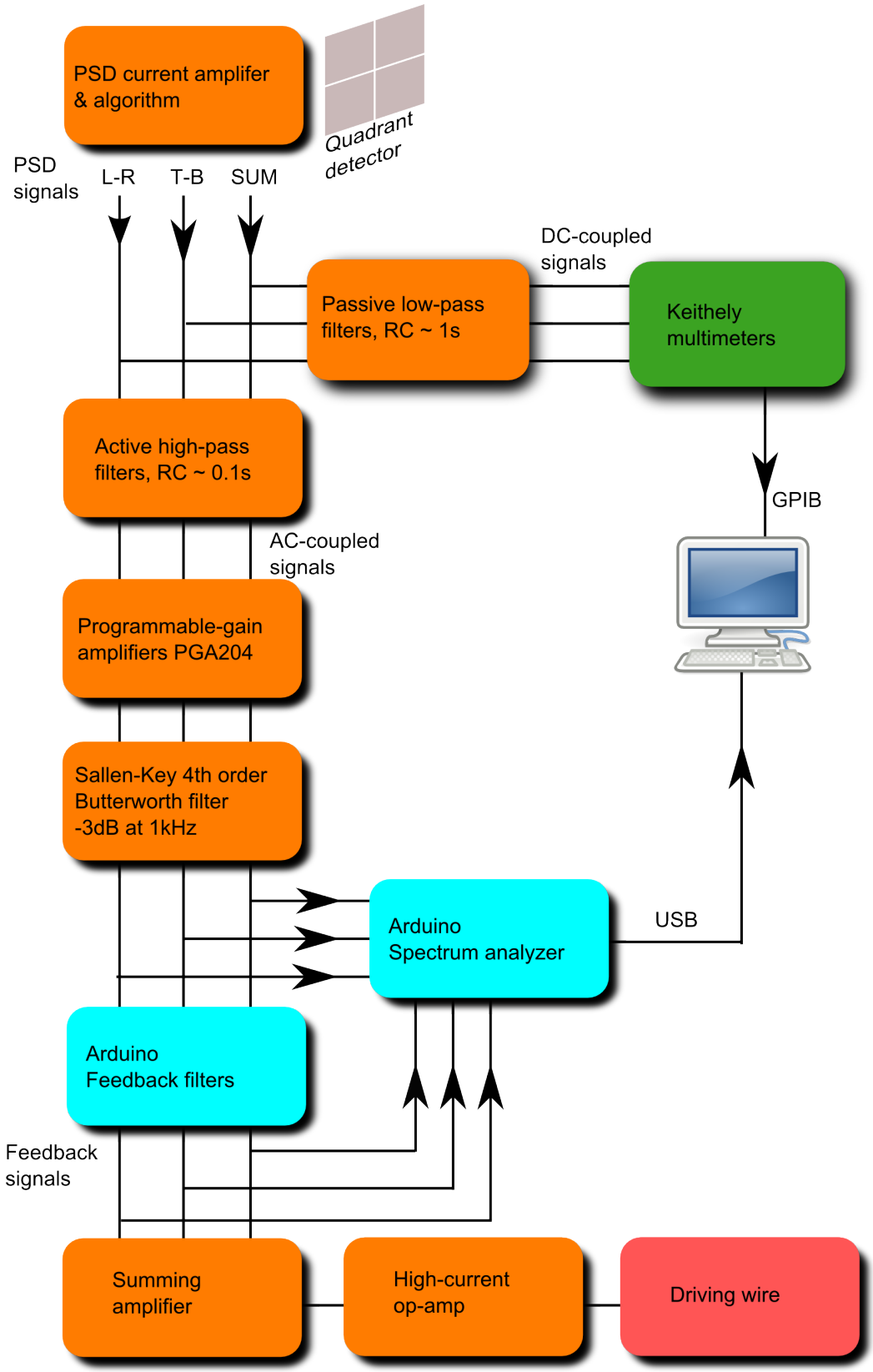

Figure 21: Detection and feedback electronics block diagram

Figure 22: Photograph of the detection and feedback electronics panel.

4.2 POSITION SENSITIVE DETECTOR - QUADRANT PHOTODIODE

4.2.1 Quadrant Photodiode

The position sensitive detector is based on a commercially available quadrant photodiode S5980 from Hamamatsu Photonics. As the name suggests, it has only four individual elements, or pixels. This model features small overall size (5 mm by 5 mm) and low noise (1.4×10^{-14} W/Hz$^{\frac{1}{2}}$) [110]. The small sensor size keeps the terminal capacitance low (10 pF) and hence the response fast. A transimpedance of 10 MΩ is chosen as the first stage amplification and conversion from current to voltage. See Appendix E.6 for the complete amplifier circuit design. This stage is especially important since the noise floor is determined at this point. The Johnson noise for a 10 MΩ resistor at 20° C for a 1 Hz bandwidth is about $V_n \sim 400$ μV, hence the noise power density is $V_n/R/\Delta f \sim 1.6 \times 10^{-14}W/Hz^{\frac{1}{2}}$. This noise level is almost matching the detector noise; when the transimpedance is higher, the Johnson noise will dominate. However, the detector's noise equivalent power of 1.4×10^{-14} W/Hz$^{\frac{1}{2}}$ is specified at the peak sensitivity wavelength. At other wavelengths, there is no indication that the noise will be higher or lower. Therefore, it might be worthwhile to increase the transimpedance for more gain, at the penalty of higher dominating Johnson noise.

4.2.2 Electronic Construction

The quadrant photodiode is solder-mounted on a custom-made board with solder paste (Quick Chip, SMD291AX) and heated manually by a solder iron (Fig. 23(a)). Connection wires are then soldered in the plated through holes (Fig. 23(b)).

Since the photodiode is sensitive to moisture, the host circuit board is designed to fit in a 1-in optics lens tube, e.g., Thorlabs SM105 and be sealed with an viton o-ring (#020) and a flat glass window (Thorlabs WG41050-B), with a few dry silica gel beads (Fig. 23(b)).

The wires leading to the pins on the quadrant photodiodes are then connected to a home-made amplifier and algorithm operator printed circuit. This printed circuit board is designed to fit in a 4-in long lens tube for 1-in optics, while the metal lens tube body is grounded, providing a electric shield from external noise. Figure 23(c) shows the wiring design of this circuit. After

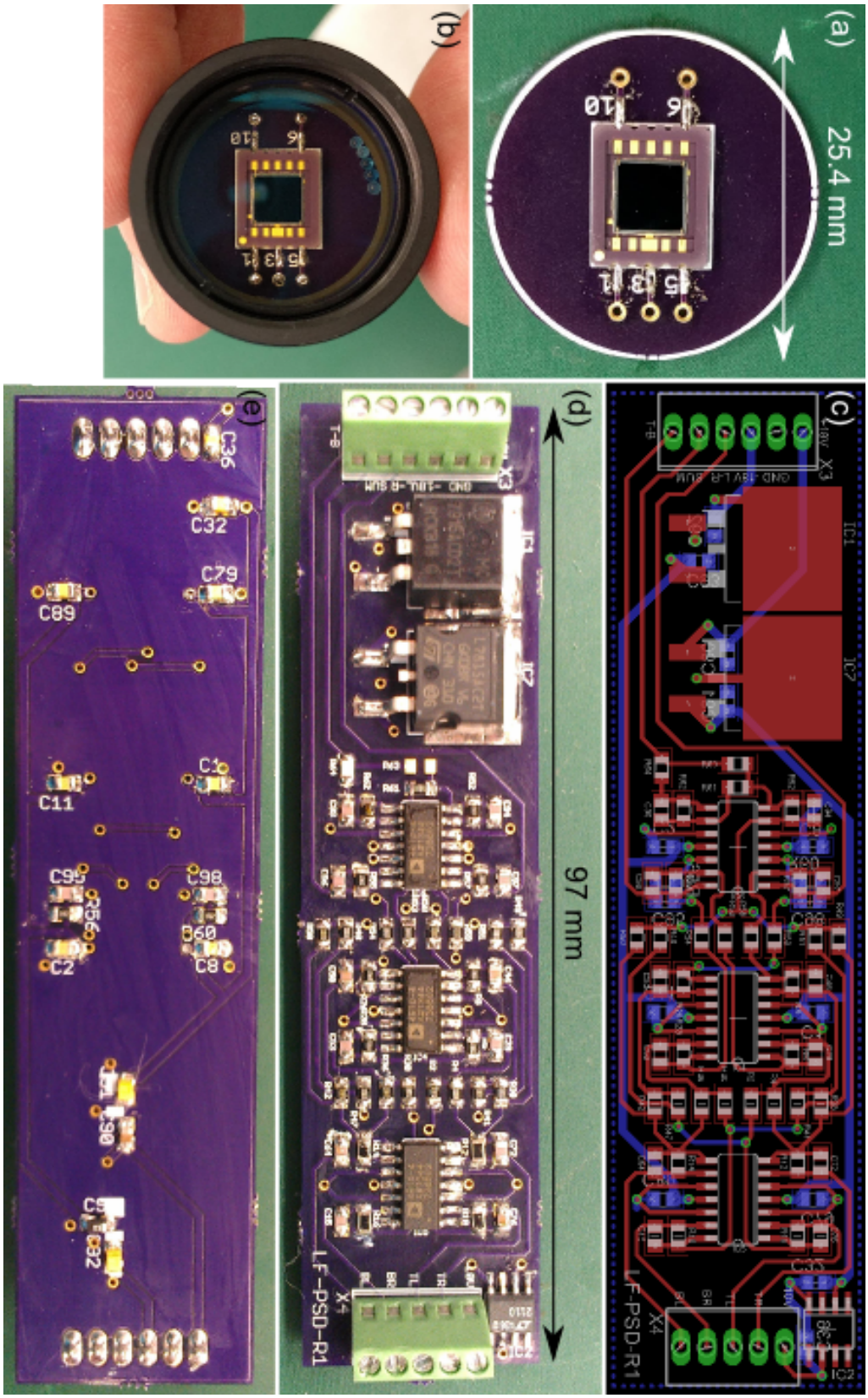

Figure 23: Quadrant photodiode in mount and the printed amplification circuit board

manufacturing of this circuit board by OSH Park, components are manually soldered onto them. Figure 23(d) and Fig. 23(e) are photographs of the actual built circuit.

4.2.3 Optical Interfacing

Collimated scattered light from the trapped particle is focused by a lens to form image onto the quadrant photodiode (Fig. 20). Detection of the trapped particle movement with the quadrant photodiode relies on the intensity difference between two sides, L and R, and T and B. The physical constraints are now the individual sensor size (2.5 mm by 2.5 mm) and the gap between sensors (0.030 mm) [110]. The fundamental idea is to maximize the linear detection range. When the focused image spot is smaller or comparable to the gap size, the detected signal is either zero (spot "hiding" in the gap) or a constant (spot moving totally on one sensor only). This is clearly the lower limit for the spot size. On the other hand, if the spot and the movement are large enough, such that the light misses the sensor when swinging over the outer edges, the difference signal strength will drop, but this will be confused with the signal of the particle moving back towards the center. This sets the upper limit for the spot size, but this is correlated with the movement range of the trapped particle, and this is especially prominent for the axial motion with weakest confinement.

With the choice of focusing lens for the position sensitive detector, together with the focal lengths of the objective and the relay lenses (Fig. 20), the total magnification of the trapped particle image on the quadrant photodiode is $\frac{f_4}{f_2}\frac{f_1}{f_o} \approx 110$. If the 30 μm gap is projected back to the trap area, it will be a $\sim$ 0.275 μm shadow. While the target particle size is around 1 μm, nearly factor of four larger in size is probably reasonable. Projecting the whole detector size, 5 mm back, the field of view is then about 46 μm. This is roughly consistent with common axial motion peak-to-peak amplitude when it is highly excited. This means that for an excited motion as large as about 46 μm, there is still chance to cool it reasonably fast.

Increasing f_4 can help enlarge the particle image for better linearity, but then the highly excited motion will be out of the field of view. Also, a focal length even longer than the current 300 mm would be inconvenient. However, when better cooling towards the quantum ground state is desired, the small motion right around the sensor gap will be important. In this case, the

magnification needs to be increased, and other technique shall be used to keep the particle from being overexcited axially.

4.3 MOTION CHARACTERIZATION

In this dissertation work, the quadrant position sensitive detector just described is used for feedback cooling, as this equipment has a fast response, but smaller linear range. The high-speed camera is used for accurate motional data acquisition, with only a small fraction (8%) of the collected light imaged onto it. All the remainder is imaged on the quadrant detector. The advantage of the high-speed camera is that with a large array of sensors (1280 by 1024) spanning a 17.9 mm by 14.3 mm area, the linear range is the entire array area.

The center-of-mass motion of the particle is analyzed by recording high-speed (496 frames per second) images of the scattered light and post-processing the images (using trackpy [111], which implements a widely-used particle tracking algorithm [112]) to track the motion of the particle in the axial and vertical directions, which are in-plane motion on the camera image. The overall intensity of scattered light reaching the camera or quadrant photodiode (sum) gives some information about the transverse motion as well, but the transverse cooling is typically less effective due to the poor linearity of the overall intensity with respect to the transverse displacement. After determining the trajectory of the particle with trackpy, the motion is analysed by one or more techniques to extract the temperature of the motion or the size of the particle, primarily with the power spectral density technique (PSD) [113].

4.3.1 Power Spectral Density of Trapped Particle Motion

This subsection considers a micron/nano-sized particle's motion in a three dimensional harmonic potential with air damping. The air environment provides both damping and incoherent force on particle.

The Newtonian equation of Brownian motion for a particle of mass m in a harmonic potential

is

$$m\ddot{x}(t) + \gamma_0\dot{x}(t) + m\omega_0^2 x(t) = \xi(t), \tag{4.1}$$

or

$$\ddot{x}(t) + \Gamma_0\dot{x}(t) + \omega_0^2 x(t) = \frac{1}{m}\xi(t), \tag{4.2}$$

where $\Gamma_0 = \frac{\gamma_0}{m}$ and ω_0 is the natural oscillation frequency of that degree of freedom.

The random force term $\xi(t)$ has two properties: averaging to zero and whiteness

$$\langle \xi(t) \rangle = 0; \;\; \langle \xi(t)\xi(t') \rangle = g\delta(t - t'). \tag{4.3}$$

$\langle \dots \rangle$ stands for ensemble average over implementations. The strength factor g will be determined by the normalization of the power spectral density later.

The Fourier transformed solution in the frequency domain is

$$\tilde{x}(\omega) = \int_{-\infty}^{\infty} e^{-i\omega t} x(t) dt, \tag{4.4}$$

and the inverse transformation is

$$x(t) = \frac{1}{2\pi} \int_{-\infty}^{\infty} e^{i\omega t} \tilde{x}(\omega) d\omega. \tag{4.5}$$

If expressing in oscillation frequency, $f = 2\pi\omega$, the transformation looks symmetric [114],

$$\tilde{x}(f) = \int_{-\infty}^{\infty} e^{-2\pi i f t} x(t) dt, \tag{4.6}$$

$$x(t) = \int_{-\infty}^{\infty} e^{2\pi i f t} \tilde{x}(f) df. \tag{4.7}$$

From Eq. (4.5) it is conveniently seen that the Fourier transforming of the time derivative of $x(t)$ is simply a factor in front of the transform of $x(t)$

$$\begin{aligned}
&\int_{-\infty}^{\infty} e^{-i\omega t}\dot{x}(t)dt \qquad (4.8)\\
&= \int_{-\infty}^{\infty} e^{-i\omega t}\frac{d}{dt}\left(x(t)\right)dt\\
&= \int_{-\infty}^{\infty} e^{-i\omega t}\frac{d}{dt}\left(\frac{1}{2\pi}\int_{-\infty}^{\infty} e^{i\omega t}\tilde{x}(\omega)d\omega\right)dt\\
&= \int_{-\infty}^{\infty} e^{-i\omega t}\left(i\omega\right)\left(\frac{1}{2\pi}\int_{-\infty}^{\infty} e^{i\omega t}\tilde{x}(\omega)d\omega\right)dt\\
&= \left(i\omega\right)\int_{-\infty}^{\infty} e^{-i\omega t}x(t)dt\\
&= \left(i\omega\right)\tilde{x}(\omega),
\end{aligned}$$

and similarly for $\ddot{x}(t)$.

Fourier transforming the equation of motion Eq. (4.2) gives

$$i\omega\left(i\omega\tilde{x}(\omega)\right) + \Gamma_0\left(i\omega\tilde{x}(\omega)\right) + \omega_0^2\tilde{x}(\omega) = \frac{1}{m}\tilde{\xi}(\omega). \qquad (4.9)$$

Solving for $\tilde{x}(\omega)$,

$$\tilde{x}(\omega) = \frac{\tilde{\xi}(\omega)}{m}\frac{1}{(\omega_0^2-\omega^2)+i\omega\Gamma_0}. \qquad (4.10)$$

The power spectral density (PSD)[1] is defined as the absolute value of $\tilde{x}(\omega)$ squared, divided by the measurement period, t_{msr},

$$\begin{aligned}
S(\omega) &= 2\left|\tilde{x}(\omega)\right|^2/t_{\text{msr}} \qquad (4.11)\\
&= \frac{2\left|\tilde{\xi}(\omega)\right|^2}{t_{\text{msr}}m^2}\frac{1}{\left(\omega_0^2-\omega^2\right)^2+\omega^2\Gamma_0^2}, \quad \omega > 0.
\end{aligned}$$

Note that the factor of 2 in Eq. (4.12) is due to the convention that the negative frequency part is thrown away when defining PSD.

[1]The power spectral density defined here has unit of $m^2{\cdot}s$, or m^2/Hz, which does not match Watts/Hz, as in electronics, and also the literal sense of power spectral density. However, this seems to be the convention in the literature.

Consider ensemble averaging of the random force squared term,

$$\begin{aligned}
\left\langle \left|\tilde{\xi}(\omega)\right|^2 \right\rangle &= \left\langle \int_{t=-t_{\mathsf{msr}}/2}^{t_{\mathsf{msr}}/2} e^{i\omega t}\xi(t)dt \int_{t'=-t_{\mathsf{msr}}/2}^{t_{\mathsf{msr}}/2} e^{-i\omega t'}\xi(t')dt' \right\rangle \\
&= \left\langle \int_{t=-t_{\mathsf{msr}}/2}^{t_{\mathsf{msr}}/2} \int_{t'=-t_{\mathsf{msr}}/2}^{t_{\mathsf{msr}}/2} e^{i\omega(t-t')}\xi(t)\xi(t')dt'dt \right\rangle \\
&= \int_{t=-t_{\mathsf{msr}}/2}^{t_{\mathsf{msr}}/2} \int_{t'=-t_{\mathsf{msr}}/2}^{t_{\mathsf{msr}}/2} e^{i\omega(t-t')} \left\langle \xi(t)\xi(t') \right\rangle dt'dt \\
&= \int_{t=-t_{\mathsf{msr}}/2}^{t_{\mathsf{msr}}/2} \int_{t'=-t_{\mathsf{msr}}/2}^{t_{\mathsf{msr}}/2} e^{i\omega(t-t')} g\delta(t-t')dt'dt \\
&= \int_{t'=-t_{\mathsf{msr}}/2}^{t_{\mathsf{msr}}/2} \int_{\tau=-t_{\mathsf{msr}}/2-t'}^{t_{\mathsf{msr}}/2-t'} e^{i\omega\tau} g\delta(\tau)d\tau dt' \\
&= g\int_{t'=-t_{\mathsf{msr}}/2}^{t_{\mathsf{msr}}/2} dt' \\
&= gt_{\mathsf{msr}}
\end{aligned} \tag{4.12}$$

Hence,

$$\langle S(\omega)\rangle = \frac{2g}{m^2}\frac{1}{\left(\omega_0^2-\omega^2\right)^2+\omega^2\Gamma_0^2}, \tag{4.13}$$

or,

$$\langle S(f)\rangle = \frac{2g}{m^2(2\pi)^4}\frac{1}{\left(f_0^2-f^2\right)^2+f^2\Gamma_{f0}^2}. \tag{4.14}$$

Experimentally, this means that averaging over many sets of data ("frames") smooths out the randomness in the force and asymptotically approaches the ensemble average. Eq. (4.14) is an experimental-data-friendly form, as the frequencies f_0, f and the damping rate $\Gamma_{f0} = \Gamma_0/2\pi$ are all in units of Hertz (Hz.)

The particle "eventually," i.e., after several damping times $1/\Gamma_{f0}$, reaches equilibrium with the environment and reaches energy k_BT. By equipartition theorem, on long time average, there will be $\frac{1}{2}k_BT$ in the potential energy. These statements imply

$$\frac{1}{2}k\left\langle x(t)^2\right\rangle = \frac{1}{2}m\omega_0^2\left\langle x(t)^2\right\rangle = \frac{1}{2}k_BT, \tag{4.15}$$

or,

$$\left\langle x(t)^2 \right\rangle = \frac{k_B T}{m\omega_0^2} = \frac{k_B T}{m f_0^2 (2\pi)^2} \tag{4.16}$$

And, by definition,

$$\left\langle x(t)^2 \right\rangle = \lim_{t_{\mathsf{msr}} \to \infty} \frac{1}{t_{\mathsf{msr}}} \int_{-t_{\mathsf{msr}}/2}^{t_{\mathsf{msr}}/2} |x(t)|^2 \, dt. \tag{4.17}$$

It is demanded by Parseval's theorem [115] that

$$\int_{-\infty}^{\infty} |x(t)|^2 \, dt = \int_{-\infty}^{\infty} |\tilde{x}(f)|^2 \, df. \tag{4.18}$$

Hence,

$$\int_0^{\infty} \langle S(\omega) \rangle \, d\omega = \lim_{t_{\mathsf{msr}} \to \infty} \frac{1}{t_{\mathsf{msr}}} \int_{-\infty}^{\infty} |\tilde{x}(\omega)|^2 \, d\omega \tag{4.19}$$

$$= \lim_{t_{\mathsf{msr}} \to \infty} \frac{1}{t_{\mathsf{msr}}} \int_{-t_{\mathsf{msr}}/2}^{t_{\mathsf{msr}}/2} |x(t)|^2 \, dt$$

$$= \left\langle x(t)^2 \right\rangle. \tag{4.20}$$

The relationship Eq. (4.20) puts a normalization constraint on g,

$$\int_0^{\infty} \langle S(f) \rangle \, df = \int_0^{\infty} \frac{2g}{m^2 (2\pi)^4} \frac{1}{\left(f_0^2 - f^2\right)^2 + f^2 \Gamma_{f0}^2} df \tag{4.21}$$

$$= \frac{2g}{m^2 (2\pi)^4} \int_0^{\infty} \frac{1}{\left(f_0^2 - f^2\right)^2 + f^2 \Gamma_{f0}^2} df$$

$$= \left\langle x(t)^2 \right\rangle = \frac{k_B T}{m f_0^2 (2\pi)^2}$$

Ref. [115] gives a nice derivation of the integral in Eq. (4.21),

$$\int_0^{\infty} \frac{1}{\left(f_0^2 - f^2\right)^2 + f^2 \Gamma_{f0}^2} df = \frac{\pi}{2 f_0^2 \Gamma_{f0}}. \tag{4.22}$$

Thus, from Eq. (4.21) and Eq. (4.22),

$$\frac{2g}{m^2 (2\pi)^4} \frac{\pi}{2 f_0^2 \Gamma_{f0}} = \frac{k_B T}{m f_0^2 (2\pi)^2}. \tag{4.23}$$

Finally, we have,

$$g = 4\pi k_B T m \Gamma_{f0}. \tag{4.24}$$

Rewriting the PSD from Eq. (4.14) once again,

$$\langle S(f)\rangle = \frac{k_B T \Gamma_{f0}}{2m\pi^3} \frac{1}{\left(f_0^2 - f^2\right)^2 + f^2\Gamma_{f0}^2} \tag{4.25}$$

$$= \left(\frac{k_B T}{2m f_0^2 \pi^3}\right) \frac{f_0^2 \Gamma_{f0}}{\left(f_0^2 - f^2\right)^2 + f^2\Gamma_{f0}^2} \tag{4.26}$$

Eq. (4.26) is the final form of the PSD used in the Python fitting to the experimental data.

Eq. (4.26) is checked against Eq. (27) in [113], except that the definition of PSD is off by a factor of 2.

Upon fitting data with Eq. (4.26), four physical parameters can be extracted – Center frequency f_0 (Hz), the damping rate Γ_{f0} (Hz), the ratio of temperature to the particle mass T/m, and the constant noise level.

Eq. (4.26) is an especially convenient form, as at the natural resonant frequency,

$$\langle S(f = f_0)\rangle = \left(\frac{k_B T}{2m f_0^2 \pi^3}\right) \frac{1}{\Gamma_{f0}}, \tag{4.27}$$

and it is easy to see that the overall factor $S_0 \equiv \left(\frac{k_B T}{2m f_0^2 \pi^3}\right)$ represents the area under the curve that is centered at the natural frequency f_0 with the width of Γ_{f0}.

Incidentally, setting the derivative of $\langle S(f)\rangle$ to be zero and finding where the maximum of $\langle S(f)\rangle$ occurs gives the damped resonant frequency $f_r = \sqrt{f_0^2 - \frac{1}{2}\Gamma_{f0}^2}$, a familiar result from classical mechanics [116].

4.4 DISCRETE FOURIER TRANSFORMATION (DFT)

Sec. 4.3.1 takes care of the continuous form of the PSD that is used to fit the experimental PSD data. This section deals with the procedure of converting the position data $x[k]$, recorded for a finite measurement period, t_{msr}, with a finite sampling frequency (or frame rate f_s), to the PSD data $\tilde{x}[n]$, using discrete Fourier transformation (DFT).

Suppose that the position data points $x[k]$ are already converted from pixel to actual length. Here k is the index of time, $t = k\Delta t$, and $\Delta t = 1/f_s$. Python implements the DFT [117] as

$$\begin{aligned}\tilde{x}[n] &= \sum_{k=0}^{N-1} x[k] e^{-i\left(\frac{2\pi n}{N\Delta t}\right)(k\Delta t)} \\ &= \sum_{k=0}^{N-1} x[k] e^{-i2\pi \frac{nk}{N}}.\end{aligned} \tag{4.28}$$

Here N is the total number of frames, so $N\Delta t = t_{\mathsf{msr}}$. n is the index for frequencies, $f_n = \frac{n}{N\Delta t}$. However, physically meaningful index stops at $n = N/2$, where the Nyquist frequency $f_{\mathsf{Ny}} = \frac{1}{2} f_s$.

From here to the actual PSD data points, for the curve fitting from Sec. 4.3.1 to be meaningful, scaling is to be done carefully. Parseval's theorem Eq. (4.18) and the normalization of PSD Eq. (4.20) are good guidance.

First of all, the variance of $x[k]$ (assuming $x[k]$ is centered, $\frac{1}{N}\sum_{k=0}^{N-1} x[k] = 0$),

$$\begin{aligned}\frac{1}{N}\sum_{k=0}^{N-1} (x[k])^2 &= \frac{1}{N\Delta t}\sum_{k=0}^{N-1} (x[k])^2 \Delta t \\ &= \frac{1}{t_{\mathsf{msr}}}\sum_{k=0}^{N-1} (x[k])^2 \Delta t \\ &= \left\langle x(t)^2 \right\rangle,\end{aligned} \tag{4.29}$$

is the discrete version of the mean-squared displacement Eq. (4.17).

Now to implement Eq. (4.20) in the discrete version,

$$\left\langle x(t)^2 \right\rangle = \frac{2\Delta t^2}{t_{\mathsf{msr}}} \sum_{n=0}^{N-1} |\tilde{x}[n]|^2 \Delta f. \tag{4.30}$$

Here Δf is the frequency resolution of the DFT, $\Delta f = 1/t_{\mathsf{msr}}$. It is an analog to df. Δt is an analog to dt in the Fourier transformation, since there is no Δt in the Python implementation. The factor of 2 is for the same reason as in Eq. (4.12), only positive frequencies.

With these "decorations", the definition of discrete PSD can be written,

$$
\begin{aligned}
S[n] &\equiv \frac{2\Delta t^2}{t_{\text{msr}}} \left|\tilde{x}[n]\right|^2 \\
&= \frac{2\Delta t^2}{N\Delta t} \left|\tilde{x}[n]\right|^2 \\
&= \frac{2\Delta t}{N} \left|\tilde{x}[n]\right|^2 \\
&= \frac{2\left|\tilde{x}[n]\right|^2}{N f_s}
\end{aligned}
\tag{4.31}
$$

Eq. (4.31) is checked against Eq. (24) in [118].

4.4.1 Power Spectral Density Results

At rough vacuum (over 1 mTorr), the motion of a particle in the magneto-gravitational trap is expected to be highly damped, and the temperature of that motion to be in thermal equilibrium with the gas surrounding it. Under high vacuum (5×10^{-8} Torr), the damping time can be minutes or longer, and the temperature of the mechanical motion of the particle is largely disconnected from room temperature. Due to the low stiffness of the trap, the thermal motion of the particle at ambient temperature is easily observed on the camera (see Appendix G).

Plots of the PSD of the motion of a diamond nanocrystal cluster are shown in Fig. 24 at several pressures. Pressures of 5 mTorr and higher were obtained by first pumping to high vacuum and then backfilling the chamber with nitrogen. The peak at 120 Hz is due to power line noise. The resonant frequency is around 10 Hz for the axial motion, about 130 Hz for the vertical, and roughly 105 Hz for the transverse.

These curves were obtained by averaging 30 frames of spectra, while each frame is a Fourier transformation of 10 seconds of recorded motion data, at a frame rate of 496 Hz. This is a particularly time-consuming process. Copying all the high-speed image files ($\approx 150,000$ of them and $\sim$ 10 GB total size) without a solid state drive and performing trackpy analysis takes many hours.

Assuming the motion is thermalized at ambient temperature (295 K) at pressures of 5 mTorr and higher, one can fit the PSD and extract S_0 to measure the mass of the particle, which for the

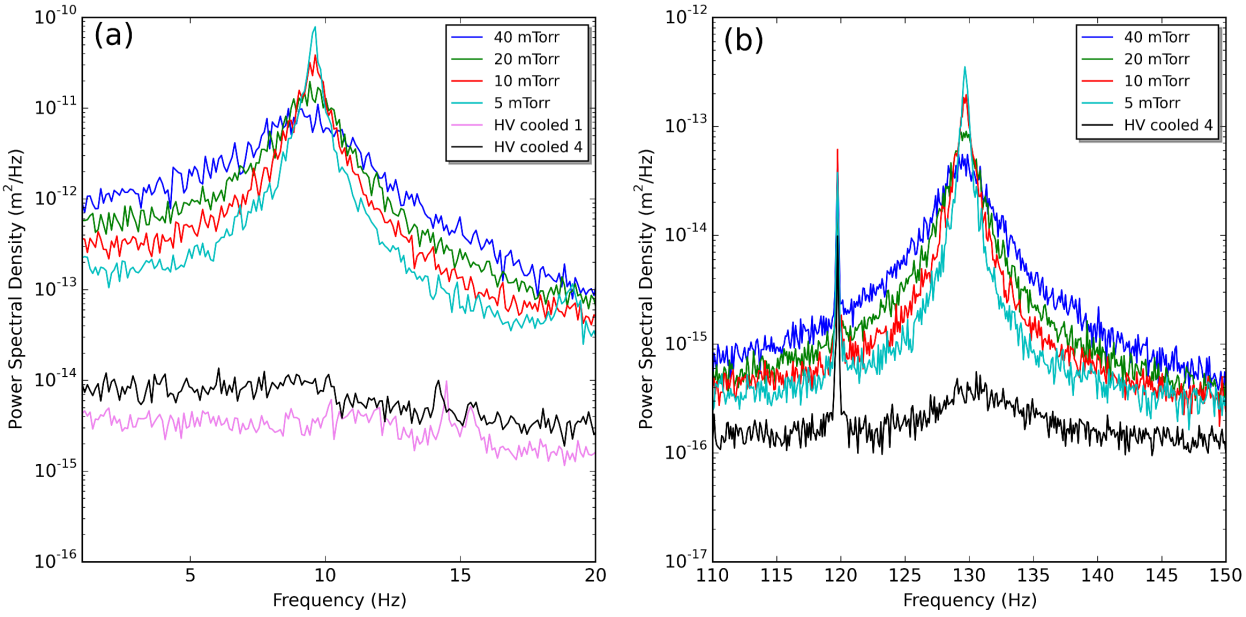

Figure 24: PSD and results of feedback cooling, (a) axial and (b) vertical. The best fittable cooling is 600 mK for axial (black curve) and 3 K for vertical.

data shown gives $m = 28$ pg (averaging the mass across axial and vertical motion at all rough vacuum pressures).

As the gas pressure is decreased, the damping rate of the motion of a trapped particle decreases, as can be seen by the increase in width of the resonance peaks in Fig. 24. At high vacuum, the damping is greatly reduced, and the center-of-mass motion is only weakly coupled to the environment. When manually optimised feedback cooling is added, the damping rate increases and the peak height decreases, as expected. The primary reason for using a diamond nanocrystal cluster instead of a single diamond nanocrystal is that the clusters remain trapped at all relevant temperatures, allowing simple calibration of the particle size and cooling. A smaller particle can be knocked out of the trap by the thermal energy at ambient temperature, and would require cold damping to keep it trapped. Such weakly trapped particles can still be loaded at room temperature by taking advantage of the low vapor pressure of DBS. This can begin by loading a large DBS droplet containing one nanodiamond, which is easily trapped at ambient temperature. The chamber can then be evacuated and the center-of-mass motion of the droplet

cooled before the DBS has evaporated. After complete evaporation of the DBS, the diamond nanocrystal would be left in the trap under high vacuum.

4.5 PARTICLE SIZE DETERMINATION

If the nanodiamond cluster were a densely packed sphere, this would correspond to a radius of 1.2 μm. Since it is likely a loosely packed cluster with significant porosity, the density is no longer the well-defined value for the material. Therefore, the usual calculation of the particle size from the damping rate with a background gas [119, 30, 120, 31, 74, 32, 38] would not be meaningful, because they all explicitly require both volume and mass.

4.6 PARTICLE IDENTITY

It is important to verify that the content in the trap is indeed diamond. To check the identity of the particles, the PL spectrum of the trapped particles is measured while pumping the NV centers with 520 nm laser light from the axial direction (see Fig. 19). Since the scattering force from the pump beam (with peak intensity ≈ 35 nW/μm^2) can easily drive the particle out of the trap, we pulse the pump beam and cool the mechanical motion of the particle back to near equilibrium after each excitation pulse (5 ms pump pulses, 2 Hz repetition rate). A recorded spectrum is shown in Fig. 25(b). The zero-phonon line (ZPL) may be less well-defined for trapped nanodiamonds than for those on a solid surface, possibly due to heating of the particle in the high vacuum environment [121, 37], even for the relatively weak pump beam used. A large (≈ 3.5 μm apparent size) cluster of nanodiamonds was used for the experiments reported here to ensure a strong PL signal. We have successfully trapped nanodiamond clusters with sizes down to ≈ 1 μm, typically with weaker PL signals but improved cooling of the center-of-mass motion.

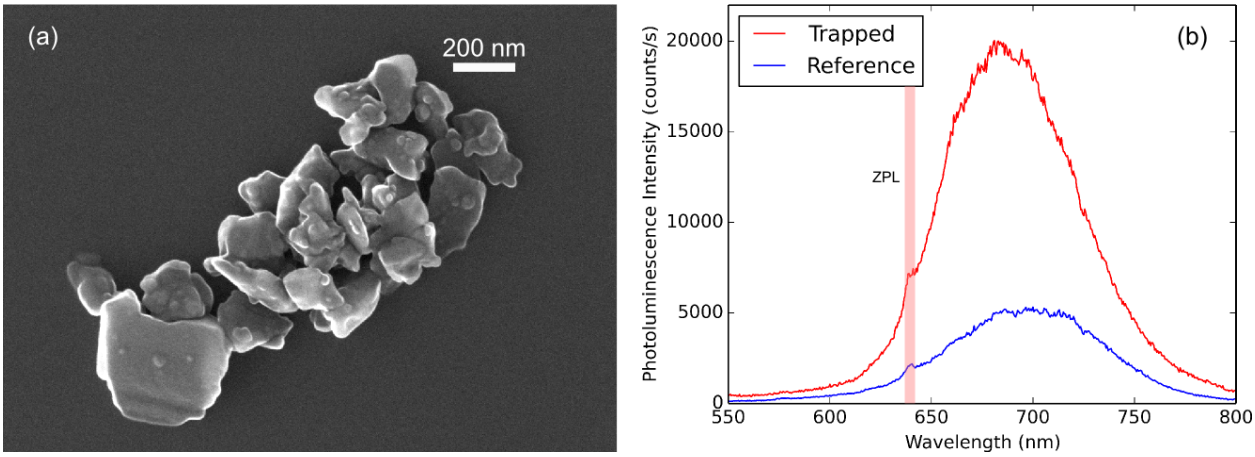

Figure 25: (a) Scanning electron microscope image of the nanodiamonds (Adámas Nanotechnologies ND-1600NV-140nm in isopropanol). (b) PL spectra of a trapped diamond nanocrystal cluster and a reference spectrum of diamond nanocrystals on a silicon substrate.

4.7 COOLING OF THE CENTER-OF-MASS MOTION

This section begins with a brief survey of cooling techniques that are commonly used in atom or ion trapping experiments, while a detailed review can be found elsewhere, for example, [122].

Linear feedback cooling, which is used in this dissertation work, is then introduced. The description of the complete feedback loop in this work and the cooling result follows.

4.7.1 Doppler Cooling

Doppler cooling, or radiation-pressure cooling, as its name suggests, utilizes the Doppler effect of laser frequency to achieve cooling [123, 124]. A trapped atom is irradiated by a laser, which is red-tuned from an electronic transition of the atom. Assuming the electron is in the lower energy state, as the atom moves towards the laser source, it "sees" the photon blue-shifted to match the electronic transition energy and absorbs the photon. This inelastic collision results in the atom losing some momentum. The atom later emits a photon and gains the same amount of momentum, but in a random direction. Over many absorption-emission cycles, the gaining of

momentum in random directions averages out, but the loss of momentum is in a consistent direction. Therefore, the center-of-mass temperature decreases. The limit on cooling is determined by the competition between the damping rate of Doppler cooling and the random momentum gain from emission in a short-time scale [125]. This limit on the ultimate temperature is usually higher than a single photon recoil heating temperature $T_{\text{recoil}} = \frac{\hbar^2 k^2}{2mk_B}$.

4.7.2 Parametric Feedback Cooling

Originally proposed by Cohen-Tannoudji [126] as "Sisyphus cooling," this cooling method for gas atoms won the Nobel Prize in 1997. The term "parametric" refers to the parameter of the trap, typically the trapping frequency. This method amounts to modifying the trapping parameter according to the detected phase information. The trapped particle then always sees a heightened potential wall as it moves away from the center, and as it moves towards the center, the trapping potential is turned down to lower the acceleration. The particle then keeps losing energy as it moves up and down hill.

One relevant implementation of this cooling method is the modulation of laser intensity in an optical trap for silica sphere in high vacuum. This approach has been demonstrated to cool the motion of the sphere to as low as $\bar{n} = 63$. [74, 77]

4.7.3 Sideband Cooling

Proposed again for ion trap experiments [127] and used extensively, this technique involves two degrees of freedom with transition frequencies ω_A and ω_B in one system. A drive at $\omega_d = \omega_A - \omega_B$ promotes a cross-transition from $|n_A, n_B\rangle$ to $|n_A + 1, n_B - 1\rangle$. Through spontaneous emission or other means of cooling the degree of freedom A and repeating the cycle, degree of freedom B can then be indirectly cooled. Here the A can be a two-state system, such as an electron's ground and excited states, or simply two levels of a harmonic oscillator. If ω_B is greater than the decay or damping rate of A, i.e., the "blur" of the energy level of A is less than ω_B, this sideband signal of $\omega_A - \omega_B$ is resolved, and hence a "resolved sideband cooling."

4.8 LINEAR FEEDBACK COOLING

The motion of the particle can be cooled with linear feedback, or simply feedback, of the detected motion using cold damping [128], which, in an ideal system, can be used to cool to the ground quantum state [129, 130].

A general equation for a driven damped harmonic oscillator reads

$$m\ddot{x}(t) + \gamma_0\dot{x}(t) + kx(t) = F_{\text{ext}}(t). \tag{4.32}$$

When the force is in the same or π rad out of phase with $x(t)$, i.e., $F_{\text{ext}}(t) = \pm k'x(t)$, the force modifies the resonant frequency,

$$m\ddot{x}(t) + \gamma_0\dot{x}(t) + (k \mp k')x(t) = 0, \tag{4.33}$$

When the force is in or π rad out of phase with the velocity $\dot{x}(t)$, i.e., $F_{\text{ext}}(t) = \pm\gamma_d\dot{x}(t)$, the force results in self-excitation ($+$, removing damping) or feedback cooling ($-$, increasing damping).

$$m\ddot{x}(t) + (\gamma_0 \mp \gamma_d)\dot{x}(t) + kx(t) = 0 \tag{4.34}$$

4.9 THE FEEDBACK LOOP

As shown in Fig. 21 and detailed electronics in Fig. 19, the complete feedback loop starts at the signal from the scattered light detected at the quadrant photodiodes. The electrical signals, after the processing for $L - R$, $T - B$, and sum, filtering and amplification, are monitored by an Arduino DUE (Monitor), to present the data to the user. Copies of signals for individual directions are fed to three additional respective Arduinos (Feedback-x,y,z, see Table 4) to digitally calculate the feedback output signal.

The movement signals are first digitized by the analog-to-digital converter (ADC) of Feedback-x,y,z, and then mixed with the internally generated oscillating signal at the LO Frequency (local oscillator frequency). The LO Frequency is set by the user to be very close to the frequency of the signal to be cooled. After low-pass filtering with the user-set bandwidth, IF Filter Width, the

Name	Board	Number of input/output	Short Description
Atomizer	Arduino DUE	0/1	Ultrasonic pulses for loading
Monitor	Arduino DUE	6/0	Monitors PSD and feedback signals
Feedback-x	Arduino DUE	1/1	Calculates feedback output, transverse
Feedback-y	Arduino DUE	1/1	Calculates feedback output, vertical
Feedback-z	Arduino DUE	1/1	Calculates feedback output, axial
Prog-amp	Arduino DUE	0/2	Controls programmable-gain amp
Counter	Arduino DUE	1/1	Controls the counter
TEC	Arduino DUE	2/2	TEC
Synthesizer	Arduino DUE	0/2	Gating of counter
Mono	Arduino Uno	0/1	Controls the monochromator

Table 4: List of all Arduinos

signal is amplified by Filter Gain. Afterward, the signals are phase-shifted and further amplified by Feedback Phase and Feedback Amplitude, respectively. The signals are then ready to be converted to analog signals by the digital-to-analog converter (DAC) and output.

Appendix F explains in detail the ADC_DAC code, which implements the feedback calculation. Table 5 summarizes the user-controlled feedback parameters and their functions.

Without any additional change, a Feedback Phase of 0 or 180 deg modifies the resonant frequency for an amount dependent on the Filter Gain and Feedback Phase. For a Feedback Phase of -90 or +90 deg, the output signals add or subtract from the natural damping, resulting in cooling or self-excitation, with strength again dependent on the Filter Gain and Feedback Phase. However, the direction of the feedback current, mirrors, electrical filters and amplifiers can all add to the phase difference between the detected and output signals. Therefore, the Feedback Phase will need to be tuned or scanned carefully according to the actual cooling performance, as opposed to following the nominal values.

The IF Filter Width, or simply the bandwidth in the frequency domain is related to how fast

Parameter Name	Description	Range
LO Frequency	Frequency of the signal to cool	n/a
IF Filter Width	Processing bandwidth	LO Frequency $>$ IF Filter Width$/2$
Filter Gain	First output amplification	powers of 2
Feedback Amplitude	Second output amplification	0 - 2.0, continuous
Feedback Phase	Phase shift of output	-180 - 180 deg

Table 5: Feedback Filter user-set parameters

the feedback output changes in the time domain to respond to new movement signals. The smaller the bandwidth is, the more heavily the output value is dependent on the past output value, so the slower it changes. The time scale is about $1/$bandwidth. Therefore, the bandwidth shall be at least larger than the damping rate, and is typically as large as about $1/10$ of the center frequency. This band setting should also avoid covering other signal peaks, or the $60/120$ Hz power lines.

4.10 DIAMOND COOLING RESULTS

Without analysis, the cooled particle appears to be stationary in high-speed videos. See Appendix G). Assuming the mass of the particle is the same as in the damped ambient-temperature measurements, PSD analysis shows the axial motion of the particle is cooled to 600 mK before the resonance peak becomes undetectable, while the vertical motion is cooled to 3 K with the strongest feedback. See Fig. 26 for the fitting and Table 6 for the full results with fitted parameters. The lowest recordable temperature for the axial motion is limited by the noise in the high-speed images used for analysis, while the vertical cooling is limited by need to avoid broadening the resonance too far, as the power line noise at 120 Hz would interfere with cooling. These results are published in [44].

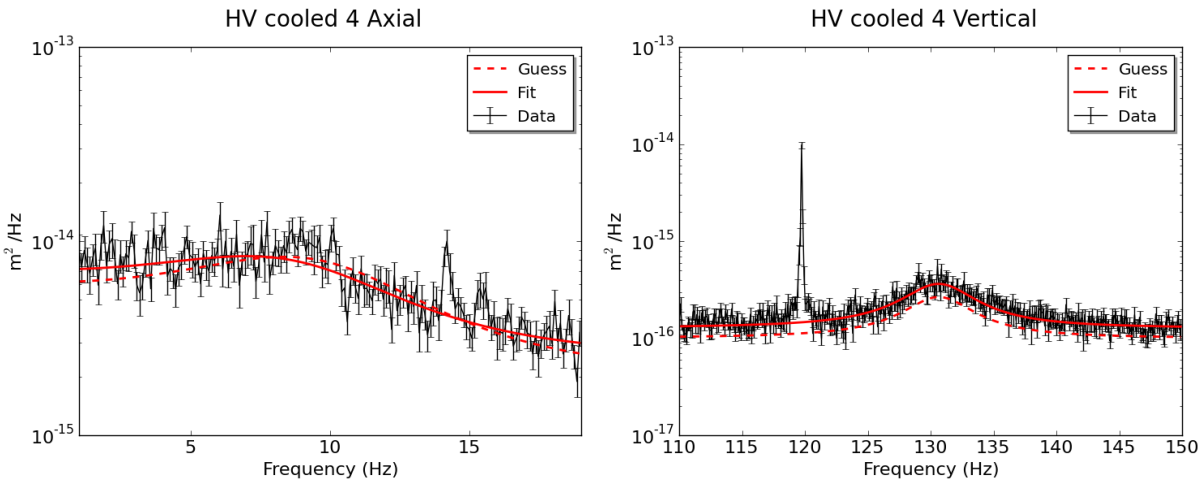

Figure 26: Lorentzian fits of cooled motions in axial and vertical directions

4.10.1 Position Distribution of a Thermalized Particle

A particle in a harmonic potential in the z axis possesses energy of

$$E = \frac{1}{2}mv^2 + \frac{1}{2}kz^2. \tag{4.35}$$

E of the degree of freedom z in thermal equilibrium with the environment follows a Boltzmann distribution, giving

$$P(z,v) \propto \exp(-E/k_BT) = \exp\left\{-\frac{1}{k_BT}\left[\frac{1}{2}mv^2 + \frac{1}{2}m(2\pi f_0)^2z^2\right]\right\}, \tag{4.36}$$

where $P(z,v)$ is the probability density of finding the particle at position z with velocity v, k_B is the Boltzmann constant, T is the temperature of the degree of freedom being measured, and m is the mass of the particle. In contrast, an isolated harmonic oscillator intuitively prefers the turning points [131],

$$P_{\text{isolated}}(x,E) = \frac{1}{\pi}\sqrt{\frac{k}{2E-kx^2}}, \tag{4.37}$$

where k is the spring constant and E is the total mechanical energy.

Pressure (Torr)	Direction	f_0(Hz)	Γ_{f0}(Hz)	S_0 (μm^2)	Mass(pg)	T(K)
40.2	Axial	9.64 ± 0.02	3.39 ± 0.05	24.5 ± 0.3	28.8 ± 0.4	assumed 295
40.2	Vertical	129.53 ± 0.02	3.56 ± 0.06	0.151 ± 0.00	25.9 ± 0.3	assumed 295
40.2	Transverse	104.03 ± 0.04	3.2 ± 0.1	n/a	n/a	assumed 295
20.1	Axial	9.56 ± 0.01	1.67 ± 0.03	23.3 ± 0.3	30.8 ± 0.4	assumed 295
20.1	Vertical	129.56 ± 0.02	1.75 ± 0.04	0.146 ± 0.002	26.9 ± 0.4	assumed 295
20.1	Transverse	104.03 ± 0.02	1.66 ± 0.05	n/a	n/a	assumed 295
9.95	Axial	9.58 ± 0.01	0.87 ± 0.02	23.5 ± 0.5	30.5 ± 0.6	assumed 295
9.95	Vertical	129.65 ± 0.01	0.91 ± 0.03	0.149 ± 0.004	26.3 ± 0.7	assumed 295
9.95	Transverse	104.05 ± 0.01	0.87 ± 0.02	n/a	n/a	assumed 295
4.99	Axial	9.57 ± 0.01	0.40 ± 0.01	25.9 ± 0.7	27.7 ± 0.7	assumed 295
4.99	Vertical	129.66 ± 0.01	0.47 ± 0.02	0.150 ± 0.006	26.0 ± 1.0	assumed 295
4.99	Transverse	104.10 ± 0.01	0.44 ± 0.02	n/a	n/a	assumed 295
HV cooled 1	Axial	can not fit	n/a	n/a	n/a	n/a
HV cooled 1	Vertical	129.90 ± 0.05	6.2 ± 0.1	$(2.62 \pm 0.08) \times 10^{-3}$	assumed 27.8	5.51 ± 0.18
HV cooled 1	Transverse	105.28 ± 0.06	n/a	n/a	n/a	n/a
HV cooled 4	Axial	10.3 ± 0.2	10.6 ± 0.6	0.046 ± 0.003	assumed 27.8	0.60 ± 0.05
HV cooled 4	Vertical	130.72 ± 0.08	6.3 ± 0.3	$(1.5 \pm 0.1) \times 10^{-3}$	assumed 27.8	3.17 ± 0.21
HV cooled 4	Transverse	105.00 ± 0.01	n/a	n/a	n/a	n/a

Table 6: Full results for particle 20160318. HV stands for high vacuum at 5×10^{-8} Torr.

Since only the position distribution is of interest, v can be integrated out, leaving the probability density for z,

$$P(z) \propto \int_{v=0}^{\infty} dv \exp\left\{-\left[\frac{1}{2}mv^2 + \frac{1}{2}m(2\pi f_0)^2 z^2\right]/k_B T\right\} \tag{4.38}$$

$$= P_0 \exp\left[-\frac{1}{2}m(2\pi f_0)^2 z^2/k_B T\right], \tag{4.39}$$

with normalization constant P_0. Eq. (4.39) is a normal distribution of z, and implies a linear relationship between the log of $P(z)$ with z^2,

$$\log\left[P(z)/P_0\right] = -\frac{m(2\pi f_0)^2}{2k_B T} z^2 = -\left(\frac{1}{\pi S_0}\right) z^2, \tag{4.40}$$

with $S_0 = \dfrac{k_B T}{2\pi^3 m f_0^2}$. The normalisation property of a Gaussian distribution can be used to determine the proportionality constant P_0,

$$\int_{-\infty}^{\infty} dz P(z) = P_0 \int_0^{\infty} dz \exp\left[-\left(\frac{1}{\pi S_0}\right) z^2\right] \tag{4.41}$$

$$= P_0 \sqrt{\frac{\pi}{\left(\frac{1}{\pi S_0}\right)}} \tag{4.42}$$

$$= \pi P_0 \sqrt{S_0}. \tag{4.43}$$

The integral is equal to the total number of occurrences, N, hence

$$P_0 = \frac{N}{\pi\sqrt{S_0}}. \tag{4.44}$$

In an experiment, when N high-speed camera images are analyzed, the number of times we will find the particle with a displacement between $z - \Delta z/2$ and $z + \Delta z/2$ is

$$P(z)\Delta z = \frac{N\Delta z}{\pi\sqrt{S_0}} \exp\left[-\left(\frac{1}{\pi S_0}\right) z^2\right], \tag{4.45}$$

where the constant P_0 has been replaced with the proper normalizaton and S_0, defined in Sec. 4.3.1, is a value determined from fitting the PSD of the motion.

Fig. 27 shows a typical distribution with predicted curve from Eq. (4.45). The measured z distributions and the expected distributions using S_0 from fitting the PSD measurements are plotted in Fig. 27. The distribution measurements match the prediction of the PSD fitting over a wide range, validating the PSD measurements and indicating that the assumption of thermal equilibrium of the motion is reasonable. The disagreement for large displacement could be due to the anharmonicity of the trap.

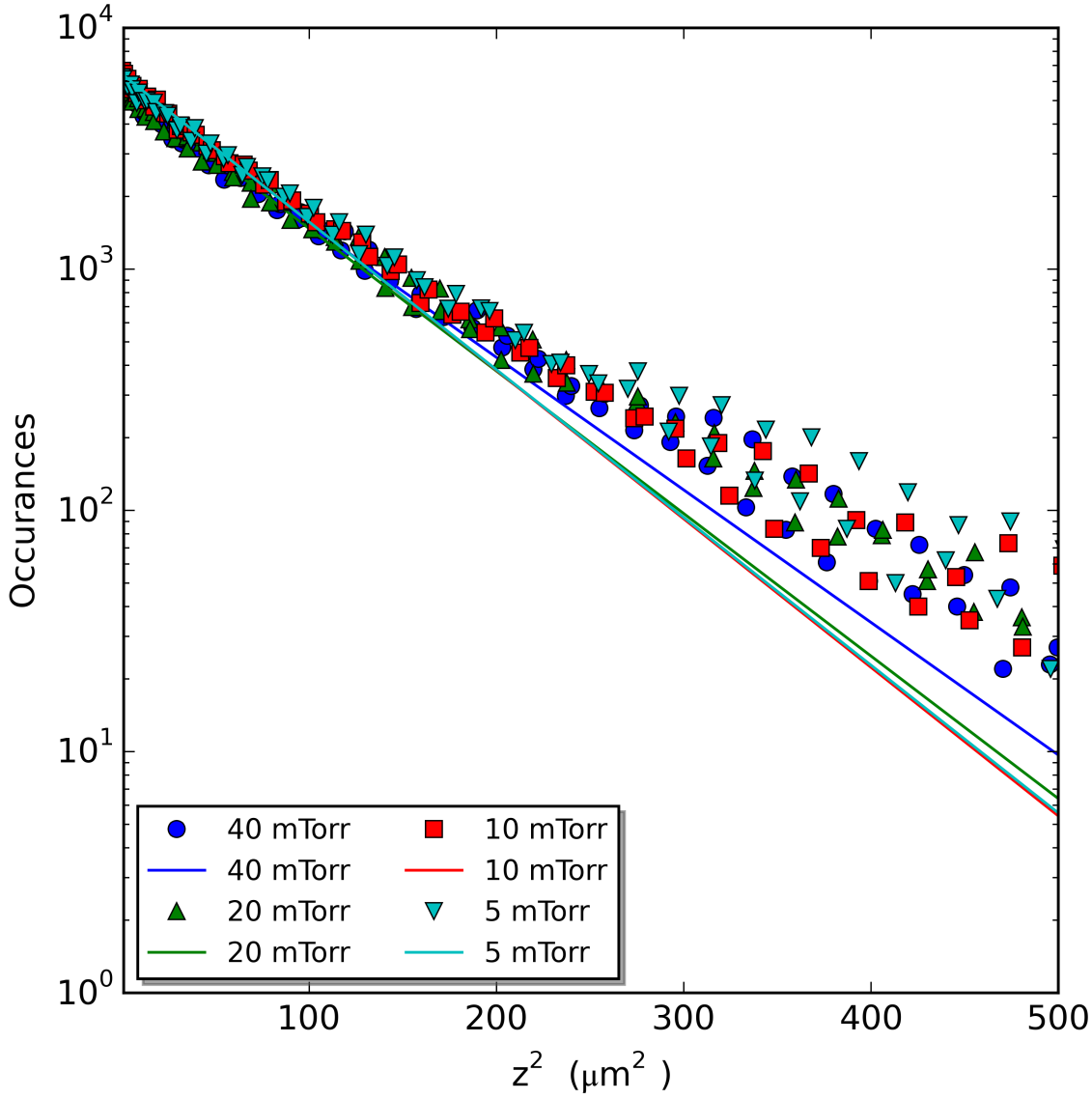

Figure 27: Distribution of the axial position.

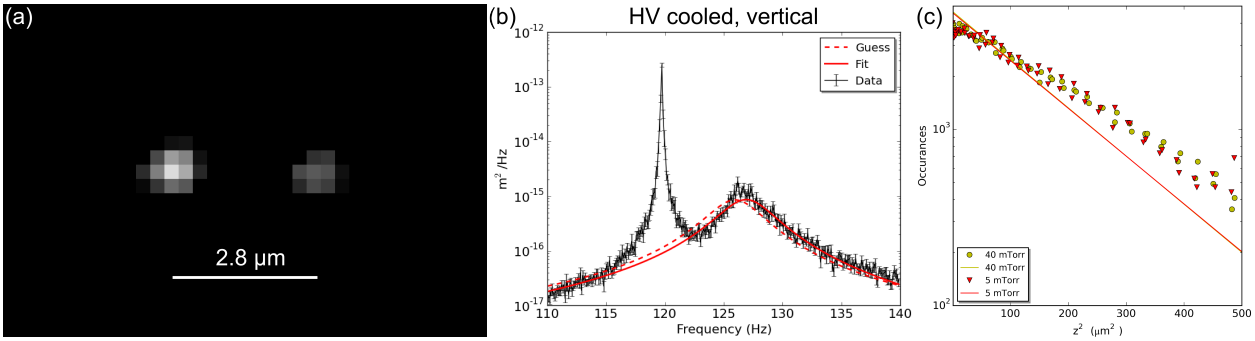

Figure 28: (a) Camera image of the silica bead cluster. 1 px $= 0.259$ μm. (b) Lorentzian fit of the cooled vertical motion. (c) Distribution of the axial position for the silica bead cluster.

4.11 SILICA SPHERE COOLING RESULTS

The preliminary results of the cooling of a cluster of 1 μm silica spheres (Thermo Fisher 8100, nominal diameter 1 μm) are summarized here.

The apparent size of this silica bead cluster is about 2.8 μm in diameter, as shown in Fig. 28(a).

PSDs of the axial and vertical motions at various pressures are plotted in Fig. 29.

The resonant frequencies, damping rate, and the mean-squared displacement can be fitted. With the density of the spheres 2010 kg/m^3, as specified by the 8100 data sheet, the mass of the whole cluster can be derived as well. The results are in Table 7.

Compared with the result for a diamond cluster, Sec. 4.10, this silica cluster is about a factor of 4 smaller in mass, corresponding to 8 to 9 individual spheres stuck together.

The vertical cooling performance can be fitted explicitly, as shown in Fig. 28(b), and the result is again in Table 7, 2.6 K, slightly better than the best practice for diamond. On the other hand, the PSD for the cooled axial motion seems to be overdone, a flat curve around the resonant peaks at higher pressures. Consequently and unfortunately, the cooling can not be fitted without ambiguity.

In order to gain some rough estimate for the axial cooling, the bump around 15 Hz in

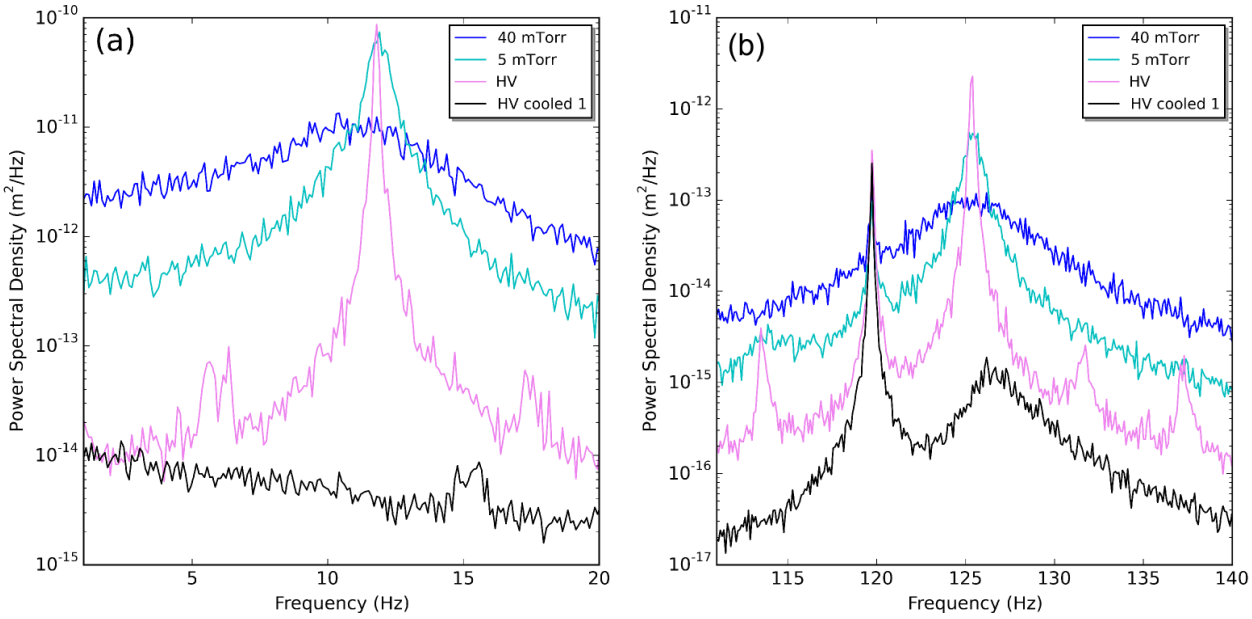

Figure 29: PSD and results of feedback cooling for a cluster of silica spheres, (a) axial and (b) vertical.

Pressure (Torr)	Direction	f_0(Hz)	Γ_{f0}(Hz)	S_0 (μm^2)	Mass(pg)	T(K)
40	Axial	11.81 ± 0.04	5.6 ± 0.1	50.6 ± 0.6	9.3	assumed 295
40	Vertical	125.41 ± 0.03	5.59 ± 0.09	0.526 ± 0.005	7.9	assumed 295
40	Transverse	99.17 ± 0.04	6.6 ± 0.1	n/a	n/a	assumed 295
5	Axial	11.919 ± 0.009	0.85 ± 0.02	51 ± 1	9.1	assumed 295
5	Vertical	125.37 ± 0.01	0.98 ± 0.03	0.48 ± 0.01	8.7	assumed 295
5	Transverse	98.97 ± 0.01	1.06 ± 0.03	n/a	n/a	assumed 295
HV cooled 1	Axial	can not fit	n/a	n/a	n/a	n/a
HV cooled 1	Vertical	126.95 ± 0.04	4.8 ± 0.1	$(4.13 \pm 0.07) \times 10^{-3}$	assumed 8.75	2.6
HV cooled 1	Transverse	n/a	n/a	n/a	n/a	n/a

Table 7: Full results for particle 20160506.

Fig. 29(a), HV cooled 1, can be used to set a upper bound for the effective temperature for the cooled particle. This bump can be represented by a Lorentzian of $f_0 = 15.4$ Hz, $\Gamma_{f0} = 0.4$ Hz, and $S_0 = 1.7 \times 10^{-15}$ m^2. Therefore, the effective temperature would be $\lesssim 16$ mK, an improvement of about 37-fold than that in Sec. 4.10.

Figure 28(c) shows the axial position distributions. Similarly, there are large discrepancies for large displacements.

5.0 TOWARDS QUANTUM GROUND STATE AND BEYOND

The cooling results presented in Chapter 4 is clearly still some distance away from the oscillator's quantum ground state. This chapter analyzes the quantum aspects of this system, including order-of-magnitude estimations and various mechanisms currently preventing the cooling from getting down to the ground state. The hope is that these analyses can provide some insight into the path towards cooling to the quantum ground state.

5.1 LIMITS ON COOLING PERFORMANCE

This section takes a "Top-down" or classical approach to examine the limits on the cooling performance, including damping by air and the detector noise.

5.1.1 Damping by Air

The collision of the trapped particle with background gas molecules at an average rate classically damps out the harmonic oscillation, and quantum mechanically destroy the quantum coherence of the state.

The following estimations for the damping rate and quality factor as function of pressure is based on the formalism in [30]. In this work, a spherical shape is assumed.

For air molecules, the product of mean-free path and pressure is 6.7×10^{-3} m·Pa, or 5.03×10^{-5} m·Torr. At atmospheric pressure, the mean-free path is less than a typical particle size, 100 nm - 1 μm, meaning collisions happen too often to estimate Q with the method in [30]. See Table 5.1.1. Below 100 mTorr, which is very easily achievable, the trapped particle

"sees" the air molecules as ballistic particles as opposed to a continuum, hence it is safe to use the formalism.

In [30], damping rate is connected to the environment and particle parameters as

$$\gamma_g = (8/\pi)(P/vr\rho), \tag{5.1}$$

where P and v are background gas pressure and mean speed, respectively. r and ρ are trapped particle radius and density, respectively. For air molecule, $v = \sqrt{3RT/M_{\rm air}} = 508$ m/s at $T = 300$ K. The collision rate $R_{\rm coll} \approx \pi P v r^2/k_B T$ is the rate the system is hit by actual gas molecules. The mechanical quality Q factor is related to the damping rate by $Q_g = \omega_m/\gamma_g$. The characteristic time $\tau_g = \hbar\omega_m/\gamma_g k_B T$ is for the system to be heated by one phonon. A phonon is the smallest unit of interaction with environment. The meaning of the characteristic time for the system to heat by one phonon starting from the ground state $\tau_g = \hbar\omega_m/\gamma_g k_B T$ then is the time next phonon hits the the trapped particle, in an average sense. This time is also the coherence time, because when an external phonon hits the particle, the quantum state of the system is destroyed. On the other hand, when an actual air molecule collides with the trapped particle, many many phonons can be transferred. Though the collision rate is rare, the number of phonons transferred is huge. In a similar concept, the number of coherent oscillations $N_{\rm osc}^{(g)} \equiv \omega_m \tau_g/2\pi$ measures in how many cycles a quantum experiment has to be done before the next coherence-destroying collision. If $N_{\rm osc}^{(g)}$ is smaller than one, the trapped particle appears as a free particle in the relevant time scale. On the other hand, if $N_{\rm osc}^{(g)}$ is many, it means that the oscillating nature of the trapped particle is relevant.

Incidentally, Eq. 5.1 can be used to determined the particle size in the trap, if it is a solid one and the damping rate is experimentally measured. See Sec. 4.5 for alternative ways of size determination.

Pressure (Torr)	Mean-free path	Particle Size	γ_g (Hz)	τ_g (s)	Q_g	$N_{\rm osc}^{(g)}$	Collision rate (Hz)
760	66 nm ($< r$)	1 μm	N/A	N/A	N/A	N/A	N/A
0.1	500 μm	1 μm	76.3	2.10×10^{-14}	0.82	2.10×10^{-13}	3.8×10^{10}
		100 nm	763	2.10×10^{-15}	0.082	2.10×10^{-14}	3.8×10^{8}
10^{-3}	50 mm	1 μm	0.76	2.10×10^{-12}	82.3	2.10×10^{-11}	3.8×10^{8}
		100 nm	7.63	2.10×10^{-13}	8.23	2.10×10^{-12}	3.8×10^{6}
10^{-5}	5 m	1 μm	0.0076	2.10×10^{-10}	8×10^{3}	2.10×10^{-9}	3.8×10^{6}
		100 nm	0.076	2.10×10^{-11}	823	2.10×10^{-10}	3.8×10^{4}
10^{-7}	500 m	1 μm	7.6×10^{-5}	2.10×10^{-8}	8.2×10^{5}	2.10×10^{-7}	3.8×10^{4}
		100 nm	7.6×10^{-4}	2.10×10^{-9}	8.2×10^{4}	2.10×10^{-8}	3.8×10^{2}
10^{-9}	50 km	1 μm	7.6×10^{-7}	2.10×10^{-6}	8.2×10^{7}	2.10×10^{-5}	3.8×10^{2}
		100 nm	7.6×10^{-6}	2.10×10^{-7}	8.2×10^{6}	2.10×10^{-6}	3.8

Table 8: Table of collision rates as a function of system pressure.

5.2 HARMONIC OSCILLATOR IN THE QUANTUM GROUND STATE

5.2.1 Basics of a Harmonic Oscillator

The Hamiltonian of a harmonic oscillator is

$$\hat{H}_m = \hbar\omega_m \left(\hat{a}^\dagger \hat{a} + \frac{1}{2}\right), \tag{5.2}$$

where $a^\dagger$ and a are the creation and annihilation operators, respectively. The eigenstates are the number states, or Fock states,

$$\hat{H}_m |n\rangle = E_n |n\rangle = \hbar\omega_m \left(\hat{n} + \frac{1}{2}\right) |n\rangle . \tag{5.3}$$

For a harmonic oscillator, e.g., $\omega_m = 2\pi \times (100$ Hz), in equilibrium with the environment, i.e., 300 K, the thermal energy would fill the oscillator's energy level up to an average occupancy number

$$\bar{n} = \frac{k_B T}{\hbar\omega} = \frac{1.38 \times 10^{-23} \times 300}{1.055 \times 10^{-34} \times 2\pi \times 100} \sim 10^{11}. \tag{5.4}$$

This is just an estimation, not meaning that the oscillator at room temperature is in a Fock state of a huge number. Rather, this is obviously best described by classical mechanics.

Mass for a sphere is $m = \frac{4}{3}\pi r^3 \rho$; for diamond, density is 3500 kg/m^3. Measured ω is at the

diameter	m(kg)
1 μm	1.83×10^{-15}
100 nm	1.83×10^{-18}

order of $2\pi\times$(100 Hz). k then can be estimated. See Table 5.2.1.

diameter	k(N/m)
1 μm	7.2×10^{-10}
100 nm	7.2×10^{-13}

Table 9: Masses and spring constants of diamond particles 1 μm and 100 nm in size.

5.2.2 Quantum Ground State of a Harmonic Oscillator

In the ground state, $n = 0$, the system posses a non-zero energy of $\frac{1}{2}\hbar\omega$. Semiclassically, an oscillation amplitude can be calculated from this ground state energy,

$$\frac{1}{2}\hbar\omega_m = \frac{1}{2}m\omega_m^2 A_{zp}, \tag{5.5}$$

and hence $A_{zp} = \sqrt{\frac{\hbar}{m\omega_m}}$. The peak-to-peak amplitude $A_{zp,p-p} = 2A_{zp} = 2\sqrt{\frac{\hbar}{m\omega_m}}$ stands for the amplitude of the motion that can be detected. For a 100-nm diamond, the $A_{zp,p-p}$ of ~ 0.6 nm (see Table 10) is a pretty large number, very tempting to try to measure. This is largely due to the very low frequency of our system.

diameter	$A_{zp,p-p}$(pm)
1 μm	19
100 nm	610

Table 10: Zero-point motion amplitudes of diamond particles 1 μm and 100 nm in size.

In the root-mean-square sense, a zero-point fluctuation x_{zp} is associated with this ground state energy. It also reflects the uncertainty relationship, which demands the "spread" of measurements of position x and momentum p are fundamentally restricted to

$$\Delta x \Delta p \geq \frac{1}{2}\hbar. \tag{5.6}$$

Using the equal sign, $\Delta p = \frac{\hbar}{2\Delta x}$, it can be seen that the energy due to just the uncertainty Δx and Δp gives rise to the ground state energy, if $\Delta x = \sqrt{\frac{\hbar}{2m\omega_m}}$,

$$E_0 = \frac{\Delta p^2}{2m} + \frac{1}{2}k\Delta x^2 = \frac{\hbar^2}{8m\Delta x^2} + \frac{1}{2}m\omega_m^2\Delta x^2 = \frac{1}{2}\hbar\omega. \tag{5.7}$$

Therefore, the zero-point fluctuation $x_{zp} = \sqrt{\frac{\hbar}{2m\omega_m}}$. Note that $x_{zp} = \frac{1}{\sqrt{2}}A_{zp}$, consistent with the understanding that x_{zp} is the averaged spread of the position measurement at the ground state, while A_{zp} is the amplitude.

5.3 COOLING TO THE QUANTUM GROUND STATE

Cooling to the quantum ground state amounts to removing energy from the oscillator until only $\frac{1}{2}\hbar\omega_m$ is left that can not be removed. In a feedback cooling scheme, the particle's motion, particularly its amplitude and phase or velocity, is measured and used to determine the cooling external force. Light is needed to be scattered off the oscillator in order to inquire about the oscillator's motion. The detected signal, or photon count, has the fundamental shot-noise source, originating from the discrete nature of photons. Uncertainty in the photon count $N_{\rm scat}$ is proportional to its own square root, $\sqrt{N_{\rm scat}}$. This, therefore, contributes to the uncertainty in the momentum by

$$\Delta p = \sqrt{N_{\rm scat}}\hbar k, \tag{5.8}$$

where k is the light wave number.

More photons improves the relative noise ($\propto \sqrt{N_{\rm scat}}/N_{\rm scat} = 1/\sqrt{N_{\rm scat}}$) and hence the uncertainty in the position measurement. This is consistent with the uncertainty relationship, in an ideal case,

$$\Delta x = \left(\frac{\hbar}{2}\right)/\Delta p = \frac{1}{2k\sqrt{N_{\rm scat}}}. \tag{5.9}$$

However, while the particle has the full momentum transfer uncertainty $\sqrt{N_{\rm scat}}\hbar k$, the number of photons received for position measurement is only $\eta N_{\rm scat}$, with η the overall light collection efficiency, i.e., including objective numerical aperture NA, loss in the subsequent lenses, quantum efficiency of the photodetector, etc.,

$$\Delta x = \left(\frac{\hbar}{2}\right)/\Delta p = \frac{1}{2k\sqrt{\eta N_{\rm scat}}},\ \ 0 < \eta < 1. \tag{5.10}$$

Therefore, combining the above two, the uncertainty in the energy can be estimated,

$$\Delta E = \frac{\Delta p^2}{2m} + \frac{1}{2}m\omega_m^2\Delta x^2, \quad \text{or} \quad \Delta E/\hbar\omega_m = \frac{N_{\rm scat}\hbar k^2}{2m\omega_m} + \frac{m\omega_m}{8k^2\hbar\eta N_{\rm scat}}. \tag{5.11}$$

Eq. (5.11) can be expressed in a more convenient way, by a number of photons that would result in recoil heating, ticking the occupation number up by 1 before the cooling is able to remove them. The condition is

$$N_{\text{recoil}}\frac{\hbar^2k^2}{2m} = \hbar\omega_m, \quad \text{or} \quad N_{\text{recoil}} = \frac{2m\omega_m}{\hbar k^2}. \tag{5.12}$$

So, the energy uncertainty can be re-written as

$$\Delta E/\hbar\omega_m = \frac{N_{\text{scat}}}{N_{\text{recoil}}} + \frac{N_{\text{recoil}}}{16\eta N_{\text{scat}}}. \tag{5.13}$$

Figure 30 is a visualization of Eq. (5.11), with various collection efficiencies. It can be seen that ground state cooling can be achieved only if the light collection efficiency is greater than $1/9$ ($\eta > 11\%$) and that the illumination intensity is adjusted to reach the standard quantum limit.

Assuming the minimal efficiency for ground state cooling of $\eta = 1/9$, $N_{\text{scat}} = \frac{1}{4\sqrt{\eta}} = \frac{3}{4}N_{\text{recoil}}$, i.e., if the light collection is poor, the laser power needs to be cranked high to really close to heating up the oscillator from the ground state. In this limit, Table 11 tabulates the order of magnitude of N_{scat}, with the recoil heating N_{recoil} defined in Eq. 5.12. ω_m is approximated as 100 Hz, and with the choice of 830 nm as illumination wavelength, $k = \left(\frac{2\pi}{\lambda}\right) = 7.57\times10^6$ m^{-1}.

The signal processing is typically done in a 1 - 10 Hz bandwidth in this dissertation work, as explained in Sec. 4.9. This means that the time window for the the scattering-measuring-cooling cycle is from 0.1 to 1 seconds. Therefore, numbers of photons in these peroids in Table 11 correspond to $\sim\ 10^{-13}$ to 10^{-9} W of optical power.

Technological limits would present here a trade-off between the target zero-point motion size and the detectable power. Using a smaller particle ($\sim\ 100$ nm) promises a large motion to detect, but the light level ($\sim$ 0.1 pW) will be close to the electronic noise of many commercially-available photodiodes and operational amplifiers, for example, the photodiode used in this work [110]. Incidentally, the low mass and low frequency restrict the optimal power for optical detection in this dissertation work to be battling with the detector noise, or more generally, sensing noise. In other mechanical systems for sensitive motion detection, for example, the LIGO detector for gravitational waves, the optimal power for detection is 70 W [132]. At this scale, the limits are the optical distortion caused by absorption in the optics, and heating of the lens, etc.

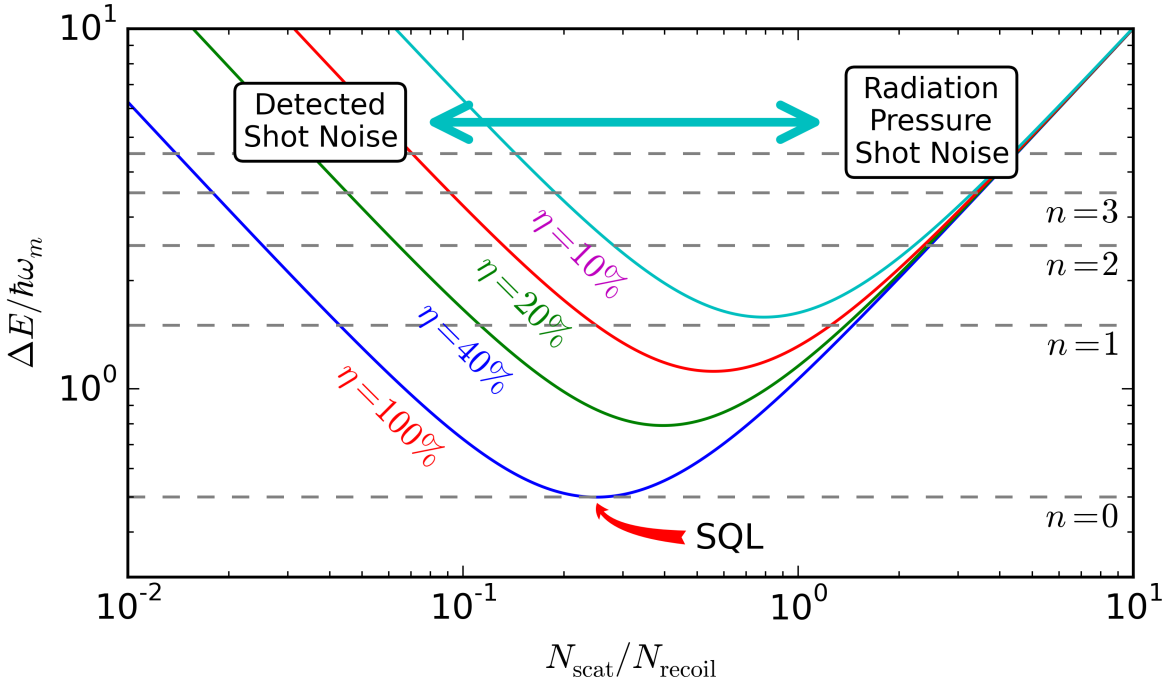

Figure 30: Energy uncertainty curve for various light collection efficiencies η. The minimum between the noise-induced uncertainty is called the standard quantum limit (SQL). For a fixed η, the uncertainty curve reaches the minimum when the ratio $\frac{N_{\rm scat}}{N_{\rm recoil}} = a_{\rm min} = \frac{1}{4\sqrt{\eta}}$. This η can achieve ground state cooling if $\Delta E/\hbar\omega_m = a_{\rm min} + \frac{1}{16\eta a_{\rm min}} < 1 + \frac{1}{2}$, meaning that the energy uncertainty is less than the energy of the first excited state. This condition poses a lower limit for the efficiency, i.e., $\eta > 1/9$.

diameter	N_{scat}^{SQL}
1 μm	3×10^{8}
100 nm	3×10^{5}

Table 11: Order-of-magnitude estimates of the number of photons needed to be scattered, N_{scat}, off the trapped particle in SQL, for various particle sizes.

5.4 EXPERIMENTAL DETECTION OF GROUND STATE MOTION

For a zero-point motion of $\sim$ 1 nm, how easy or how hard is it to detect and identify its energy being below the first excited state? In other words, what is the "smoking gun" signal that is showing cooling below $\left(1+\frac{1}{2}\right)\hbar\omega$?

In a noise-free ideal case (other than the quantum measurement uncertainty), the zero-point motion still exhibits a Lorentzian shape in the frequency domain, with an area under the curve equal to the mean-square displacement (MSD)

$$\left\langle x(t)^2\right\rangle = \left(\frac{\pi}{2}\right) S_0, \tag{5.14}$$

where S_0 is a parameter defined in Sec. 4.3.1. And semi-classically, the total mechanical energy E is related to the MSD,

$$E = \frac{1}{2}kA^2 = m\omega_m^2 \left\langle x(t)^2\right\rangle = m\omega_m^2 \left(\frac{\pi}{2}\right) S_0. \tag{5.15}$$

Assuming that the oscillation frequency ω_m can be measured with less uncertainty, the relationship between the energy uncertainty and the MSD uncertainty is

$$\Delta E = m\omega_m^2 \left(\frac{\pi}{2}\right) \Delta S_0. \tag{5.16}$$

With, for example, the would-be-dominant shot-noise in SQL, the noise strength is proportional to $N/\sqrt{N} = 1/\sqrt{N}$. From the analysis in Sec. 5.3, taking the best case of $N = N_{\mathrm{scat}}^{SQL} = 10^8$, the signal-to-noise ratio is 10^4. Therefore, if the S_0 is detected to be with an uncertainty less than $S_0/10^4$, the cooling is reliably working to achieve ground state.

5.5 POSSIBLE COUPLING SCHEMES BETWEEN A NMO AND ANOTHER NMO, AND NV, OR A CAVITY

5.5.1 Harmonic Oscillators Interaction - Cat Coding

If one harmonic oscillator is to be prepared into a Schrödinger's cat state, which is a superposition of macroscopically distinguishable states, another harmonic oscillator can be used as a readout subsystem. For a magnetically trapped particle system, this is very simple, since there are three spatial modes of harmonic oscillators. Suppose the vertical mode is used as the "storage" oscillator, $\omega_s = \omega_v$, and the axial mode is used as the "readout", $\omega_r = \omega_a$. An external drive ("pump") at $\omega_p = 2\omega_s - \omega_v$ enables a two-phonon coupling of the storage with the readout. This can pump the storage into a cat state if the storage is initially prepared in a Fock number state $|n\rangle$, [133, 134]

$$|\psi\rangle = \mathcal{N}\left(|+\alpha\rangle + |-\alpha\rangle\right), \tag{5.17}$$

where $|\alpha|^2 = n$.

5.5.2 Harmonic Oscillator - Spin Interaction

Three different types oscillator - spin interaction, based on different magnetic field distributions, are introduced below.

5.5.2.1 Uniform Field, Angular Motion

The interaction takes the form

$$H_I = g\mu_B B_{\text{ext}}(S_y \sin\theta + S_z \cos\theta). \tag{5.18}$$

For small angular oscillations with respect to the external field, $\cos\theta \approx 1 - \frac{1}{2}\theta^2$. This can implement quantum non-demolition (QND) measurement between a harmonic oscillator and a spin.

5.5.2.2 Linear Field Gradient, Translational Motion

Suppose there is a linear magnetic field gradient near the trap center. This would of course be much weaker than the trap field, in order not to alter the oscillation frequency too much. In the case when the NV axis is aligned with the gradient direction, the interaction Hamiltonian reads:

$$H_I = g\mu_B a_0 \vec{\nabla} B_{\text{ext}} \cdot \hat{r} S_z (a_m + a_m^\dagger). \tag{5.19}$$

This linear coupling enables a prepared Fock state to evolve simultaneously into two superpositioned states when the trapping strength is changed non-adiabatically. A protocol of Schrödinger's cat generation has been proposed using this type of interaction [5].

5.5.2.3 Quadratic Field Gradient, Translational Motion

A quadratic field gradient

$$H_I = \frac{1}{2} g\mu_B \left(\nabla^2 B_{\text{ext}}\right) S_z x^2 \tag{5.20}$$

can be used create QND measurement for translational oscillation motion. This is particularly important and useful for this experiment geometry, since it deals with translational oscillation, and the quadrupole magnetic field is actually quadratic in at least two directions. See Sec. 3.3 for the detail of trap field expansion.

5.5.3 Stroboscopic QND

Monitoring of the position of a harmonic oscillator in general is not a QND measurement, as

$$H = \frac{\hat{p}^2}{2m} + \frac{1}{2} m\omega_m^2 \hat{x}^2, \tag{5.21}$$

and $[\hat{x}, H] \neq 0$. However, taking advantage of the periodicity of the motion, there is a way to have repeated position measurement without disturbing the system after each measurement [29, 135, 136]. For a harmonic oscillator, the commutator of position measurement at different times is

$$[\hat{x}(t), \hat{x}(t+\tau)] = i\frac{\hbar}{m\omega} \sin \omega\tau. \tag{5.22}$$

This commutator vanishes every half period after the first measurement. Therefore, a readout, or interaction Hamiltonian of the form

$$E_0 \sum_n \delta\left(t - \frac{n\pi}{\omega}\right) \hat{x}\hat{q}, \tag{5.23}$$

i.e., turned on only every half period, can be employed to track the position of particle while leaving the quantum state undisturbed. In experiment, this amounts to pulsing the illumination light only at the half periods.

However, the phase of the oscillator at the moment of the position measurement is also important. Just as a sinusoidal oscillation with a phase ϕ can be broken down to two quadratures,

$$\sin(\omega t + \phi) = \cos\phi \sin(\omega t) + \sin\phi \cos(\omega t), \tag{5.24}$$

the time evolution of the position and momentum operators, $\hat{x}$ and $\hat{p}$, of a harmonic oscillator are

$$\hat{x}(t) = \hat{x}(0)\cos(\omega t) + \frac{\hat{p}(0)}{m\omega}\sin(\omega t) \tag{5.25}$$

$$\hat{p}(t) = \hat{p}(0)\cos(\omega t) - m\omega\hat{x}(0)\sin(\omega t). \tag{5.26}$$

While the amplitude of the cosine term in Eq. 5.25 is determined after measurement of $\hat{x}$, the sine term, i.e., the momentum, is disturbed infinitely, from the uncertainty relation.

As a classical understanding, the measurement is turned on while the oscillator is at an arbitrary phase. This phase is then decomposed to two oscillating parts, one at the turning or extreme point and the other just passing the equilibrium. The measurement photons hitting the extreme-point particle does no work (since there is no movement), hence no "disturbance." On the other hand, the photons on the equilibrium-point quadrature does the maximal work since the velocity is maximal.

6.0 OTHER EXPLORED APPROACHES

For completeness of documentation of this dissertation work, previous attempts for a well-behaved quantum nanomechanical system are summarized in this chapter. Divided into sections, clamped graphene film devices, optical trap, bottle beam trap, and three-piece magnetic trap are described. Due to various reasons elaborated below, these systems did not present good enough qualities for continued effort.

6.1 SUSPENDED GRAPHENE DEVICES

A suspended graphene beam with a nanodiamond attached on top in an external magnetic field has been proposed as a nanomechanical oscillator-NV coupling system for quantum measurement experiments [137]. This approach is one of Shonali Dhingra's dissertation work foci [138].

Excessive phase noise has been observed in this type of system, limiting the quality factor Q. One possible contribution to this issue is the clamping of the graphene film to the fabricated trenched substrate [138]. This might be improved if a patterned silicon dioxide/silicon wafer is used as a substrate, since the roughness of the polished wafer surface can be sub-nanometer, at least one order of magnitude smaller than a diamond lathe-machined surface.

6.1.1 Graphene

The graphene used in this research is synthesized in D'Urso Group's own lab. The procedures and various attempts are again described in Shonali Dhingra's dissertation [138] and a journal article [47].

The graphene produced in this lab also benefited a few collaborations, within the University and outside. For example, the collaboration with Professor Jeremy Levy's group at Pitt integrates graphene, a two-dimensional semi-conducting sheet, with the interface between lanthanum aluminate ($LaAlO_3$) and strontium titanate ($SrTiO_3$), a novel material interface demonstrating many properties under different conditions. This collaboration produced many useful and interesting results [49, 50], and fed back to improve the transferring techniques of graphene [51].

6.1.2 Fabrication of Suspended Graphene Devices

Figure 31(a) shows a scanning electron microscopy (SEM) image of a graphene beam (or bridge), the most explored device geometry by Dhingra. Figures 31(b) and (c) are graphene drums, clamped by poly(methyl methacrylate) (PMMA) and aluminum, respectively, and suspended over a trench.

The procedure of patterning and transferring graphene as synthesized into suspended mechanical devices is organized in an unpublished note [45] and is summarized in Fig. 32(b) and (c). The graphene is patterned by deep-UV lithography and oxygen plasma with PMMA as photoresist. The copper substrate on which the graphene is grown is etched away by ferric chloride or ammonium persulfate. The floating graphene/PMMA film is then picked up by the pre-defined grooved substrate for suspension. After removing PMMA with acetone and critical-point drying, the structure of suspended graphene devices is achieved.

6.2 OPTICAL TRAPPING SETUP

In line with other research efforts of using an optical trap for nanomechanics experiments, it was found in this lab that an absorptive particle, such as soot or dye can be burnt off a substrate and stay trapped in a simple focused laser beam at 405 nm and relatively low NA, about 0.5. Therefore, a strategy of mixing nanodiamonds with tartrazine, primary ingredient for food dye Yellow 5, was formed to load nanodiamonds in the optical trap. The reason for the particular choice of tartrazine is its strong absorption around 405 nm, and hence its orange color. The diamonds

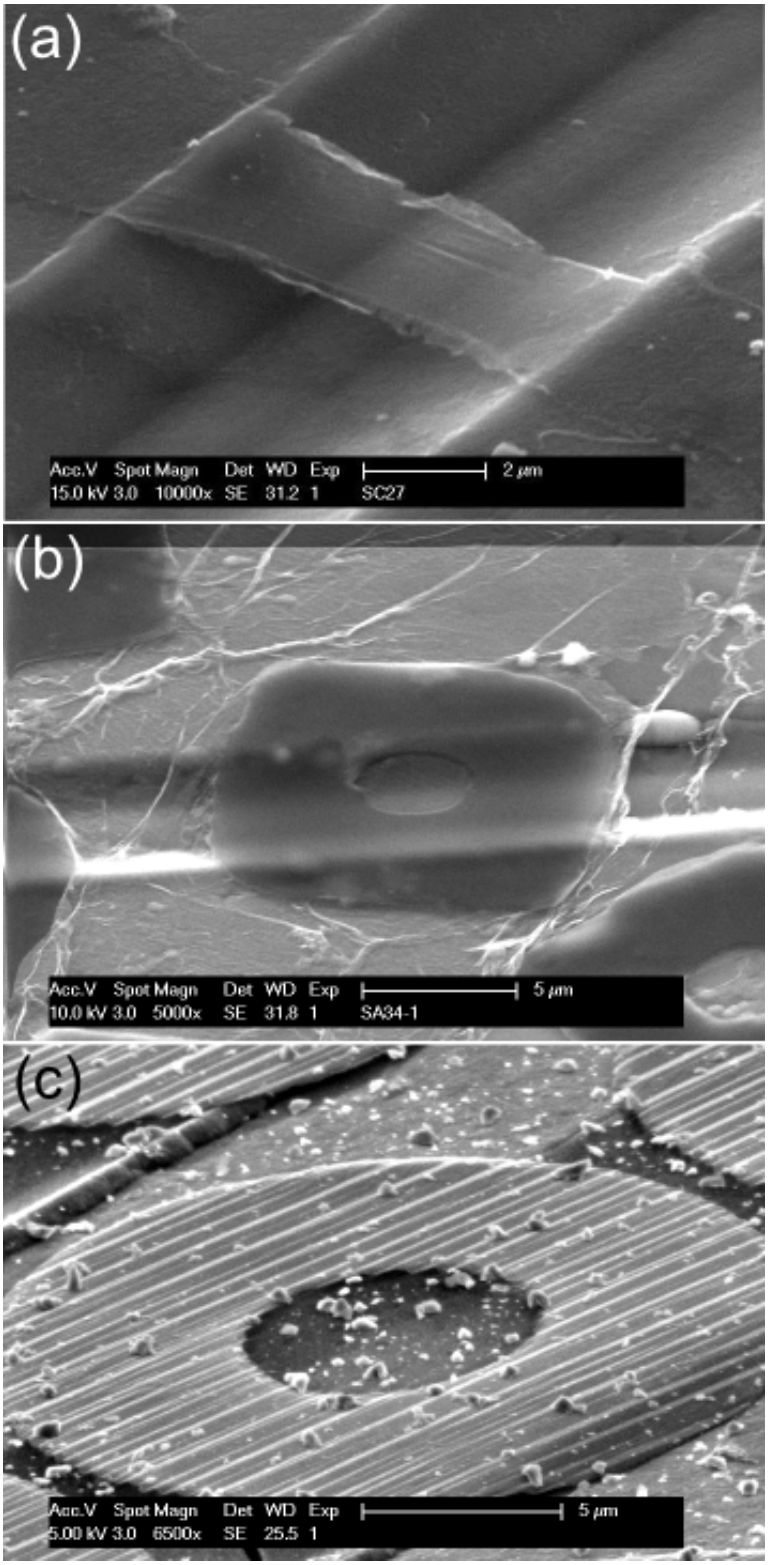

Figure 31: SEM images of suspended graphene devices fabricated in the lab, (a) beam (or bridge), (b) drum with PMMA clamping, and (c) drum with aluminum clamping.

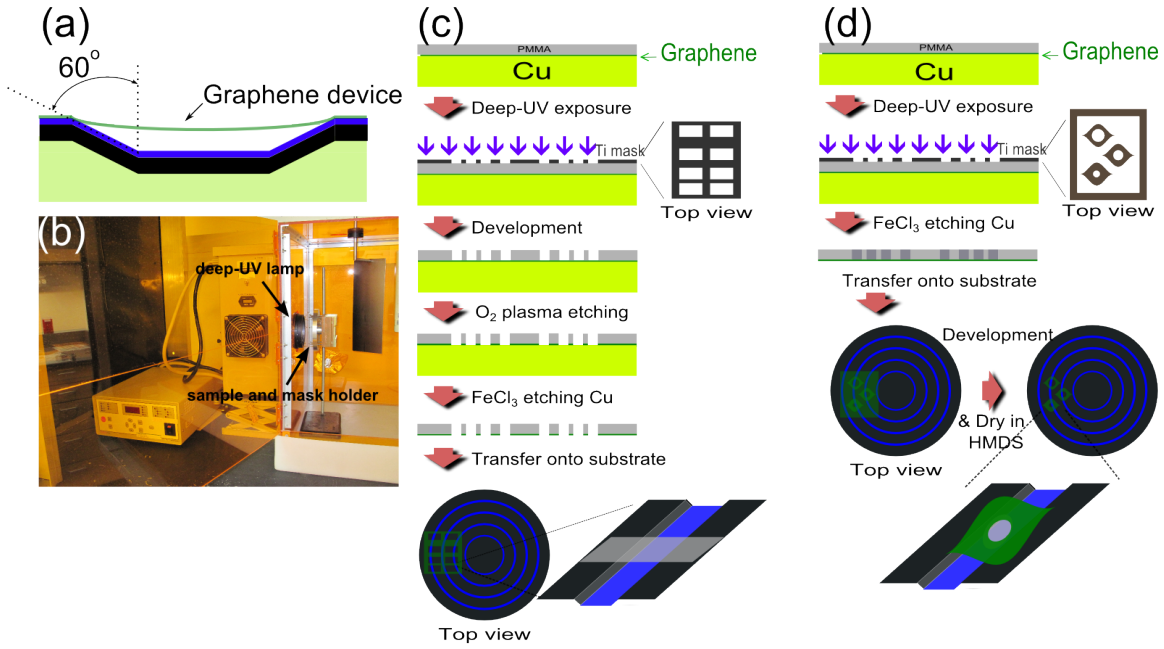

Figure 32: (a) Basic geometry of a suspended graphene beam device. (b) The deep-UV exposure setup in the lab. The orange cover is to block the UV. (c) and (d), fabrication steps for the beam and drum devices, respectively.

can indeed be "smuggled" into the optical trap, as was verified by the photoluminescence (PL) counts when an excitation laser at 520 nm was turned on. The control experiment was simply loading the tartrazine and checking its sensitivity to the excitation. This experiment is described in a previous publication [46].

However, with this loading approach, trapping in vacuum could not be achieved, as the particle would disappear in the process of evacuating the chamber, at a pressure usually as high as half an ambient pressure. The suspicions are: one, removing air is removing damping, and the particle had enough energy to escape the trap. Two, removing air reduces heat conduction, and the particle was burning off. Lastly, the trapping mechanism was not purely the optical gradient force. In fact, another mechanism, photophoretic force [65, 66] (or simply thermal force), might dominate. Since the photophoretic force relies on there being air molecules around, it will eventually weaken and disappear under vacuum, as the air molecules' mean free path increases. It is also consistent with the fact that only absorptive particles can be trapped in this way, indicating mechanisms other than gradient of the laser beam are dominant effects.

Figure 33(a) shows a small cluster of tartrazine-nanodiamond mix (T-ND) trapped in front of a reflecting objective (Newport 50102-02). Figure 33(b) is a spatial scan of the PL counts from the trapped particle. The spatial scan is performed by a home-built mirror galvo system with a pythics user interface [48].

Figure 34 shows the main results of [46]. In Fig. 34(a), PL counts with excitation on and off are recorded for 100 loadings each for T-ND and tartrazine only, and the counts are scatter-plotted. The distributions are prominently different: while the tartrazine data points are restricted to the $x = y$ line, indicating insensitivity to the excitation laser, the counts of T-ND when the excitation is on are typically several times that when the excitation is off. Note that log scales are used for both axes. Figure 34(b) reinforces this observation by counting the occurrence of ratios of PL counts when the excitation is on to off. While for tartrazine only the ratio is tightly centered around 1, T-ND has a very broad distribution up to ~ 10.

Though this approach was proven to efficiently load nanodiamonds into the trap, the inability to keep the particle under vacuum made it less attractive for high-Q mechanics experiments.

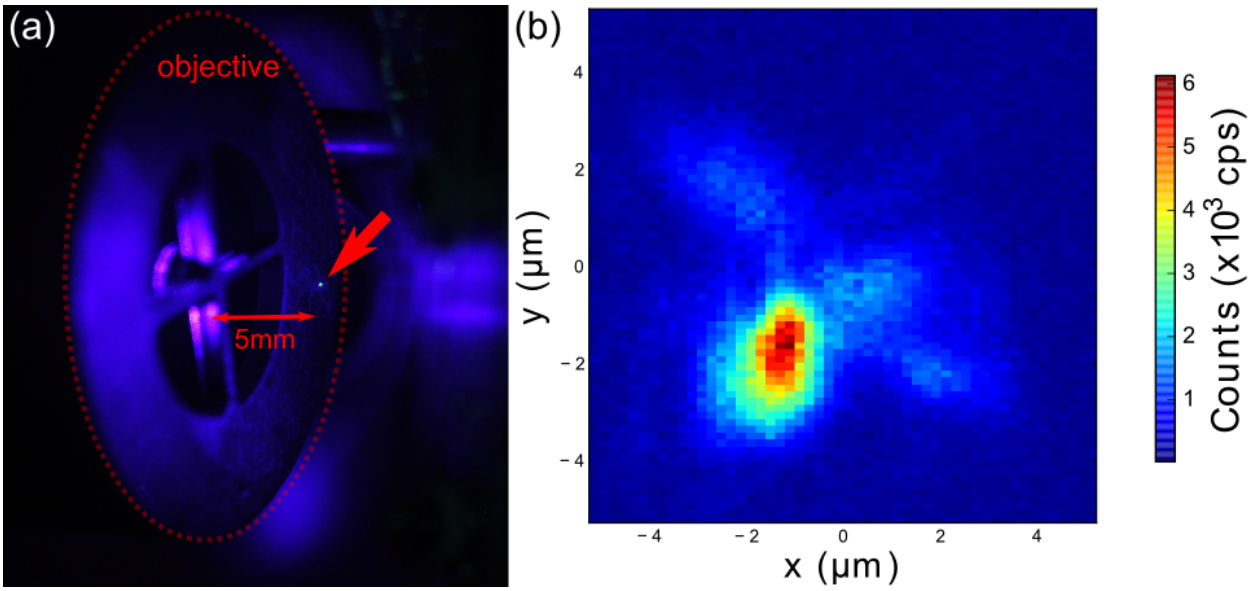

Figure 33: (a) A T-ND mix trapped by focused 405 nm laser. (b) Spatial scan of the photoluminescence of the trapped cluster.

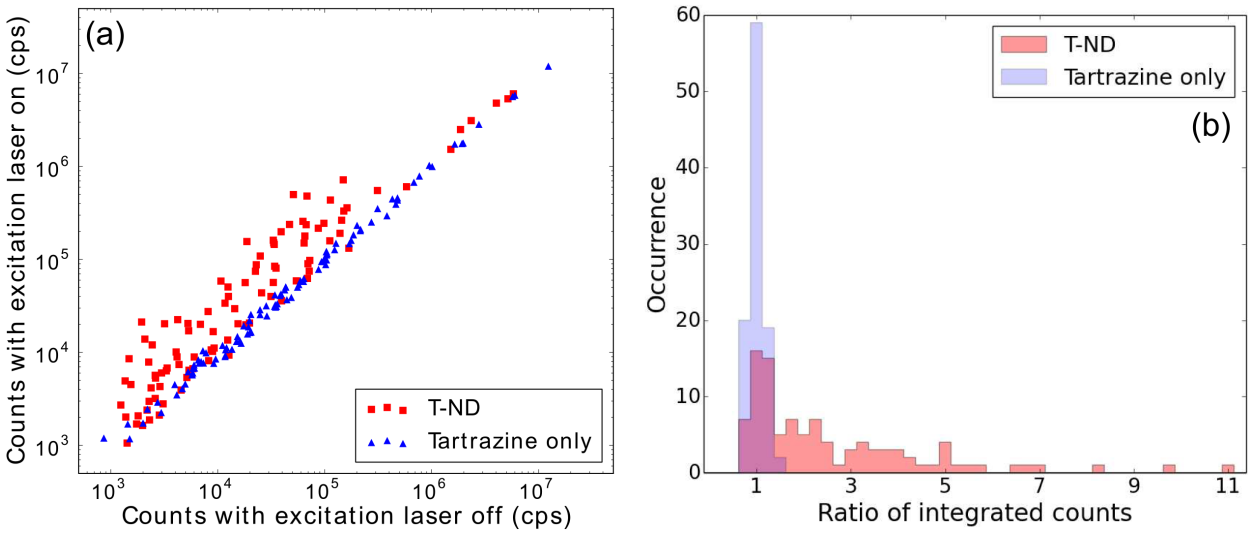

Figure 34: (a) Scattered plot of PL counts with the excitation laser on (y-axis) and off (x). T-ND mix is much more sensitive to the excitation laser. (b) Histogram of ratio of PL counts with excitation on to off. For tartrazine the ratio is tightly centered around 1.

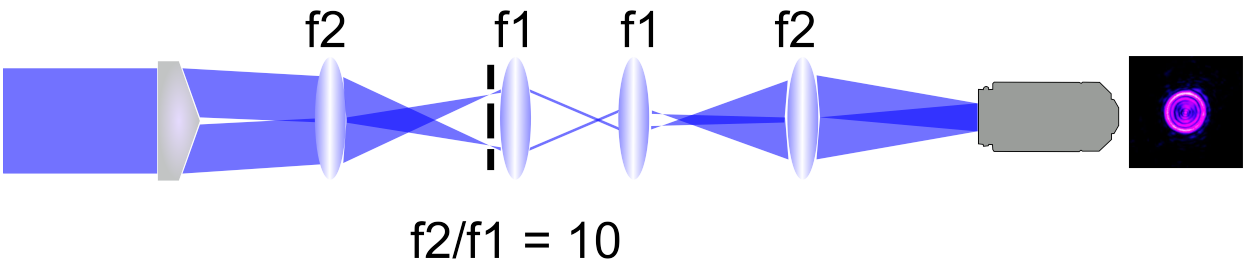

Figure 35: The optical setup of a axicon-based bottle beam trap. On the right-hand side is the image of the trap at the center.

6.3 BOTTLE TRAP WITH AXICON

Another optical-trap-related idea was to use a bottle beam, generated by an axicon, a conical lens [139]. Utilizing both the photophoretic force and scattering forces, the hope is that the particle can be confined in the bottled defined by the axicon.

Figure 35 shows the basic optics arrangement for the bottle beam. The axicon is produced by the single-point diamond turning machine in the lab. The axicon can be of reflective style (from aluminum) or refractive style (from acrylic glass, or PMMA). Since the final bottle size is small, the axicon angle is typically $\sim 0.5^{\circ}$ or smaller.

For loading particles into the trap, a ideal of selective (on-demand) loading of nanodiamond off a (laser burnt) suspended graphene film was also proposed. Illustrated in Fig. 36, this nanodiamond-graphene structure can be fabricated with simple transfer steps onto a TEM copper grid (e.g., 2000 mesh copper grids from SPI). The bottle beam is to be turned on after being aimed at a nanodiamond in a suspended-graphene region. However, this idea was not realized. Possibly due to graphene's strength, the diamonds might have been launched after the graphene film is burnt by the bottle beam, as opposed to staying in place and being trapped.

An alternative way of loading would be simply burning a dye-diamond mix a substrate. Though trapping was observed with this approach, the trapping lifetime was fairly short. In Fig. 37(a), the bottle was imaged from its side by scattering the laser beam off a thin wire placed vertically at a series of positions from the objective. In this figure, there is indeed a low-intensity volume. The

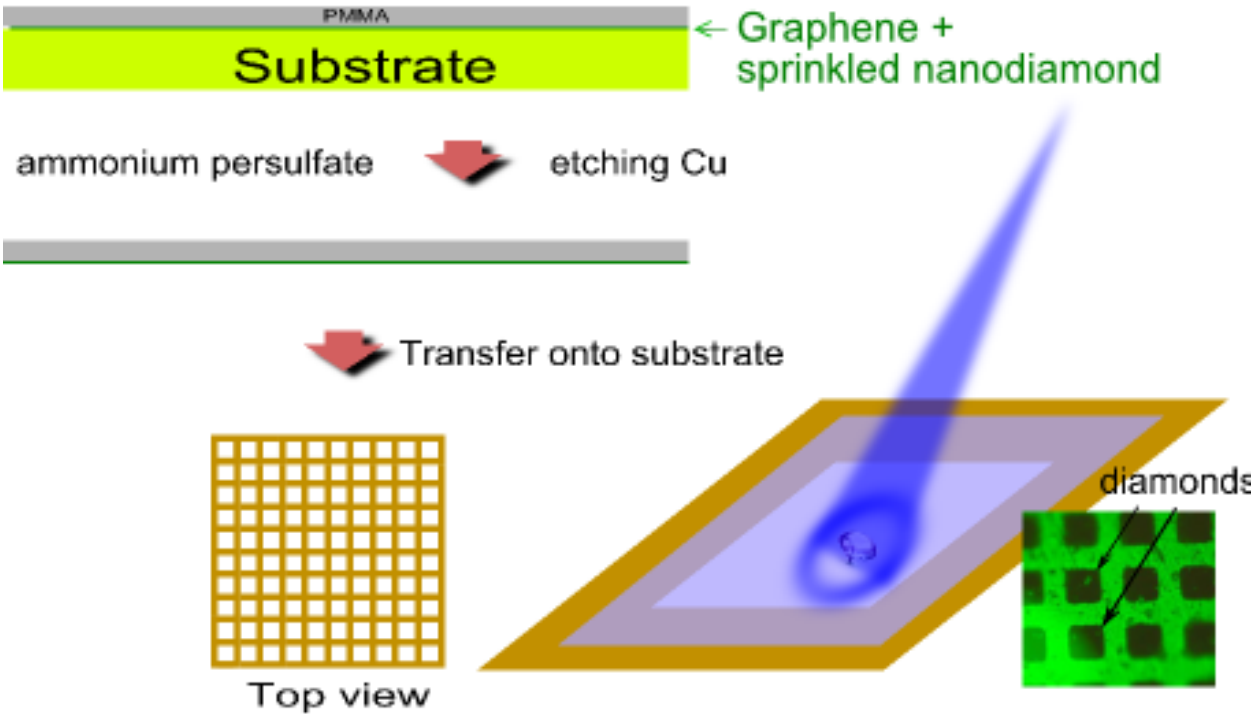

Figure 36: The fabrication steps for selective loading of nanodiamond off the suspended graphene film.

wire was then removed and images were taken when a particle is loaded. After several loadings, the images were stacked and are shown in Fig. 37(b).

Figure 37(c) then put (a) and (c) on top of each other. The results shows that despite the nice trap volume, particles do not favor staying in it, instead, they are probably in the little "cracks." This phenomena was not understood, and the desired experiment could not be done with this trapping performance. One speculations is that the particles did not have the right size, and therefore are easy to sneak into small openings.

6.4 THREE-PIECE MAGNETIC TRAPPING

The previous (first) generation of the magnetic trap had a open-top, three-piece geometry, as representatively shown in Fig. 38.

This design was adopted from the design for a femtodroplet experiment [40]. The reasons for the modifications are, first, to avoid machining the magnets themselves, as common neodymium-iron-boron magnets from powders chip very easily and the machining chips are extremely hard to remove from the piece. Second, on a related note, the optical numerical apertures for the original design are way too small for significant motion detection without machining the magnets.

As a consequence, using easier-to-machine magnetic pole pieces to shape the magnetic field became the primary strategy. Fig. 38(a) is a cross-section view of the initial trap geometry with primitively simulated magnetic field lines by Vizimag. The trapping relies on the rapidly changing magnetic field. The particles are "lifted up" by the field gradient going from the top pieces to the bottom one, but the particle would sit in the trap because of gravity. The top pieces are slanted for optical access from top. The axial confinement is achieved by slitting the bottom iron ridge (Fig. 38(c)) for a width that is comparable to other dimensions, i.e., ~ 100 μm.

Basic trapping, drying of droplets, and primitive cooling of the motion had been demonstrated for this geometry. The materials that have been trapped are bismuth, silicon carbide, diamond, and gloss beads, all of a few microns to a hundred microns. However, it was suspected that the slitting of the ridge can weaken the trapping in other directions. Significant rate of "leaking" and sinking down to the bottom were observed, either during the initial evacuation or drying. As

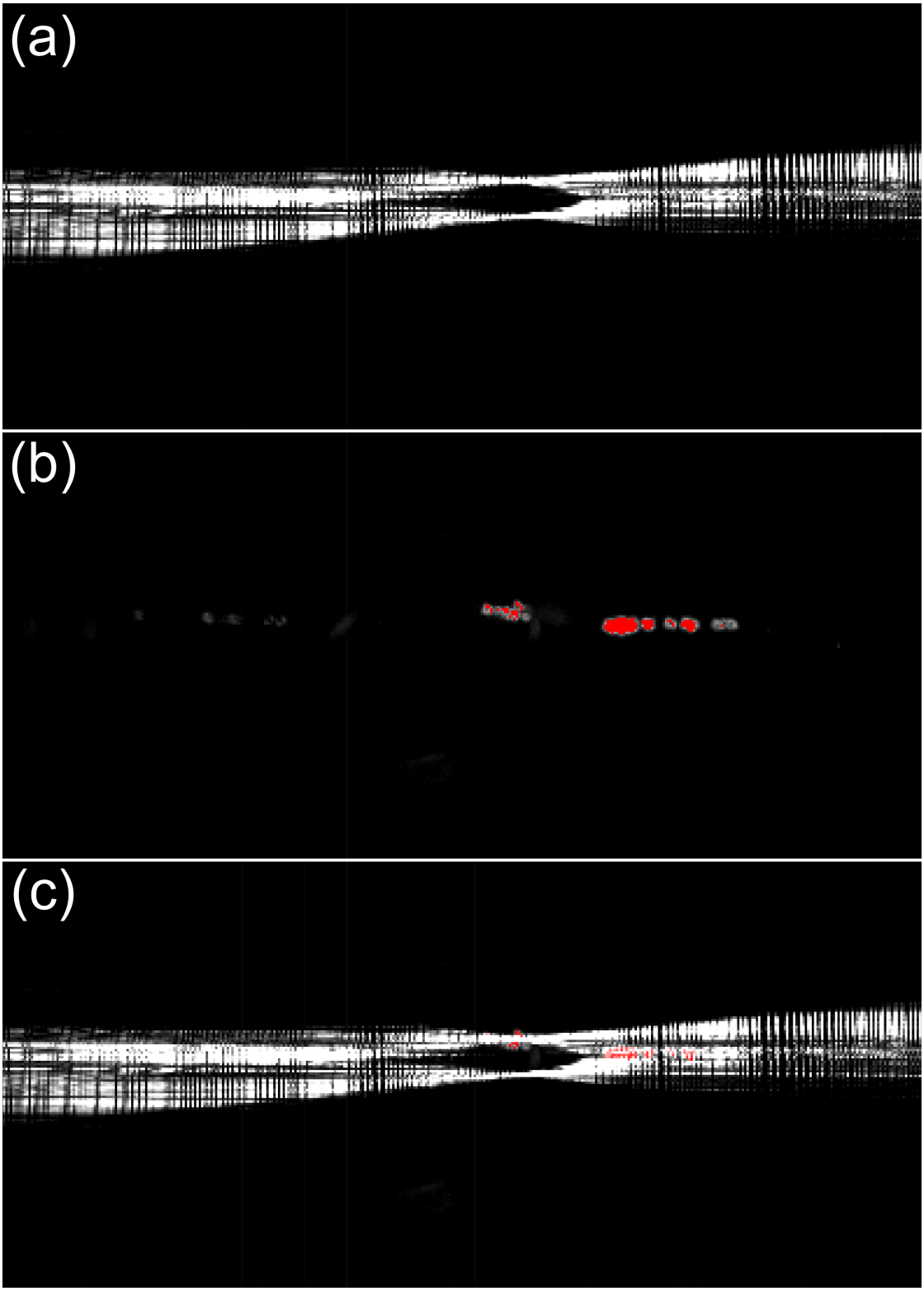

Figure 37: (a) Integrated profile images of a bottle beam. (b) Integrated images of particles loaded. (c) Superimposed image of (a) and (b).

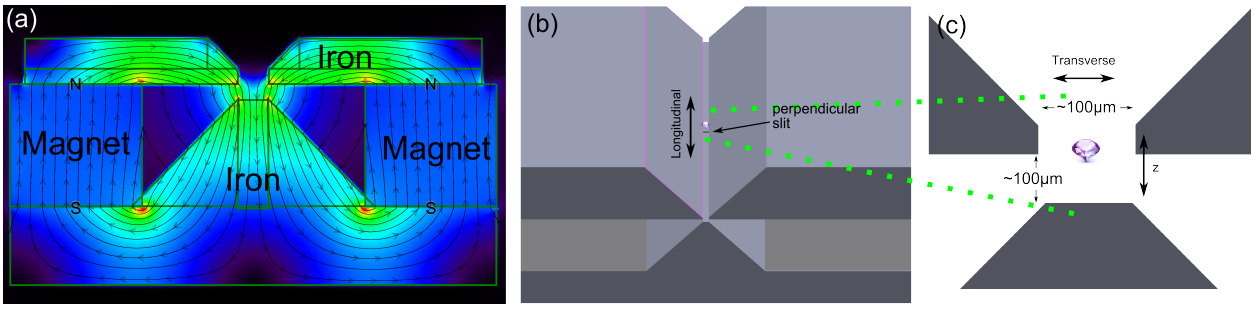

Figure 38: (a) Arrangement of the three-piece magneto-gravitational trap. (b) 3-D rendering of the trap from a tilted angle. (c) Basic dimensions of the trap.

a result, the design was steered towards a more symmetric one, i.e., a quadrupole-like trap, as detailed in Chapter 3.

7.0 CONCLUSION AND OUTLOOK

The experiments carried out of magnetic trapping of clusters of diamond nanocrystals, from the electromagnetic mechanics, trap design, detection, to quantum mechanics outlook have been described in detail. The cooling of the center-of-mass motion of the trapped particle is demonstrated to achieve 600 mK for nanodiamonds and 15 mK for silica microspheres.

However, it is not "there" yet, obviously. There is still a long way from $\sim 10^{-1}$ K to the ground state effective temperature, $\sim 10^{-9}$ K. Therefore, the following section examines this experiment system for what can be improved to get ready to touch down.

7.1 IDEAS OF IMPROVEMENTS

In short, there are four major roadblocks in the path towards a better cooling results: electric charge, particle size, detector noise, and vacuum.

7.1.1 Charge State Control

The residual charge might not only reduce the mechanical Q by generating eddy currents, but also force the particle out of the trap if the charge-to-mass ratio is high. The latter would be manifest when smaller particles are attempted. Therefore, this issue is tangled with the particle size one.

As has been explored in Sec. 3.6.3, UV lamps at different illumination positions can charge the trapped particle in either direction. It remains to constructed that two UV lamps can be arranged and turned on independently, so that the charge can be arbitrarily controlled.

Or, seeing the bulkiness of a UV lamp, other more compact ways of neutralization might be desirable.

7.1.2 Particle Size

The trade-off between the zero-point motion scale, cooling performance, and easiness of data analysis favors the particle size to be larger than 100 nm and less than 1 μm.

The 1-μm bar comes from imaging. A particle that is less than the spot size of the microscopy system will appear as a diffraction-limited spot in the image. This eliminates the noise from the internal structure being imaged, for which the detector confuses the internal "blinking" with the center-of-mass motion. Also, a single particle, rather than a cluster of smaller ones, is strongly favorable, since is helps suppress the noise, since there are many fewer faces for light scattering.

The first step towards it is to load droplets that contain only single particles, so that when they are dried up, only one particle remains trapped. This amounts to fine-tuning the concentration of the particles in DBS. This optimal concentration would of course cause more failure in loading and drying because statistically, there will be many droplets containing zero particles, and they will simply dry up and vanish.

As pointed out in the previous subsection, single sub-micron particles will be harder to keep trapped, as they are more prone to electric force on charge and thermal excitation. It is very likely that the cooling of the motion needs to be left on during the entire process, starting from a small and almost dry droplet with a particle.

7.1.3 Detector

The noise levels observed in the data presented in Chapter 4 may still be due to the particle motion. This means detector electronics is not limiting the noise yet. But the PSD presented in Chapter 4 alone will surely overwhelm the motion signal as it gets to lower effective temperatures. New detectors, for example, an low-temperature avalanche photodiode (APD) based custom detector, are in continued development.

7.1.4 Vacuum

Ideas of pushing to even higher vacuum include using a titanium sublimation pump, baking out the chamber, and upgrading to a cryogenic system.

Baking of the walls of the chamber primarily pulls water molecules off, and potentially can achieve 10^{-10} Torr vacuum. Most of the system is ready for baking out up to a temperature of about 150° C. The Curie temperature of the samarium-cobalt permanent magnets is much higher, and they are stably usable up to 250° C. The kapton film is characterized up to 200° C [140].

The only material that can fail at 150° C is the adhesives of the kapton tape that is securing the driving wire down to the trap pieces. Therefore, a better clamping mechanism for the wire is required.

A potentially better alternative is using a printed wire pattern of copper on kapton, such as DuPont Pyralux AC 352500EY or AC 091200EV, which is also an on-going project. The patterning can be done with standard lithography with photoresist (e.g., AZ1512) by the in-house lithography in the lab. This approach can be expanded to include more wires for voltage biasing or microwave drive for NV applications.

An ultimate pressure of less than 10^{-17} Torr(!) is possible if the experiment chamber is placed in a cryogenic temperature, < 10 K. It works, as opposed to baking the water out, by trapping the water molecules on the walls, so they do not contribute to the pressure anymore. Again, this is one of the big on-going projects in the lab.

7.2 G MEASUREMENT

The magnetic trapping is weak enough that gravity comes into play. There is possibility that the Newton's gravitational constant, G, can be measured. Maybe counter-intuitive, though the gravitational constant is already estimated by Newton, there are discrepancies in precision measured values of G [141] in recent decades, and it remains the least precisely-measured among the fundamental constants.

Since the motion of the trapped particle in the magneto-gravitational trap presented here is

affected by gravity, this system provides a path measurement of G. If a large mass is placed near the the magnetic trap, additional "spring" from gravity would modify the resonant frequencies from magnetic trapping, hence providing a calibration for G if the large mass is measured with enough precision.

APPENDIX A

Q-FACTOR DUE TO EDDY CURRENTS FROM MAGNETIC FIELD FLUCTUATIONS

Here the "back action" of the magnetized trap particle on the trapping substrate is analyzed. The Q-factor due to this change in magnetic field at the surface of the substrate is estimated.

A.1 GENERAL FORMALISM

Following the analysis on Jackson p. 198, the magnetic scalar potential for a dia/paramagnetic sphere in a uniform field in $\hat{z}$ is

$$\begin{cases} \Phi_M = -H_0 r\cos\theta + \dfrac{1}{3}M_0 r\cos\theta, \text{inside sphere,} \\ \Phi_M = -H_0 r\cos\theta + \dfrac{1}{3}M_0 a^3\dfrac{\cos\theta}{r^2}, \text{outside sphere.} \end{cases} \tag{A.1}$$

For outside of the sphere, the magnetic field can be calculated

$$\vec{H}_{\text{out}} = -\vec{\nabla}\Phi_M = \vec{H}_0 - \vec{\nabla}\left(\frac{1}{3}M_0 a^3\frac{\cos\theta}{r^2}\right). \tag{A.2}$$

We also know that

$$\vec{H}_0 = \frac{1}{\mu_0}\vec{B}_0 \tag{A.3}$$

for the external field. Hence we can calculate the "magnetic induction"

$$\vec{B}_{\text{out}} = \mu_0\vec{H}_0 - \mu_0\vec{\nabla}\left(\frac{1}{3}M_0a^3\frac{\cos\theta}{r^2}\right) \tag{A.4}$$

$$= \mu_0\vec{H}_0 - \mu_0\frac{M_0a^3}{3}\left[\hat{r}\frac{\partial}{\partial r}\left(\frac{\cos\theta}{r^2}\right) + \hat{\theta}\frac{1}{r}\frac{\partial}{\partial\theta}\frac{\cos\theta}{r^2}\right] \tag{A.5}$$

$$= \underbrace{\mu_0\vec{H}_0}_{\vec{B}_0} - \mu_0\frac{M_0a^3}{3}\left(\frac{2\cos\theta}{r^3}\hat{r} + \frac{\sin\theta}{r^3}\hat{\theta}\right) \tag{A.6}$$

Now $\Delta\vec{B} = \vec{B}_{\text{out}} - \vec{B}_0$ is the change of magnetic induction due to the magnetic sphere.

At a distance D from the particle, the maximal possible change in the magnetic induction is

$$\left|\Delta\vec{B}\right|_{\text{max}} = \mu_0\frac{M_0a^3}{3}\sqrt{\left(\frac{2\cos\theta}{D^3}\right)^2 + \left(\frac{\sin\theta}{D^3}\right)^2}\,|_{\text{max}} \tag{A.7}$$

$$\approx \frac{1}{3}\mu_0M_0a^3\sqrt{\left(\frac{2}{D^3}\right)^2 + \left(\frac{1}{D^3}\right)^2} \tag{A.8}$$

$$= \mu_0\frac{\sqrt{5}}{3}\frac{M_0a^3}{D^3} \tag{A.9}$$

Now M_0 is estimated. For dia- or paramagnetic material, by Eq. (5.115),

$$\vec{M}_0 = \frac{3}{\mu_0}\left(\frac{\mu-\mu_0}{\mu+2\mu_0}\right)\vec{B}_0. \tag{A.10}$$

A.2 NUMERICAL VALUES

In our system, diamond spheres are 100 nm to 1 μm in diameter and the spheres are ∼100 μm from the substrate. For paramagnetic materials,

$$\mu = \mu_0(1+\chi_\nu), \tag{A.11}$$

where χ_ν is the magnetic susceptibility and μ is the magnetic permeability. For diamagnetic materials, χ_ν is usually a very small negative number. Even though diamond is among the "stronger" diamagnetic material, $\chi_\nu = -2.1\times10^{-5}$. Hence

$$M_0 \approx \frac{2\times10^{-5}}{\mu_0}B_0 \tag{A.12}$$

Therefore,

$$\left|\Delta\vec{B}\right|_{\text{max}} = \mu_0 \frac{\sqrt{5}}{3}\left(\frac{a}{D}\right)^3 \frac{2\times 10^{-5}}{\mu_0} B_0 \tag{A.13}$$

$$\sim \left(\frac{a}{D}\right)^3 B_0 \times 10^{-5} \tag{A.14}$$

Quality factor Q can be estimated as how large the external induction is in multiple of $\left|\Delta\vec{B}\right|_{\text{max}}$,

$$Q \sim \frac{B_0}{\left|\Delta\vec{B}\right|_{\text{max}}} \sim \left(\frac{a}{D}\right)^3 \times 10^{-5}. \tag{A.15}$$

Physically the factor of 10^{-5} comes from the smallness of diamagnetic susceptibility, and the rest is determined by the ratio of the dimensions.

sphere radius a	distance D (μm)	Q
1 μm	100	10^{11}
100 nm	100	10^{14}
1 μm	200	10^{12}
100 nm	200	10^{15}

The above calculation assumes that all the field change happens at the very surface, and the field does not penetrate into the material at all. But in reality there is some finite skin depth.

If the conductivity and magnetic hysteresis of the material can be cut down, the system can have a higher Q (lower loss). But in a realistic material, one can not find lower values in both.

APPENDIX B

MAGNETIC POTENTIAL ENERGY OF A DIAMAGNETIC OBJECT

The following analysis starts from Sec. 5.16 of [85]. Expressed in terms of the fields, the total magnetic energy is

$$W_1 = \frac{1}{2}\int \vec{B}\cdot\vec{H}d^3x, \tag{B.1}$$

where the integration is carried out in all space and for linear materials. The relationships

$$\vec{B} = \mu\vec{H}, \vec{B_0} = \mu_0\vec{H} \tag{B.2}$$

can be employed to calculate the energy increase:

$$W = W_1 - W_0 = \frac{1}{2}\int \left(\vec{B}\cdot\vec{H} - \vec{B_0}\cdot\vec{H}\right) d^3x \tag{B.3}$$

$$= \frac{1}{2}\int \left(\vec{B}\cdot\vec{H_0} - \vec{H}\cdot\vec{B_0}\right) d^3x \underbrace{+\frac{1}{2}\int \left(\vec{B}+\vec{B_0}\right)\cdot\left(\vec{H}-\vec{H_0}\right) d^3x}_{W_B}. \tag{B.4}$$

Since

$$\vec{B} + \vec{B_0} = \vec{\nabla}\times\vec{J}, \tag{B.5}$$

the second term in Eq. (B.4) becomes

$$\frac{1}{2}\int \left(\vec{B}+\vec{B_0}\right)\cdot\left(\vec{H}-\vec{H_0}\right) d^3x = \frac{1}{2}\int \left(\vec{\nabla}\times\vec{J}\right)\cdot\left(\vec{H}-\vec{H_0}\right) d^3x. \tag{B.6}$$

Using the vector identity

$$\vec{\nabla}\cdot\left(\vec{a}\times\vec{b}\right)=\vec{b}\cdot\left(\vec{\nabla}\times\vec{a}\right)-\vec{a}\cdot\left(\vec{\nabla}\times\vec{b}\right), \tag{B.7}$$

W_B can be further rewritten as ($\vec{J}$ as $\vec{a}$ and $\left(\vec{H}-\vec{H}_0\right)$ as $\vec{b}$)

$$W_B=\frac{1}{2}\int\left\{\vec{\nabla}\cdot\left[\vec{J}\times\left(\vec{H}-\vec{H}_0\right)\right]+\left[\vec{J}\cdot\vec{\nabla}\times\left(\vec{H}-\vec{H}_0\right)\right]\right\}d^3x \tag{B.8}$$

$$=\frac{1}{2}\int\vec{J}\times\left(\vec{H}-\vec{H}_0\right)\cdot\hat{n}da+\frac{1}{2}\int\vec{J}\cdot\left[\vec{\nabla}\times\left(\vec{H}-\vec{H}_0\right)\right]d^3x. \tag{B.9}$$

The first term in Eq. (B.9) is derived by Gauss' law, and the area integral is performed at the boundary, which is at infinity. Hence, this term is zero. The second term in Eq. (B.9) is zero as well since $\left(\vec{H}-\vec{H}_0\right)=0$, and therefore, $W_B=0$ and

$$W=\frac{1}{2}\int\left(\vec{B}\cdot\vec{H}_0-\vec{H}\cdot\vec{B}_0\right)d^3x \tag{B.10}$$

$$=\frac{1}{2}\int_V\left(\vec{B}\cdot\vec{H}_0-\vec{H}\cdot\vec{B}_0\right)d^3x+\frac{1}{2}\int_{\text{outside }V}\left(\vec{B}\cdot\vec{H}_0-\vec{H}\cdot\vec{B}_0\right)d^3x, \tag{B.11}$$

where V is the volume of the diamagnetic object and hence the first term represents the integral within the object volume and the second term all outside free space. However, in free space $\vec{B}=\mu\vec{H}=\mu_0\vec{H}$, the second term in Eq. (B.10) is zero:

$$\int_{\text{outside }V}\left(\vec{B}\cdot\vec{H}_0-\vec{H}\cdot\vec{B}_0\right)d^3x \tag{B.12}$$

$$=\int_{\text{outside }V}\left(\mu_0\vec{H}\cdot\vec{H}_0-\vec{H}\cdot\mu_0\vec{H}_0\right)d^3x \tag{B.13}$$

$$=0. \tag{B.14}$$

Exploiting the relationships Eq. (B.2),

$$W=\frac{1}{2}\int_V\left(\vec{B}\cdot\vec{H}_0-\vec{H}\cdot\vec{B}_0\right)d^3x \tag{B.15}$$

$$=\frac{1}{2}\int_V\left(\vec{B}\cdot\frac{1}{\mu_0}\vec{B}_0-\frac{1}{\mu}\vec{B}\cdot\vec{B}_0\right)d^3x \tag{B.16}$$

$$=\frac{1}{2}\int_V\left(\frac{1}{\mu_0}-\frac{1}{\mu}\right)\vec{B}\cdot\vec{B}_0d^3x. \tag{B.17}$$

Since diamagnetism is a small effect, the field distortion is ignored, i.e., $\vec{B} \approx \vec{B}_0$. Further assuming that the volume V is small and the field is uniform within,

$$W \approx \frac{1}{2} V B_0^2 \left(\frac{1}{\mu_0} - \frac{1}{\mu} \right) \tag{B.18}$$

$$= \frac{1}{2} V B_0^2 \frac{1}{\mu_0} \left(1 - \frac{\mu_0}{\mu} \right). \tag{B.19}$$

The magnetic susceptibility is defined as

$$\chi = \frac{\mu}{\mu_0} - 1, \text{ or } \frac{\mu_0}{\mu} = \frac{1}{1+\chi}. \tag{B.20}$$

Thus,

$$W = \frac{1}{2} V B_0^2 \frac{1}{\mu_0} \left(1 - \frac{1}{1+\chi} \right) \tag{B.21}$$

$$\approx \frac{1}{2} V B_0^2 \frac{1}{\mu_0} \left[1 - (1-\chi) \right] \tag{B.22}$$

$$= \frac{\chi B_0^2 V}{2\mu_0}. \tag{B.23}$$

Here $\vec{B}_0$ stands for the undistorted field, which is the same as in the main text. But this is the work done for both creating the magnetic moment and introducing to the external field. For simply the potential energy,

$$W = -\frac{\chi B_0^2 V}{2\mu_0}. \tag{B.24}$$

See p.214 in [85].

APPENDIX C

LAPPING OF MAGNETIC TRAP POLE PIECES

The appendix documents the step-by-step procedure for lapping the magnetic trap pole pieces by hand.

Materials needed:

1. Pole pieces to be lapped, pre-machined as described in Sec. 3.4.
2. Emery cloth of 800 grade or finer, 1 sheet.
3. Water

Equipment needed:

1. Steel pole piece holder for lapping.
2. Microscope for inspection.

Procedure:

1. Tuck the pole piece in the slot in the holder.
2. Adjust the height of the pole piece with the back setscrew, until the tip is about flush with the holder surface.
3. Tighten the side setscrew to hold the pole piece in place. Double check the height of the tip.
4. Turn the back setscrew in slightly, say 1/16 of a turn or even less. Now the tip should stick out of the surface.
5. Wet the emery cloth with water.

6. Lift the emery cloth up in the air by one hand at an edge. Hold the lapping holder on the other hand and make the lapping surface touch the emery cloth. Do not place the surface against the table top at this point. The capillary force of water between the lapping surface and the emery cloth squeezes water out and keeps the two surfaces sealed in contact.
7. In a figure 8 pattern, move the holder around for initial lapping, while still keeping the holder and cloth in air from touching the table by hand. This prevents the piece from the initial squeezing that can deform and destroy the tip.
8. Do the lapping on the cloth against the table for more figure 8s, but still lift the holder to prevent excessive pressure.
9. Eventually, the holder can rest against the table, while the hands only push the holder horizontally to lap.
10. Inspect the tip and determine whether the desired width has been reached. If yes, the procedure is done. If not, repeat from Step 4.

APPENDIX D

DISTILLATION OF DBS AND PREPARATION OF PARTICLE-DBS-SOLVENT SLURRY

This appendix details the procedure to purify dibutyl sebacate (DBS) by distillation. This includes the glassware, vacuum and heating system setup, and operation sequence.

Also, calculation sheet for silica sphere concentration in DBS is provided.

D.1 DBS DISTILLATION

Procedure:

1. Disable the furnace door interlock, as the the furnace will need to be turned on while door is opened.
2. Use a long-handle brush to scrub clean the interior of the retort and collector as much as possible with alconox solution.
3. Ultrasonic clean the above two parts with acetone in them, and then repeat with isopropanol.
4. Rinse the parts with isopropanol and air blow dry.
5. Fill the retort with about 50 ml of DBS to be distilled, from the injection point (Fig. 16).
6. Apply a thin layer of vacuum grease (e.g., Dow Corning High Vacuum Grease) around the male glass joints of the retort, the plug for the injection, and the barb of the vacuum port on the collector.

7. Connect the glass joints.
8. Set the retort in the furnace and arrange the ceramic insulation caps and stuff the openings.
9. Connect the vacuum line. See Fig. 39.
10. Turn on the heat exchanger, so that any DBS vapor getting thourgh the line will condensate and be trapped in the low temperature copper tubings.
11. Turn on the dry pump, slowly open the valve and wait for the gauge to get to down to below 1 Torr. It will typically settle at around 0.5 Torr.
12. Turn on the furnace, and set the temperature to 170 or 180° C, a streak of DBS will appear towards the collector after about half an hour. At 180° C the process takes several hours. At 170° C, it is supposed to be gentler (not clear if cleaner) and will take a couple days.
13. Turn off the furnace when some 40 ml of DBS (80%) has been collected.
14. Close the vacuum valve.
15. Turn off the heat exchange.
16. Use a long-handle brush to scrub clean the interior of the retort as much as possible with alconox solution.
17. Ultrasonic clean the retort with acetone in it, and then repeat with isopropanol.
18. Rinse the retort with isopropanol and air blow dry.
19. Transfer the collected DBS to the retort through the injection point.
20. Clean the collector as described above.
21. Repeat from Step 6, for a typical of two times. Always stop distillation while some liquid (20%) is left behind in the retort.
22. Store the distilled DBS in a ultrasonically cleaned vial.

D.2 PREPARATION OF PARTICLE-DBS-SOLVENT SLURRY

The goal is to prepare a diluted DBS solution, so that it is reasonably easy to nebulize with low piezo driving voltages (≈ 30 V). And more importantly, each DBS droplet in the trap (~ 20 μm diameter) is best to contain just one diamond crystal or silica bead. Therefore, it comes down to two ratios: solvent to DBS and DBS to original slurry volume.

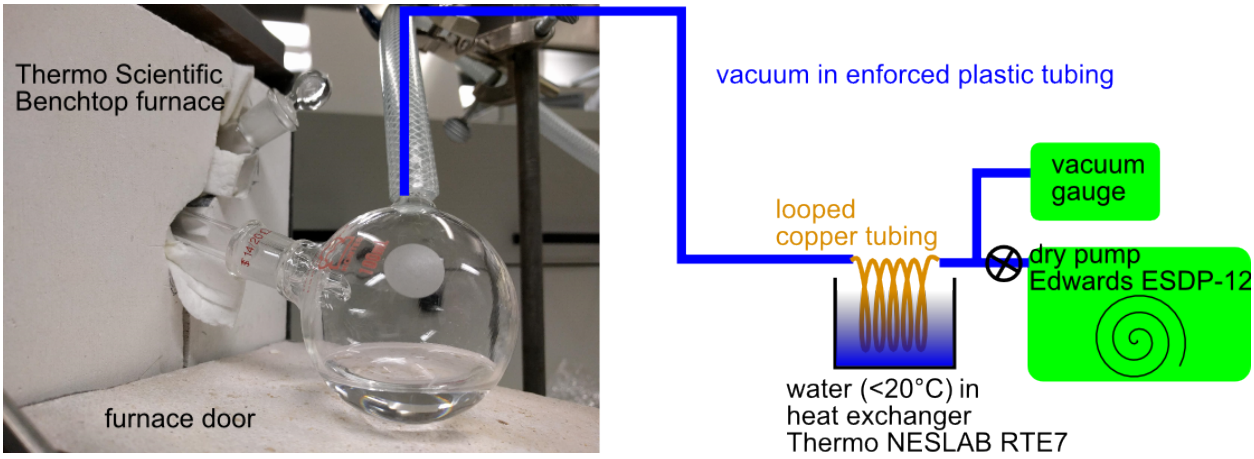

Figure 39: Complete setup of the DBS distillation system.

Depending on what solvent the original slurry is in, the same is used to dilute. As an experience, 10 times dilution is enough for nebulizing, and there is a reasonably amount of DBS droplets as well. The exact prescriptions for two commonly used slurries in the lab are summarized. The vial to contain the new mix should be ultrosonic cleaned in acetone and isopropanol. And after mixing, it is left in the ultrasonicator for at least 15 mins.

D.2.1 NanoComposix 400 nm Silica Spheres in Ethanol

Original particle density is 10.5 mg/mL, and the particle concentration is specified: 1.3×10^{11} particles/mL. Therefore, for a 20 μm diameter original slurry, there are 544 spheres. This implies that this can be diluted about 1000 times so there is $\lesssim 1$ particles in each droplet.

Preparation: 10 mL 200proof ethanol + 1 mL distilled DBS + 1 μL original slurry.

D.2.2 ThermoFisher 1 μm Silica Sphere

Original particle concentration is specified at 1.92×10^{10} particles/mL. Hence, a 20 μm droplet contains 80 spheres, and can be diluted 100 times to be $\lesssim 1$ particles in each droplet.

Preparation: 1 mL 200proof ethanol + 100 μL distilled DBS + 1 μL original slurry.

APPENDIX E

ELECTRONICS SETUP DETAIL

This appendix documents all the directly-related electronic circuits, including the design schematic, interface codes, and pictures of the circuit board actually made.

Dictionary for supplier abbreviation:

- DK: Digi-Key
- MM: McMaster-Carr

Note: All the power pins on integrated-circuit chips have bypass capacitors of 0.1 μF, unless otherwise noted. These play a role of large charge reservoirs, providing large current and avoiding voltage drops. The pins of the bypass capacitors are to be as close to the power pins as possible, to minimize inductance from long leads. The capacitors should be ceramic ones, with temperature coefficients of C0G or NP0 when possible, or X7R. Also, the voltage regulators used, such as L7815 and L7915, have specific requirement for output stabilization capacitor on respective datasheets. The recommended tantalum capacitors at values indicated there are used, but not explicitly drawn in the following diagrams.

E.1 ATOMIZER HORN AND DRIVING CIRCUIT

Figure 40 shows the detailed circuit diagram for the atomizer driver.

The Arduino sends out switching signals, sweeping from 150 to 200 kHz, in order not to miss

the resonant frequency of the horn. The MOSFET driver is capable of supplying enough current speedily to switch the gate of the MOSFET. The movement in the piezo element X1 is caused by the fast switching in the MOSFET gate, making the voltage difference across the piezo to oscillate near the Arduino switching frequency, hence driving the horn.

The current drawn and oscillating in the MOSFET-piezo loop will be as large as V/R, where V is the power supply S1 voltage and R is the equivalent resistance in the resistor array R12-R15. The voltage setting should then be according to the power dissipation rating of the power resistor, the current ratings for the MOSFET and the piezo element.

The input capacitance C_{iss} of MOSFET IRFP S40N50L is 8.1 nF, while the capacitance C_{piezo} of the piezo is 105 nF. Therefore, the time constant is dominated by the piezo. In order to generate droplets as large as tens of microns, the desired operation frequency shall be $\lesssim$ 500 kHz, compared with a few microns at few MHz for a commercial nebulizer. A resistance of 15 Ω is chosen such that the cut-off frequency $f_c = \frac{1}{2\pi RC} \approx 1/(2\pi \times 15\ \Omega \times C_{\text{piezo}}) \approx 100$ kHz, or $\tau \approx \Omega \times C_{\text{piezo}} \approx 1.6$ µs. The reason for the array of 15 Ω resistors, with the equivalent resistance of 15 Ω, is simply to distribute the power dissipation to multiple components.

A resistor is commonly placed before the gate of the MOSFET (R16 in FIG) to intentionally slow down the gating signal to avoid oscillation. In this case, this time constant $R16 \times C_{\text{iss}}$ shall not be longer than τ. Thus, a resistance value for R16 that's less than around 133 Ω is adequate, as $133\ \Omega \times 8.1$ nF≈ 1.1 µs. Here R16 is as small as 13 Ω, when the circuit seems to work without additional problems.

For this thesis work for loading DBS in IPA dilution, typically 30 V in S1 is adequate to generate droplets. This voltage is consider safe and the current (~ 2 A) is such short on-time (< 1 s) does not overheat the elements.

Below is the list for relevant files:

- mister_noliac_NAC2121_flange.dft, nozzle engineering drawing.
- insulation_film_and_peek_center_rod.dft, insulation film and center rod for electrical insulation between two sides of the piezo actuator.
- piezo_driver.ino, arduino DUE code for the switching signal.

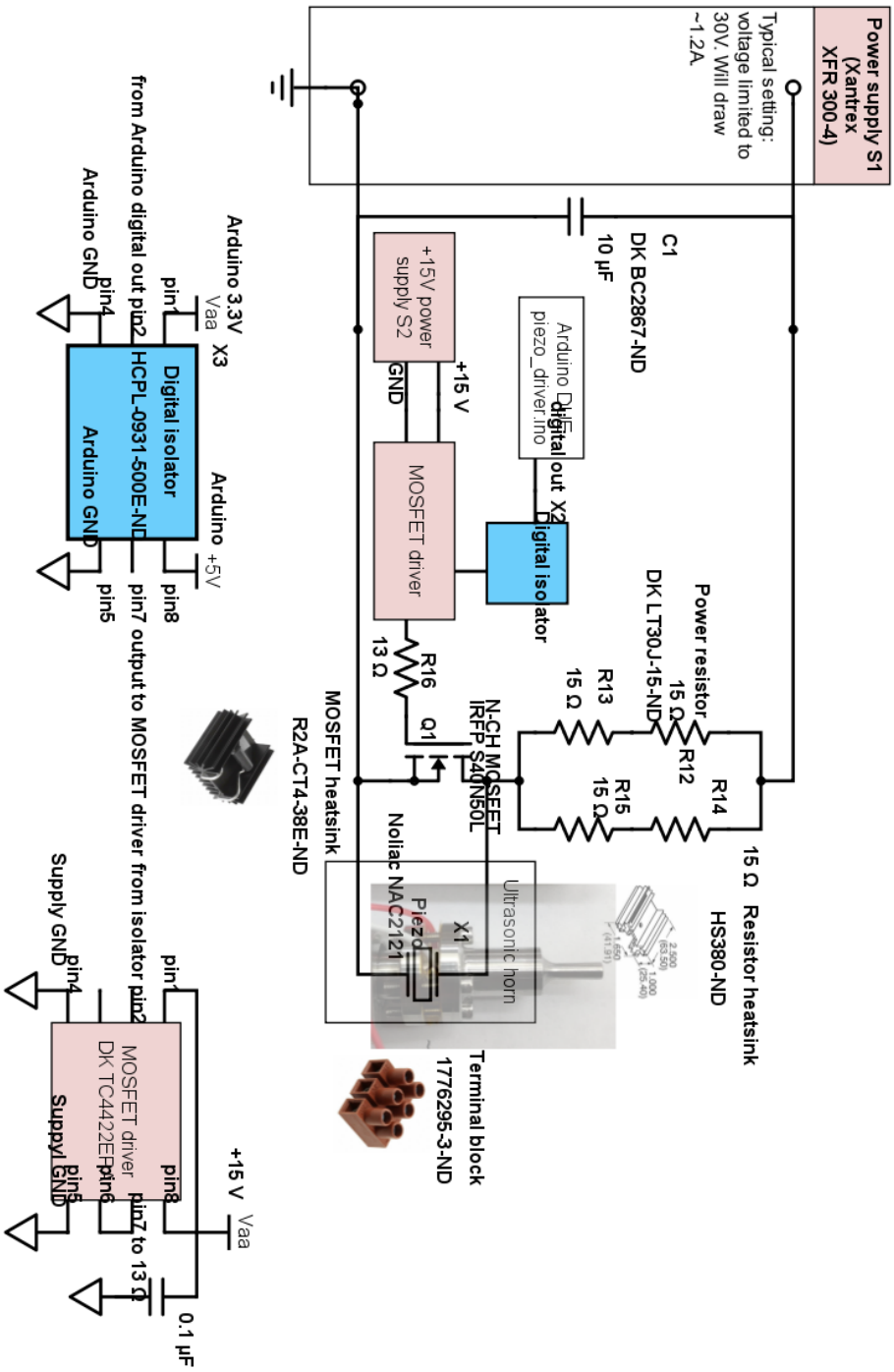

Figure 40: Circuit diagram for the atomizer driver. Note: All the power pins on integrated-circuit chips have bypass capacitors of 0.1 µF, unless otherwise noted. The pins of the bypass capacitors are to be as close to the power pins as possible, to minimize inductance from long leads. The capacitors should be ceramic ones, with temperature coefficients of C0G or NP0 when possible, or X7R.

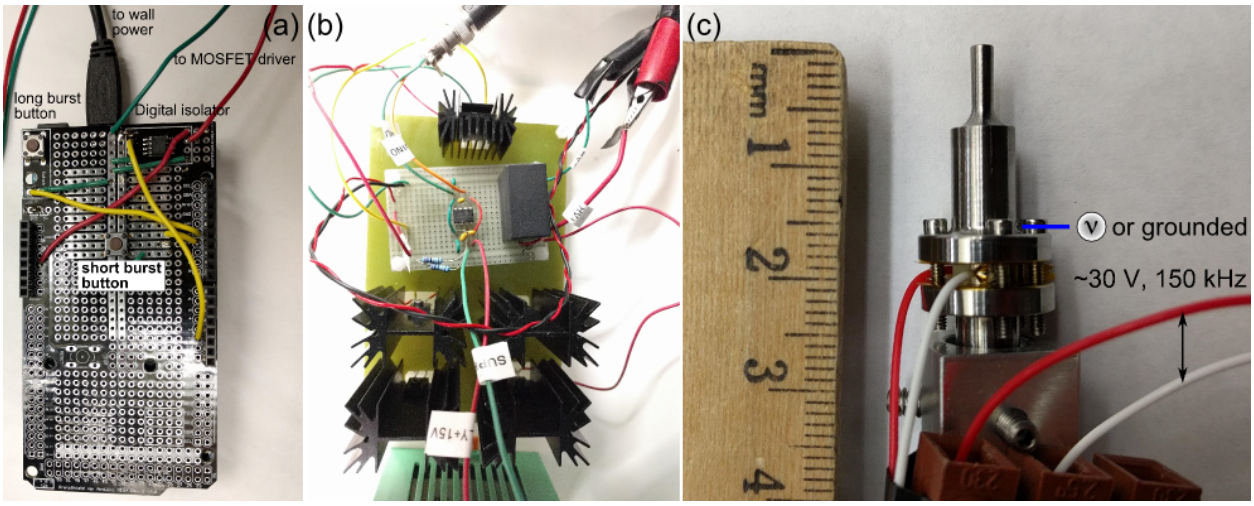

Figure 41: Electronics components of the atomizer setup.

E.2 NEWPORT 700C LASER MOUNT CONNECTION

In the lab, Thorlabs LDC202C or LDC205C are used for current supply and control of laser diodes. In this dissertation work, Newport 700C-9-5.6 laser diode housings are used exclusively. This model defines the optics height at 4 inches off the table surface, has built-in collimation lens holder with fine adjustment, has built-in thermoelectric controller and sensing thermistor, provides convenient $x-y$ adjustment, has a BNC connector and a nitrogen purge port, and slides side-to-side for alignment.

Some modifications need to be done to this laser mount to be compatible with Thorlabs controllers. Figure 42 is a record of the modified wiring specifically for cathode grounded configuration (CG), and the necessary steps are summarized below:

1. The db-9 male diode drive connector is replaced with a female version (SD9S, L-com), to receive the default cable with the Thorlabs controller.
2. According to the Thorlabs controller's manual (e.g., LDC205C [142]), jump connect Pin 1 and Pin 5 to disable the interlock.
3. Connect Pin 3 to the ground pin of the BNC connector, and then connect to the cathode of

the laser diode on the socket.

4. Connect Pin 8 to the center pin of the BNC connector, and then connect to the anode of the laser diode on the socket.

E.3 NEWPORT 700C LENS MOUNT ADAPTER

Newport 700C-9-5.6's fine collimator mount by default hosts Newport 700-42 near-IR lens. If another lens is desired, an adapter is needed to slide into the mount. Relevant file:

- newport_mnt_aspheric_holder_for_355230-B.dft, adapter's engineering drawing. The opening is specifically for the diameter of Thorlabs 355230-B lens.

E.4 NEWPORT 700C SMALL TO ADAPTER

As its name hints, 700C-9-5.6 can fit common diode base diameters of 9 and 5.6 mm. In this work, the Osram PL520 diode that is used to pump the NV at 520 nm has a base diameter of only 3.8 mm. Therefore, a special mount plate is needed to provide enough support for diodes of this style. Relevant file:

- 3dot8mm_diode_adaptor_to_Newport_700C_mount.dft, adapter's engineering drawing. In this drawing, the back holder basically extends the base of the diode, and the front cover replaces the one from the original package.

E.5 THERMOELECTRIC COOLER CIRCUIT

Figures 43 and 44 show schematic and the photography, respectively, of the control circuit for the thermoelectric cooler, e.g., the one in a Newport 700C-9-5.6. This module can serve up to two thermoelectric coolers. So, this dissertation work only needs one module. The output

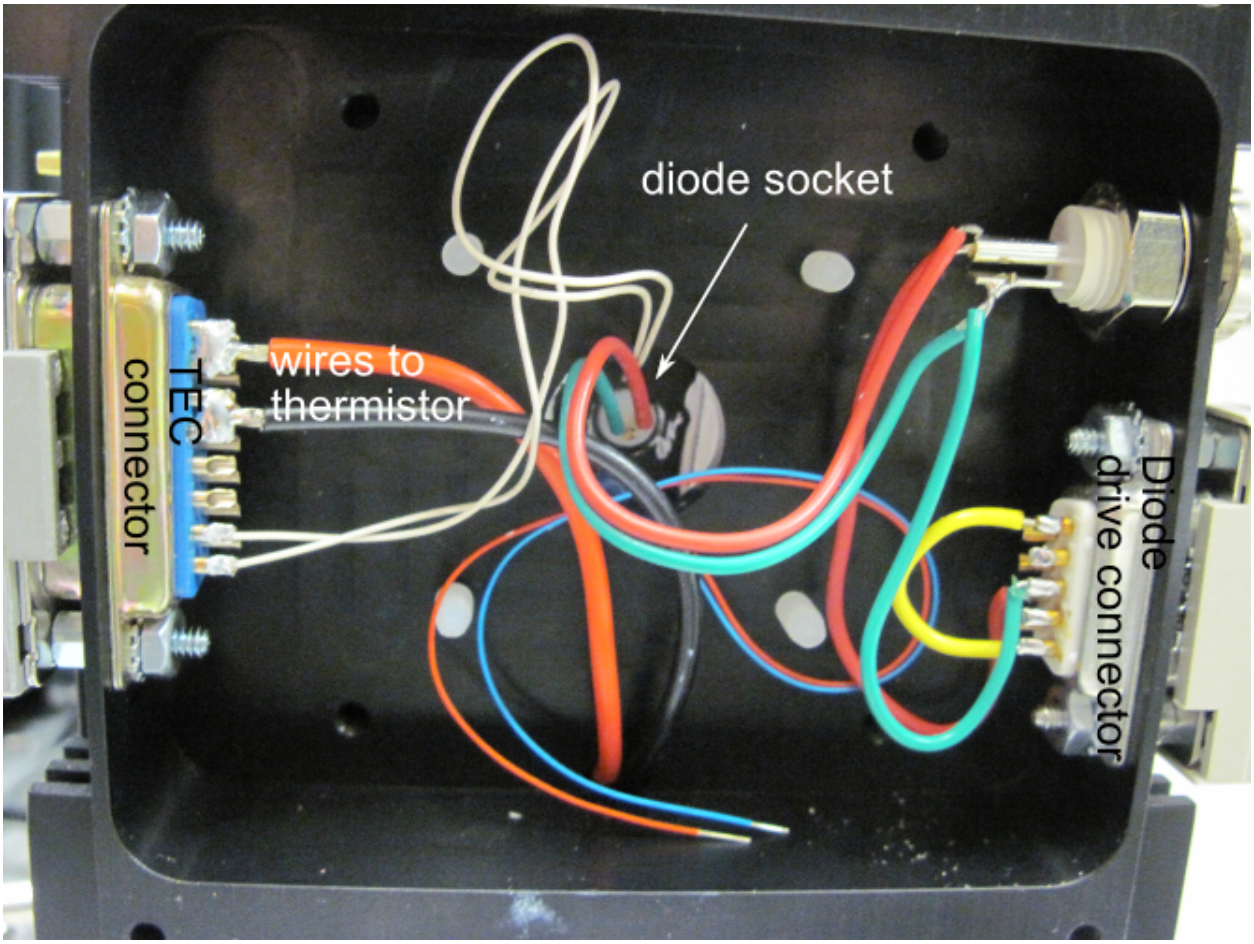

Figure 42: Modified wiring of Newport 700C-9-5.6 laser diode mount.

of this circuit is determined by the algorithm run by the Arduino. The algorithm is a PI loop, consisting of the leading order responding to the difference between set and actual temperatures and a correction term for the error.

Relevant files:

- arduino_TEC.ino contains the core PI loop algorithm.
- TEC_control_PID_interface.py and TEC_control_PID_interface.html are the python codes and the user interface for the Arduino algorithm.
- circuit_diagram_Arduino-TEC-w-Opto-isolator-OPA548.pdf, the circuit diagram.

E.6 PSD AMPLIFIER

Figure 45 is the complete circuit diagram for the PSD amplifying circuit.

First of all, this circuit is powered by the shared external ± 18 V power supply, regulated to ± 15 V. Additional $+10$ V regulator is to provide the biasing of the quadrant photodiode.

An transimpedance of 10 MΩ is the first stage conversion and amplification of the current signal. In the left-hand column of Fig. 45, current signals from the quadrant diode are converted to voltage signals, but remain separated in respective quadrants.

The center column converts voltages from each quadrant back to current by resistors, adds up currents from pairs of quadrants, and then outputs voltage signals T, B, L, and R with another gain of 10.

The top and bottom parts of the right-hand column further take the opposite pairs and calculate the the differences $T - B$ and $L - R$, and output with one more gain of 10. The sum, implemented by the middle of the right-hand column, simply takes the sum of currents from all quadrants, and outputs voltage with a gain of 10 or 100, depending on which 0-ohm jumper is installed (but not both).

Relevant files:

- LF_PSD_PCB_R1.sch and LF_PSD_PCB_R1.brd, the circuit schematics and board image.

Figure 43: Circuit diagram of the thermoelectric cooler control circuit. Note: All the power pins on integrated-circuit chips have bypass capacitors of 0.1 μF, unless otherwise noted. The pins of the bypass capacitors are to be as close to the power pins as possible, to minimize inductance from long leads. The capacitors should be ceramic ones, with temperature coefficients of C0G or NP0 when possible, or X7R.

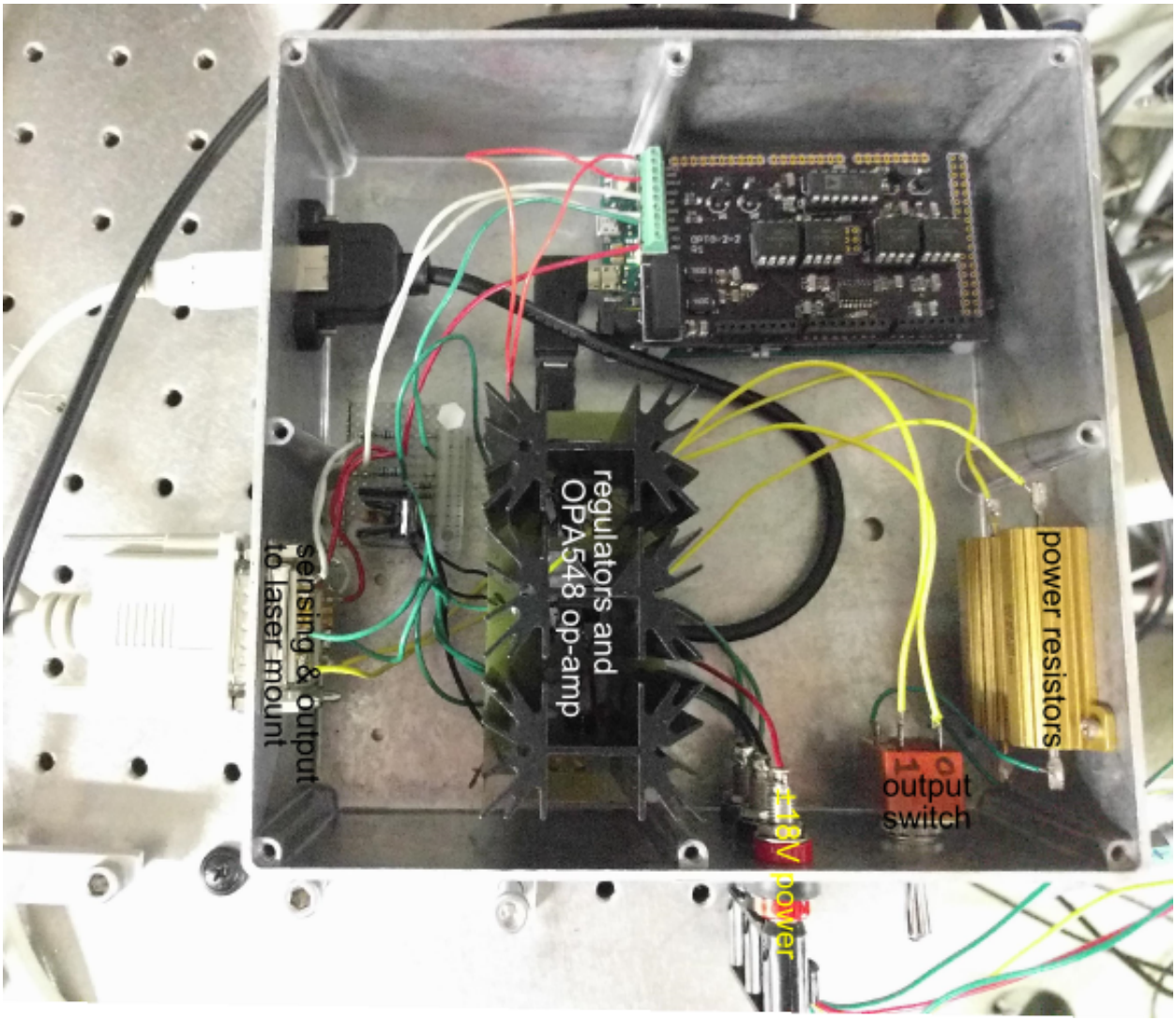

Figure 44: Photography of the assembled thermoelectric cooler control circuit.

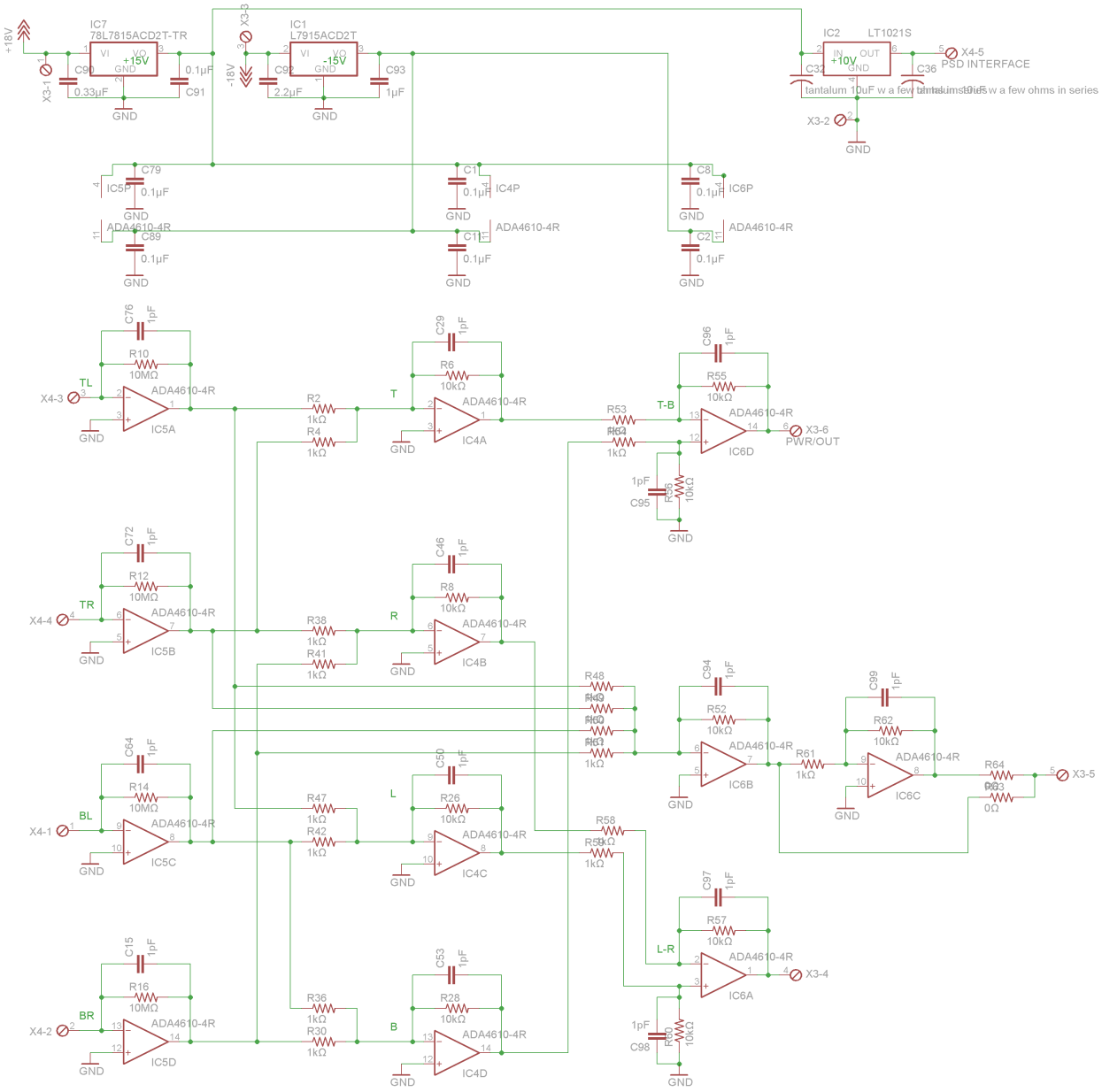

Figure 45: Circuit schematic of the PSD amplification.

- LF_PSD_PCB_parts.ods, complete parts list for building.

E.7 PASSIVE LOW-PASS ($RC \sim 1$ S), ACTIVE HIGH-PASS ($RC \sim 1$ S) FILTERS, AND PROGRAMMABLE-GAIN AMPLIFIER

Figures 46 and 47 show schematics of the passive low-pass, and the active high-pass and the programmable-gain amplifier, respectively. Figures 48 and 49 are photographs of the actual circuits built.

The passive low-pass filter passes any "slow" motions that are slower than the lowest resonant frequency, $\ll$ 10 Hz, and hence a time constant of 1 s is chosen. These slowly varying signals represent off-centering of the particle/droplet image on the PSD, and should be minimized by moving the chamber stage or the mirror tilting on the flip mount. In practice, the image is centered to the objective lens' center of field, as can be told by minimizing the coma error. Then, the tiltings of the mirror on the flip mount right before the focusing lens of the PSD are adjusted until the DC-coupled signals are minimized on the digital multimeters, e.g., Keithley 2000.

The high-pass filter picks up the oscillating motions, leaving any DC offset behind. In order not to lose signal strength, an active filter is used. The AC-coupled signals are sent to the programmable-gain amplifiers. The programmable-gain amplifier chip PGA204 from Texas Instruments can choose gains among 1, 10, 100, and 1000, depending upon the TTL status at two pins, defined by a accompanying Arduino DUE board. This Arduino DUE board is shielded by a digital isolator.

Relevant files:

- PGA204_interface_pythics_v0dot7dotx.py and PGA204_interface_pythics_v0dot7dotx.xml are the python script and the user interface for selecting the gain.

E.8 SALLEN-KEY 4TH-ORDER BUTTERWORTH FILTERS, 1 KHZ

Figure 50 shows the schematic for a Sallen-Key 4th-order implementation of a Butterworth filter with a 3-dB point at 1 kHz.

The simulated performance (by Analog Devices Filter Wizard) are plotted in Fig. 51. As can

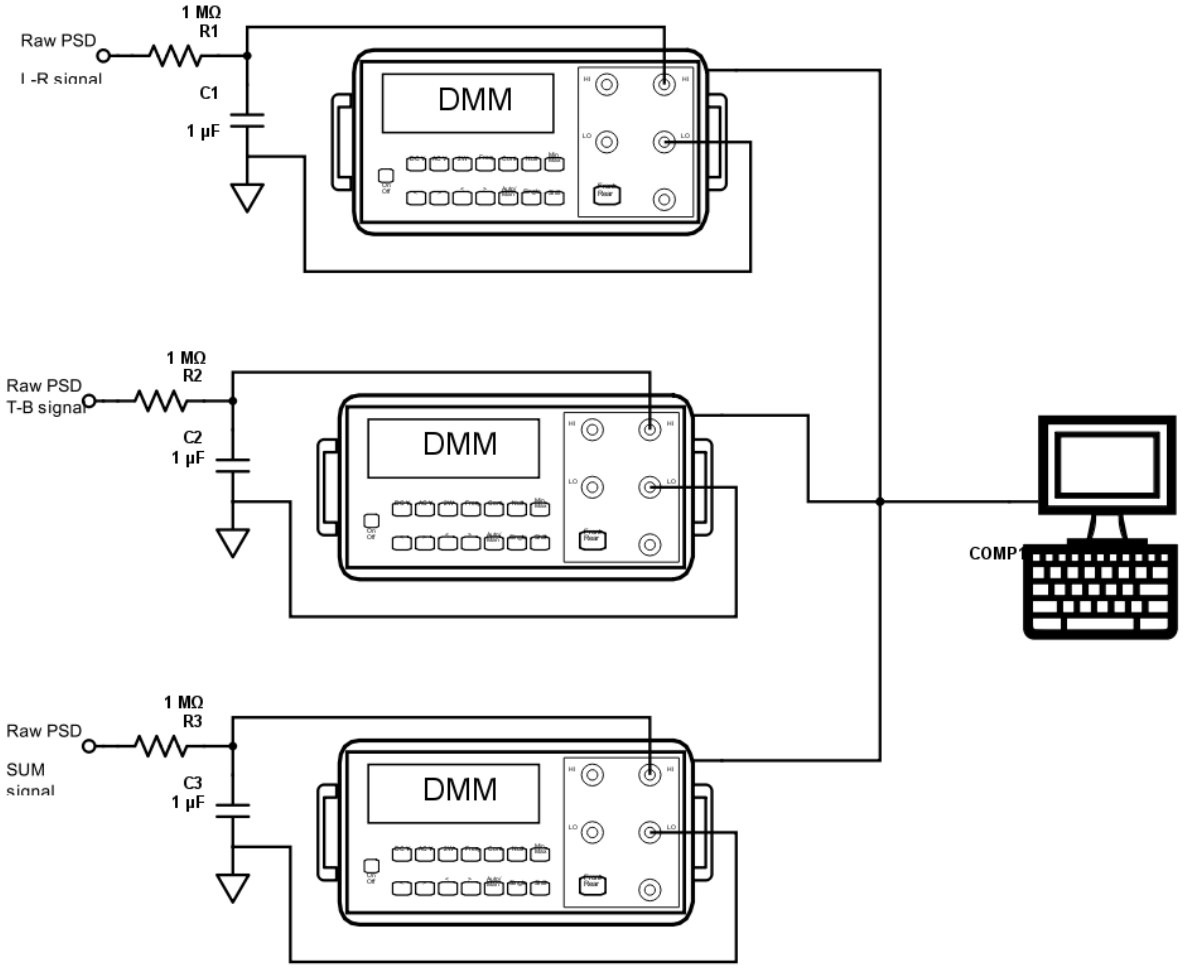

Figure 46: Circuit schematic of passive low-pass filter.

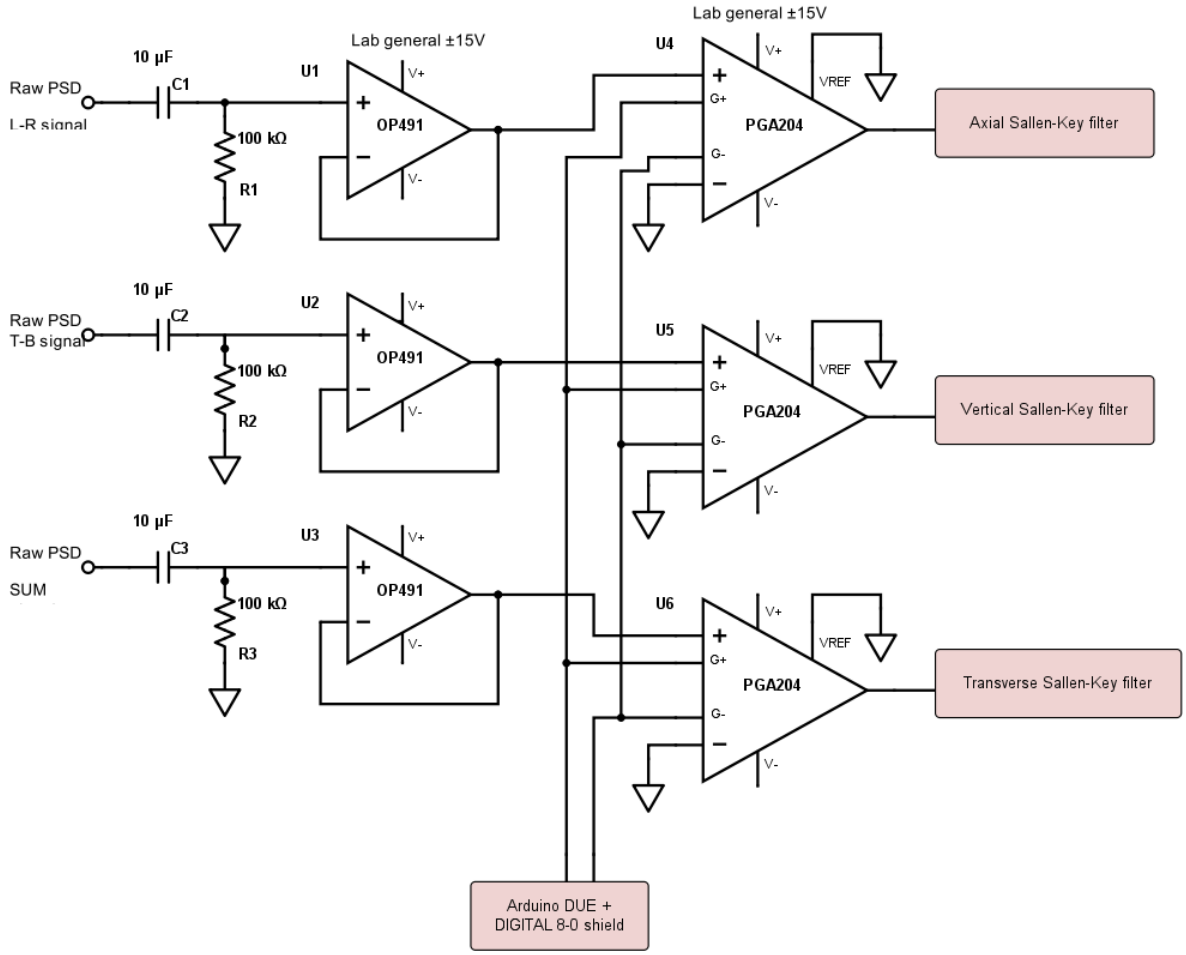

Figure 47: Circuit schematic of the active high-pass filter and the programmable-gain amplifier. Follower op-amp: OP491GPZ, programmable amplifier: DK PGA204BP-ND. Note: All the power pins on integrated-circuit chips have bypass capacitors of 0.1 µF, unless otherwise noted. The pins of the bypass capacitors are to be as close to the power pins as possible, to minimize inductance from long leads. The capacitors should be ceramic ones, with temperature coefficients of C0G or NP0 when possible, or X7R.

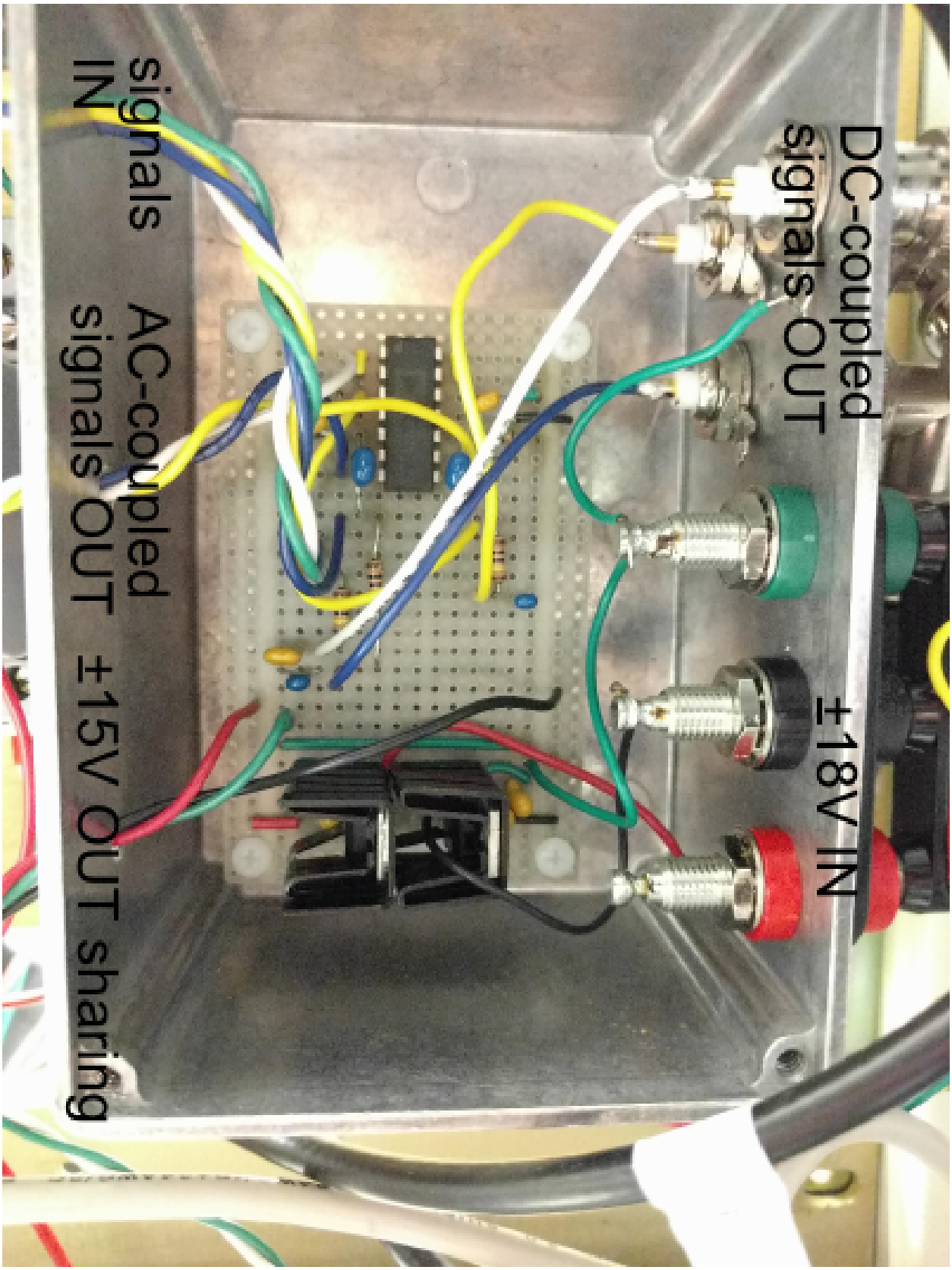

Figure 48: Photography of the low- and high-pass filters circuit.

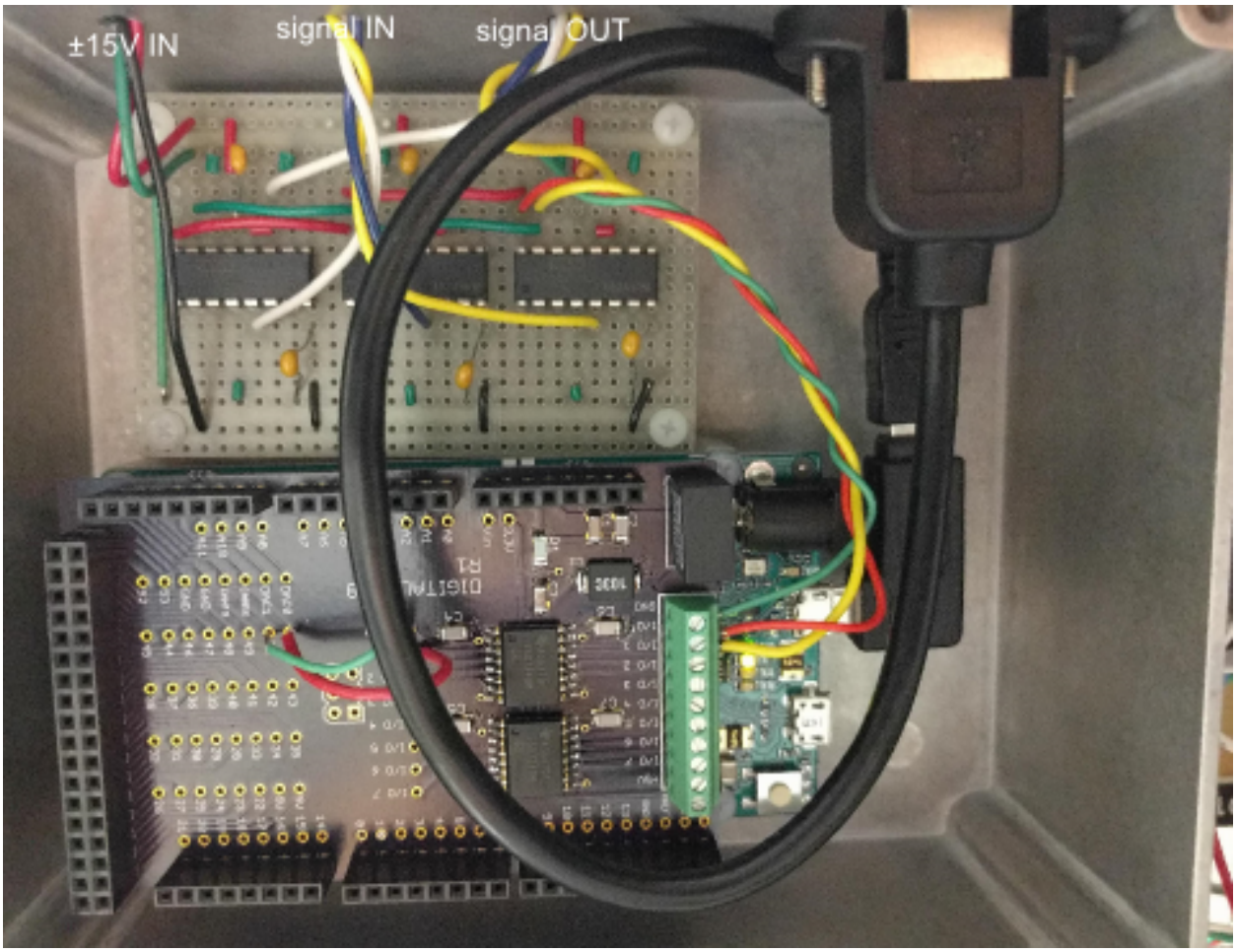

Figure 49: Photography of the programmable-gain amplifier.

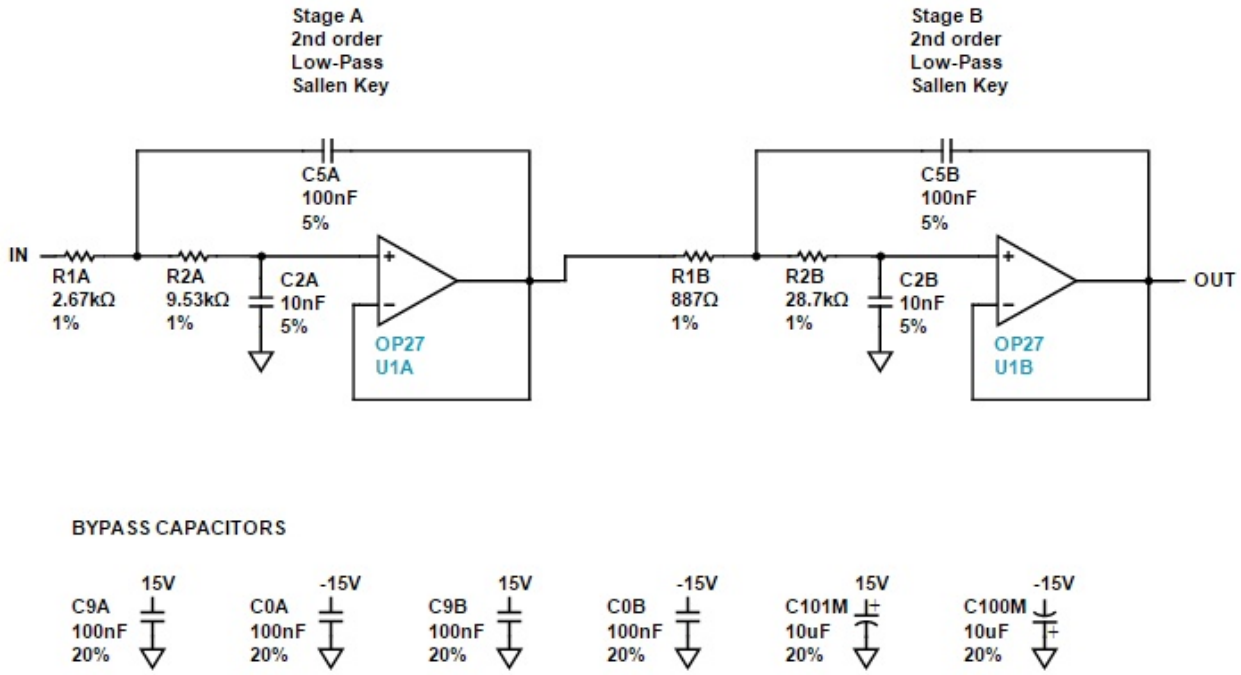

Figure 50: Schematic of the 1 kHz Sallen-Key filter. Op-amp: DK OP27EPZ-ND.

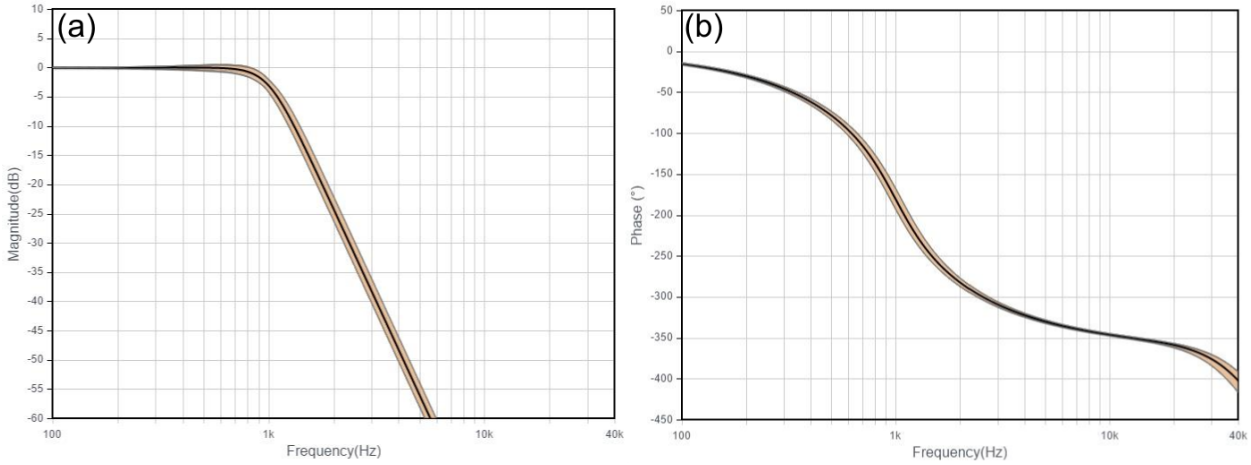

Figure 51: (a) Amplitude and (b) phase attenuation of the Sallen-Key filter as a function of frequency.

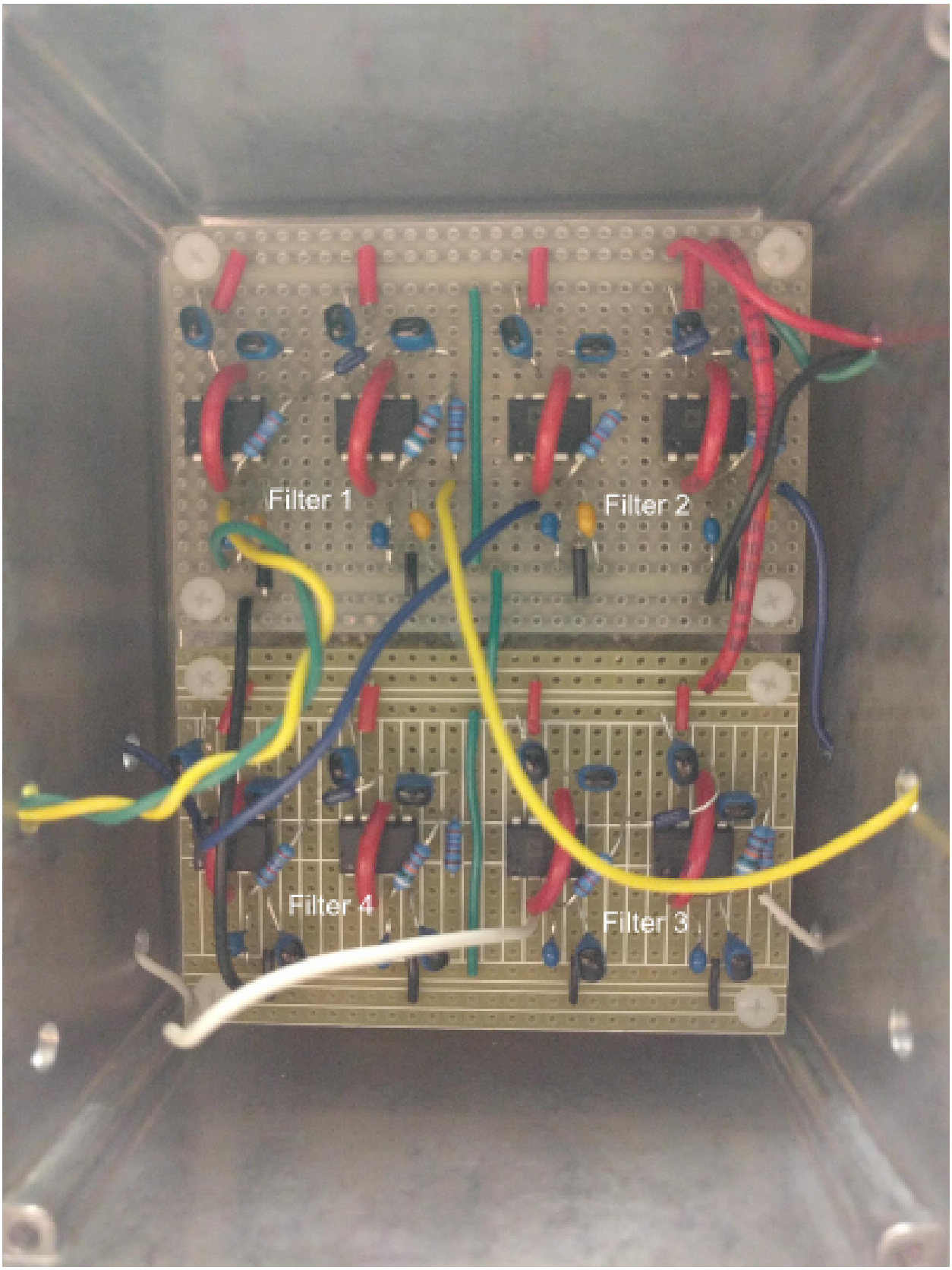

Figure 52: Photography of the built Sallen-Key filter.

be seen, at 2 kHz, the amplitude is already suppressed down to -25 dB, or 0.003 times the DC strength. The inconvenience this filter introduces, as can be seen in Fig. 51(b), is the significant and frequency-dependent phase shift. This will make the optimal cooling phase deviate from 90 or -90 degrees.

Figure 52 shows the circuit actually built. In the scope of this dissertation work, only three sets of filters are needed, for the three degrees of freedom.

E.9 FEEDBACK AND DRIVING CIRCUIT

Figures 53 and 54 show schematic and the photography, respectively, of the feedback and driving circuit.

This module features high current output of several amps (so, the limiting factor is the drive wire melting.) Also, with instrumentation amplifiers (INA121, Texas Instruments), external drive from, e.g., frequency synthesizer is combined with feedback signals for all directions. The electric loop for the driving current is very carefully engineered. With a dedicated power supply and ground loosely tied (through a 10 kΩ resistor) to the earth, the drive current does not return to the earth. This helps suppress the "feed-through" false signal being picked up by the PSD.

A 1 s high-pass filter helps reduce the DC offset signal from the Arduinos.

An output monitor tracks the voltage drop over the load resistor, also carefully ground-isolated with an instrumentation amplifier. This method monitors the actual current flow instead of the voltage output from the high-current op-amp, and can diagnose a broken loop due to, for example, a broken drive wire or a bad connection.

Relevant files:

- Magnetic-driving-with-ground-isolation_circuit_diagram.pdf, the circuit schematics.
- multiple_feedback_filter_control.py and multiple_feedback_filter_control.xml are the python codes and the user interface for the feedback drive. "multiple" stands for multiple degrees of freedom.

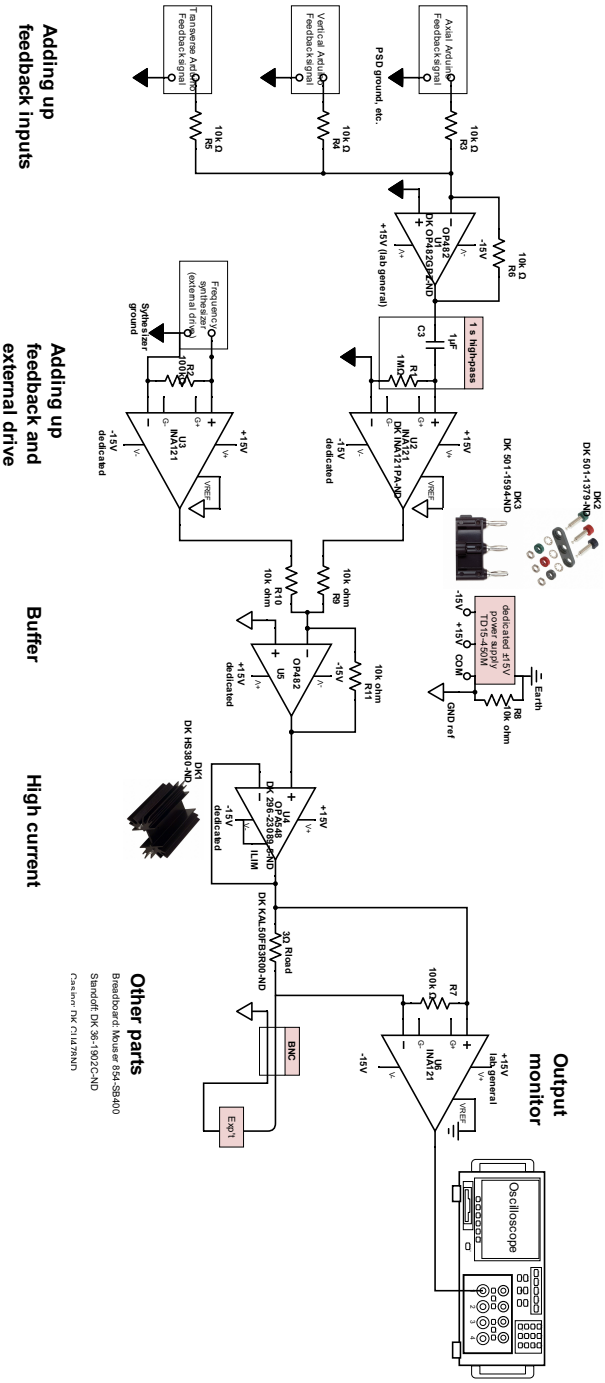

Figure 53: Schematic of the feedback and driving circuit. Note: All the power pins on integrated-circuit chips have bypass capacitors of 0.1 µF, unless otherwise noted. The pins of the bypass capacitors are to be as close to the power pins as possible, to minimize inductance from long leads. The capacitors should be ceramic ones, with temperature coefficients of C0G or NP0 when possible, or X7R.

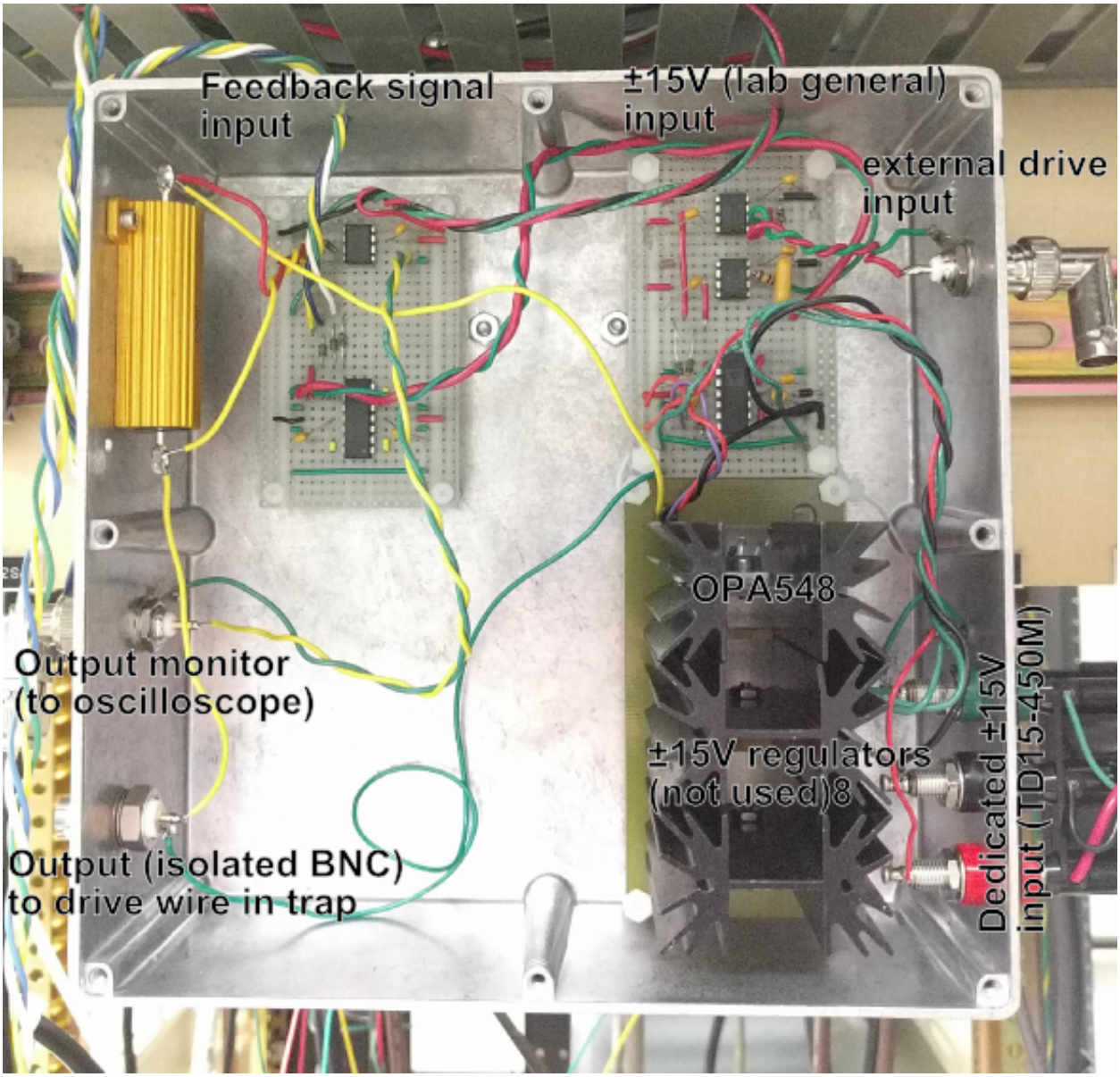

Figure 54: Photography of the feedback drive circuit.

E.10 GALVO

Figure 55 shows the schematic of the galvo control circuit, while Fig. 56 shows the actual built unit.

The purposes of the $20\ \Omega$ load resistor are one to limit the max current that can be drawn to ~ 0.5 A, the rated value for a single transducer (COM-10975, Sparkfun), while the equivalent resistance of each transducer is $\sim 4\ \Omega$.

Relevant files:

- galvo_scan_and_counter_w_PCBcounter_R2.ino has the Arduino code for galvo.
- spatial_scanning_interface_pythics_v0dot7dotx.py and spatial_scanning_interface_pythics_v0dot7dotx.html are the python script and the user interface for galvo.

E.11 GENERAL PURPOSE LED DRIVER

Figure 57 shows the schematic for a driving circuit for a LED light source.

E.12 SINGLE DROPLET GENERATOR

Relevant files:

- single_droplet_generator_design_1.dft, first design drawing for system.

Relevant parts already purchased:

- DK 668-1273-ND, piezo buzzer.
- MM 9464K79, #25 oring.

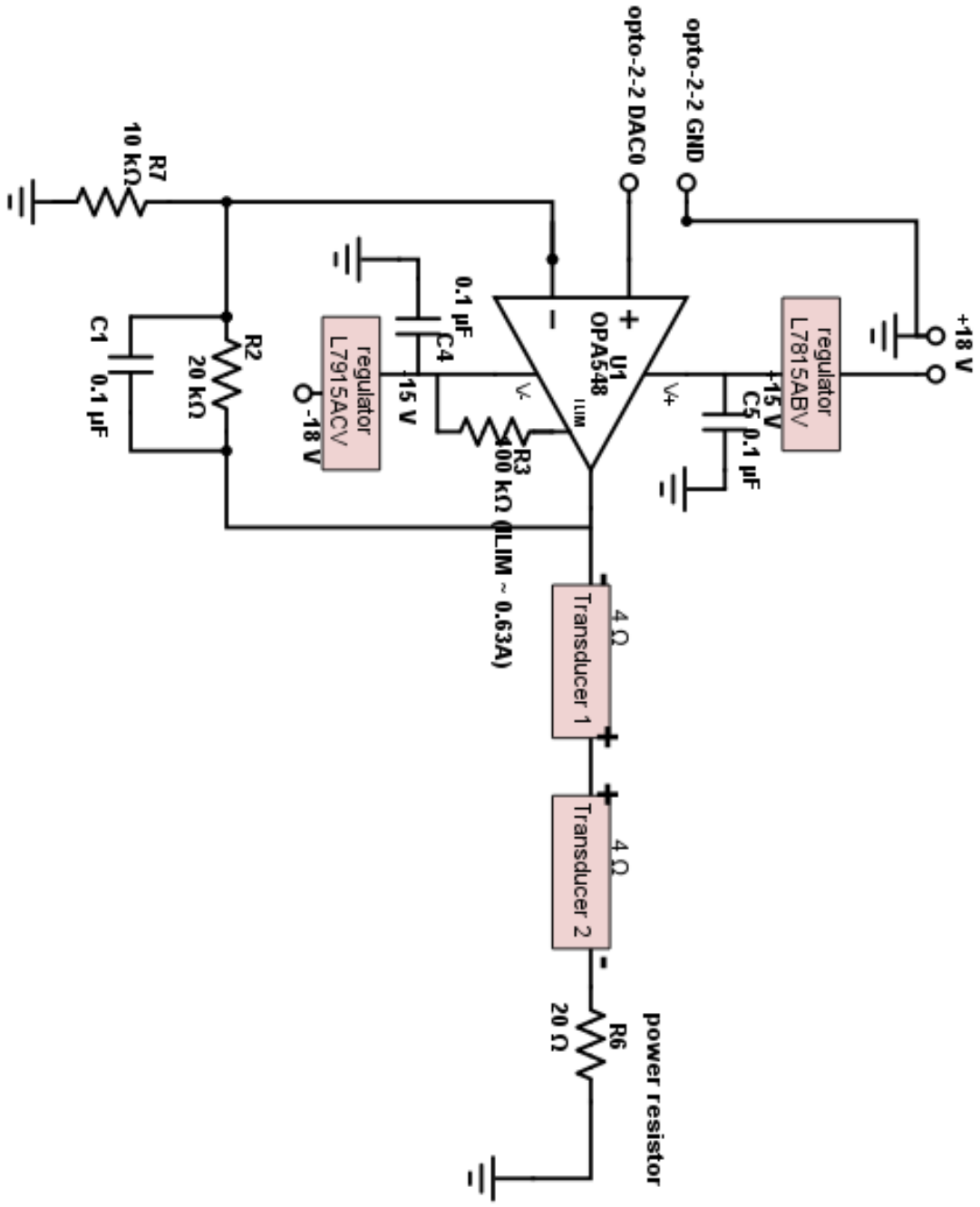

Figure 55: Schematic of the galvo control circuit. Note: All the power pins on integrated-circuit chips have bypass capacitors of 0.1 µF, unless otherwise noted. The pins of the bypass capacitors are to be as close to the power pins as possible, to minimize inductance from long leads. The capacitors should be ceramic ones, with temperature coefficients of C0G or NP0 when possible, or X7R.

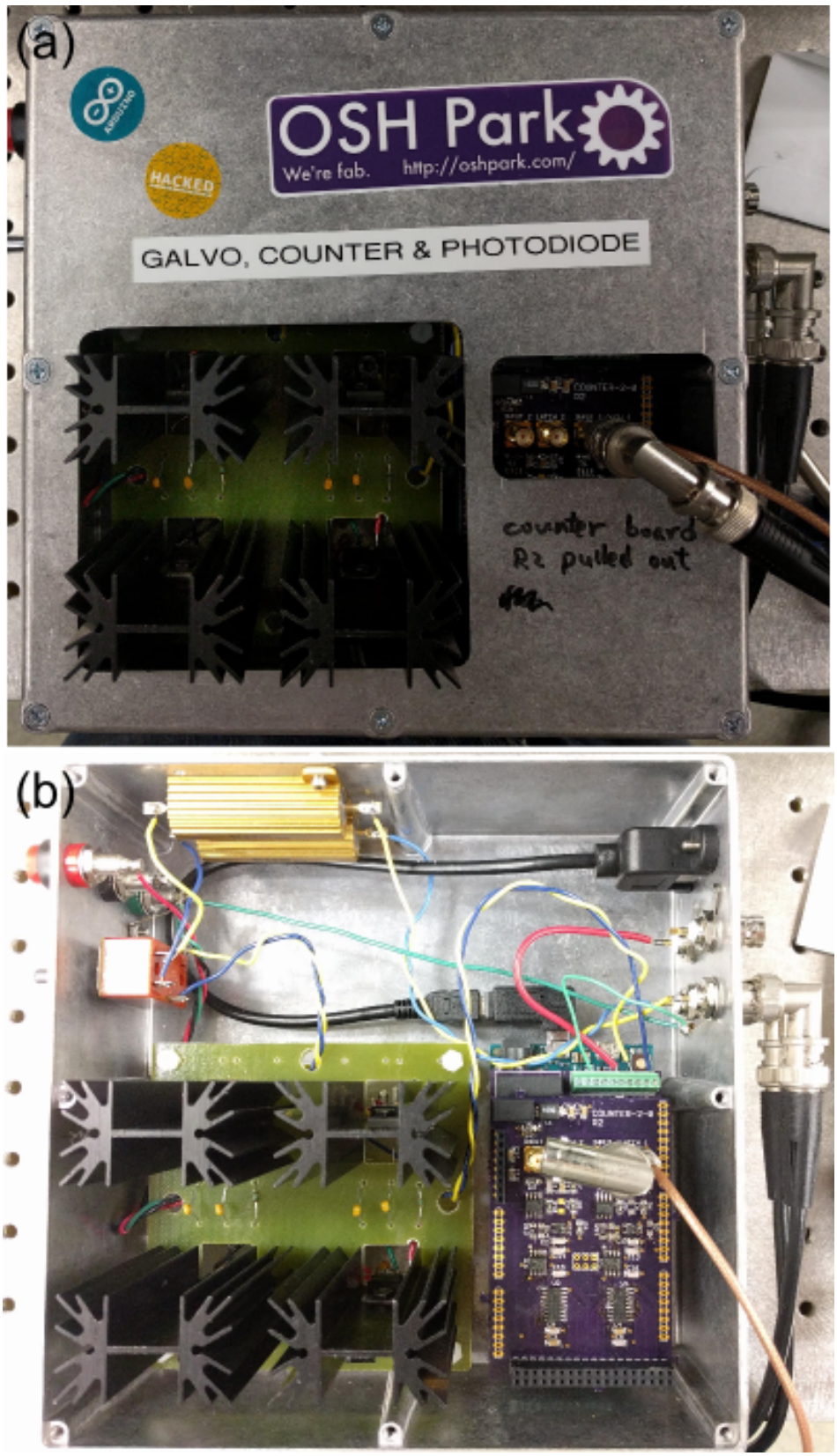

Figure 56: Photographys of the galvo circuit (a) with and (b) without the cover.

Figure 57: schematic for the driving circuit for a LED light source.

E.13 A NOTE FOR ELECTRONICS IMPROVEMENT

E.13.1 Voltage regulators L7815 and L7915

Ignored in most of the circuit designs documented above, but should have been taken care of, a load resistor is to pull a minimum load current for regulation. As required in the datasheets, a current of 5 mA should be drawn for the regulation to be reliable. Therefore, a dummy resistor of 15 V/0.005 mA $\approx 3000\ \Omega$ should be connected between the output and ground pins of the regulator, to ensure the baseline current.

E.13.2 Bandwidth Limiting

Another good practice that has not been employed for each circuit design is bandwidth limiting. Proper RC filtering should be implemented at each stage of amplification, according to the application frequency range. For example, in this dissertation work, a pass-band of 0 to 10 kHz is considered appropriate. The purpose of bandwidth limiting at each stage can prevent high frequency noises from each op-amp from propagating to the next stage, and eventually to the driving output to cause problems.

E.13.3 Grounding

A few points to be careful to in dealing with electronic grounding are summarized below:

1. Avoid ground loop.
2. The ground reference point is best to be defined at a single point, and connections are made in a radiating pattern from this ground point. This helps eliminate ground loop, too.
3. For an isolated loop (e.g., the feedback driving loop in this work) where the ground is not defined by the earth ground, the voltage in the loop can float to an arbitrary and dangerous point. A "loose" tie with the earth ground with a large resister, 1 or 10 MΩ, can help anchor the loop voltage down, but not drawing current between different grounds.

E.13.4 Electric Shielding

Electronic circuit boards should be shielded in metal boxes to avoid noises from external electric fields around, while the boxes are grounded. The signal wires between circuit boards should also be shielded by grounded jackets to minimize noise pick-up. When possible, a signal wire and a ground reference wire should be twisted together as much in the length as possible, to cancel the inductance in the wires.

APPENDIX F

ADC_DAC CODE

The key operations in the ADC_DAC.ino for the feedback loop are listed and explained.

In subroutine void ADC_to_DAC_bandpass_bw12_to_bw15(const int filter_shift):

- L3090 int32_t ch0 = (int16_t)ADC_current_buffer[ij] - ADC0_ZERO;
- L3122 c = ADC_sin_table[((ADC_phase_accumulator>>20)
  + ADC_SIN_TABLE_LENGTH/4) % ADC_SIN_TABLE_LENGTH];
- L3125 ADC_ch0_cos_stage1 = ((c * ch0)<<(filter_shift-11))
  + (((65536 - (1<<filter_shift)) * (int64_t)ADC_ch0_cos_stage1)>>16);
- L3144 in0_cos = ADC_ch0_cos_stage1 >> gain_shift;
- L3163 out0 = (user1*((in0_cos*(int64_t)c + in0_sin*(int64_t)s)>>15)
  + user2*((in0_sin*(int64_t)c - in0_cos*(int64_t)s)>>15))>>15;
- L3175 DAC_current_buffer[i] = ((out0>>4) + DAC0_ZERO) & DAC_OUTPUT_MSK;

L3090 The raw time series data department ADC_current_buffer[ij] department is shifted by the center value ADC0_ZERO (2048) to became centered around zero.

L3122 c is the table created for $\cos(\omega_{\mathrm{LO}}t)$, where ω_{LO} is the local oscillator frequency, that is, the user-set center frequency.

L3125 filter_shift is the user's bandwidth setting. ADC_ch0_cos_stage1 is in 32-bit, while the input date are in 12-bit (DUE) and c and s are in 16-bit. So, most of the shift operations are to switch between precisions. This line is analogous to an integrator, adding up past values with

a weight w:

$$\text{ADC\_ch0\_cos\_stage1} = \text{c} * \text{ch0} + w * \text{ADC\_ch0\_cos\_stage1}. \tag{F.1}$$

Electronically, an integrator is a low-pass filter. This is where the filtering is implemented. In programming, this particular implementation is called the infinite impulse response (IIR).

Here, the weight is

$$w = (65536 - (1<<\text{filter\_shift})). \tag{F.2}$$

The weight is in 16-bit, so 16-bit times 32-bit gives 48 bits. Therefore, this needs to be right shifted by 16 bits to get back to a 32-bit, thence the >>16 operation at the end of the line.

(c * ch0) is the actual mixing of the user-set center frequency $\omega_{\rm LO}$ and the supposed frequency ω_m of the signal $\cos(\omega_m t)$:

$$\cos(\omega_{\rm LO} t)\cos(\omega_m t) = (\omega_{\rm LO} - \omega_m)\text{part} + (\omega_{\rm LO} + \omega_m)\text{part}. \tag{F.3}$$

If $\omega_{\rm LO}$ is carefully "aimed" at the signal center frequency, the $(\omega_{\rm LO} - \omega_m)$ part is a mixed-down nearly-DC signal, while the $(\omega_{\rm LO} + \omega_m)$ part is the high frequency part that gets filtered out.

L3144 amplifies the signal. gain_shift is the user's Gain setting, in powers of 2.

L3163 in0_cos and in0_sin are the output of the lock-in amplifier, still down near DC. This line mxies the output back up. The user1 term represets the $\cos$ term being picked up by c, similarly for $\sin$. The user2 term is 90 degrees off, that $\sin$ term is picked up by c, similarly for $\cos$.

user1 and user2 together are determined by the Feedback Phase and the Feedback Amplitude (0-2.0 continuous) at the user end. Those allow setting the output amplitude and phase relative to the input.

Now the output is at the set LO frequency, which is set by the user and should be pretty close to the signal frequency. Further more, it is properly phase shifted according to the user's wish, e.g., 90 degrees off for feedback cooling or self-excitation.

L3175 shifts out0 from 16-bit to 12-bit, and the offset value is added back. Now the signal is ready to be sent out through the DUE DAC.

This routine continuously updates the output value at each data point. There is no "data frame" here. They are only in the python interface. The IF Filter Width label from 1 to 16 is

passed to ADC_DAC as filter_shift in the weight in the integrator, Eq. (F.2). So, the larger the bandwidth (BW) is, the smaller the weight. The smaller the BW in the frequency domain, the more heavily the output value is dependent on the past value, so slower to change in the time domain. The time scale is about 1/BW. So, the BW should be at least bigger than the natural damping rate, in order not to lose any signal. As a rule of thumb, if possible, the BW is set up to be as big as 1/10 of the center frequency. Otherwise, it is set to be as large as possible, before it runs into other peaks, or the 60/120 Hz power lines.

What this physically means to this experiment is that the larger the bandwidth, the faster the cooling output changes in response to the particle's motion, hence the higher cooling gain.

APPENDIX G

MOVIES OF PARTICLE THERMAL MOTIONS

Supplementary video V1 is an animated .gif file of the high-speed images of the trapped particle in the magneto-gravitational trap at 40 mTorr.

Supplementary video V2 shows the cooled motion of the same particle at high vacuum. The frame rate in the videos has been slowed by a factor of ten to improve visibility of the motion.

BIBLIOGRAPHY

[1] Original image: Archontis politis, real/complex spherical harmonic transform, gaunt coefficients and rotations http://se.mathworks.com/matlabcentral/fileexchange/43856-real-complex-spherical-harmonic-transform--gaunt-coefficients-and-rotations.

[2] Ch Monroe, DM Meekhof, BE King, and David J Wineland. A "schrödinger cat" superposition state of an atom. *Science*, 272(5265):1131, 1996.

[3] T Kovachy, P Asenbaum, C Overstreet, CA Donnelly, SM Dickerson, A Sugarbaker, JM Hogan, and MA Kasevich. Quantum superposition at the half-metre scale. *Nature*, 528(7583):530–533, 2015.

[4] Erwin Schrödinger. Die gegenwärtige situation in der quantenmechanik. *Naturwissenschaften*, 23(49):823–828, 1935.

[5] Zhang-qi Yin, Tongcang Li, Xiang Zhang, and LM Duan. Large quantum superpositions of a levitated nanodiamond through spin-optomechanical coupling. *Phys. Rev. A*, 88(3):033614, 2013.

[6] Matteo Scala, MS Kim, GW Morley, PF Barker, and S Bose. Matter-wave interferometry of a levitated thermal nano-oscillator induced and probed by a spin. *Phys. Rev. Lett.*, 111(18):180403, 2013.

[7] Andreas Albrecht, Alex Retzker, and Martin B Plenio. Testing quantum gravity by nanodiamond interferometry with nitrogen-vacancy centers. *Phys. Rev. A*, 90(3):033834, 2014.

[8] D Kafri, JM Taylor, and GJ Milburn. A classical channel model for gravitational decoherence. *New J. Phys.*, 16(6):065020, 2014.

[9] Richard P Feynman. There's plenty of room at the bottom. *Engineering and science*, 23(5):22–36, 1960.

[10] David P DiVincenzo et al. The physical implementation of quantum computation. *arXiv preprint quant-ph/0002077*, 2000.

[11] Thaddeus D Ladd, Fedor Jelezko, Raymond Laflamme, Yasunobu Nakamura, Christopher Monroe, and Jeremy L O'Brien. Quantum computers. *Nature*, 464(7285):45–53, 2010.

[12] D. Rugar, R. Budakian, H. J. Mamin, and B. W. Chui. Single spin detection by magnetic resonance force microscopy. *Nature*, 430(6997):329–332, July 2004.

[13] B Odom, D Hanneke, B D'Urso, and G Gabrielse. New measurement of the electron magnetic moment using a one-electron quantum cyclotron. *Physical Review Letters*, 97(3):030801, 2006.

[14] Mo Li, Hong X Tang, and Michael L Roukes. Ultra-sensitive nems-based cantilevers for sensing, scanned probe and very high-frequency applications. *Nature nanotechnology*, 2(2):114–120, 2007.

[15] Stephan Camerer, Maria Korppi, Andreas Jöckel, David Hunger, Theodor W Hänsch, and Philipp Treutlein. Realization of an optomechanical interface between ultracold atoms and a membrane. *Physical review letters*, 107(22):223001, 2011.

[16] Sungkun Hong, Michael S Grinolds, Patrick Maletinsky, Ronald L Walsworth, Mikhail D Lukin, and Amir Yacoby. Coherent, mechanical control of a single electronic spin. *Nano letters*, 12(8):3920–3924, 2012.

[17] SD Bennett, S Kolkowitz, QP Unterreithmeier, P Rabl, AC Bleszynski Jayich, JGE Harris, and Mikhail D Lukin. Measuring mechanical motion with a single spin. *New Journal of Physics*, 14(12):125004, 2012.

[18] Shimon Kolkowitz, Ania C Bleszynski Jayich, Quirin P Unterreithmeier, Steven D Bennett, Peter Rabl, JGE Harris, and Mikhail D Lukin. Coherent sensing of a mechanical resonator with a single-spin qubit. *Science*, 335(6076):1603–1606, 2012.

[19] Quantum ground state and single-phonon control of a mechanical resonator. *Nature*, 464(7289):697–703, April 2010.

[20] T Rocheleau, T Ndukum, C Macklin, JB Hertzberg, AA Clerk, and KC Schwab. Preparation and detection of a mechanical resonator near the ground state of motion. *Nature*, 463(7277):72–75, 2010.

[21] JD Teufel, Tobias Donner, Dale Li, JW Harlow, MS Allman, Katarina Cicak, AJ Sirois, Jed D Whittaker, KW Lehnert, and Raymond W Simmonds. Sideband cooling of micromechanical motion to the quantum ground state. *Nature*, 475(7356):359–363, 2011.

[22] Jasper Chan, TP Mayer Alegre, Amir H Safavi-Naeini, Jeff T Hill, Alex Krause, Simon Gröblacher, Markus Aspelmeyer, and Oskar Painter. Laser cooling of a nanomechanical oscillator into its quantum ground state. *Nature*, 478(7367):89–92, 2011.

[23] M Cirio, GK Brennen, and J Twamley. Quantum magnetomechanics: ultrahigh-q-levitated mechanical oscillators. *Phys. Rev. Lett.*, 109(14):147206, 2012.

[24] O Romero-Isart, L Clemente, C Navau, A Sanchez, and JI Cirac. Quantum magnetomechanics with levitating superconducting microspheres. *Phys. Rev. Lett.*, 109(14):147205, 2012.

[25] Remi Riviere, Samuel Deleglise, Stefan Weis, Emanuel Gavartin, Olivier Arcizet, Albert Schliesser, and Tobias J Kippenberg. Optomechanical sideband cooling of a micromechanical oscillator close to the quantum ground state. *Physical Review A*, 83(6):063835, 2011.

[26] ER MacQuarrie, M Otten, SK Gray, and GD Fuchs. Cooling a mechanical resonator with a nitrogen-vacancy center ensemble using a room temperature excited state spin-strain interaction. *arXiv preprint arXiv:1605.07131*, 2016.

[27] BC Barish and R Weiss. Ligo and the detection of gravitational waves. *Physics Today*, pages 44–50, 1999.

[28] BP Abbott, Richard Abbott, TD Abbott, MR Abernathy, Fausto Acernese, Kendall Ackley, Carl Adams, Thomas Adams, Paolo Addesso, RX Adhikari, et al. Observation of gravitational waves from a binary black hole merger. *Physical review letters*, 116(6):061102, 2016.

[29] Vladimir B Braginsky, Yuri I Vorontsov, and S Kip. Quantum nondemolit measureme. *Science*, 209:1, 1980.

[30] Darrick E Chang, CA Regal, SB Papp, DJ Wilson, J Ye, O Painter, H Jeff Kimble, and P Zoller. Cavity opto-mechanics using an optically levitated nanosphere. *Proc. Natl. Acad. Sci. U.S.A.*, 107(3):1005–1010, 2010.

[31] Tongcang Li, Simon Kheifets, and Mark G Raizen. Millikelvin cooling of an optically trapped microsphere in vacuum. *Nat. Phys.*, 7(7):527–530, 2011.

[32] Nikolai Kiesel, Florian Blaser, Uroš Delić, David Grass, Rainer Kaltenbaek, and Markus Aspelmeyer. Cavity cooling of an optically levitated submicron particle. *Proc. Natl. Acad. Sci. U.S.A.*, 110(35):14180–14185, 2013.

[33] Marcus W Doherty, Neil B Manson, Paul Delaney, Fedor Jelezko, Jörg Wrachtrup, and Lloyd CL Hollenberg. The nitrogen-vacancy colour centre in diamond. *Phys. Rep.*, 528(1):1–45, 2013.

[34] Ngoc Diep Lai, Dingwei Zheng, François Treussart, and Jean-François Roch. Optical determination and magnetic manipulation of a single nitrogen-vacancy color center in diamond nanocrystal. *Adv. Nat. Sci: Nanosci. Nanotechnol.*, 1(1):015014, 2010.

[35] Viva R Horowitz, Benjamín J Alemán, David J Christle, Andrew N Cleland, and David D Awschalom. Electron spin resonance of nitrogen-vacancy centers in optically trapped nanodiamonds. *Proc. Natl. Acad. Sci. U.S.A.*, 109(34):13493–13497, 2012.

[36] Levi P Neukirch, Jan Gieseler, Romain Quidant, Lukas Novotny, and A Nick Vamivakas. Observation of nitrogen vacancy photoluminescence from an optically levitated nanodiamond. *Opt. Lett.*, 38(16):2976–2979, 2013.

[37] Thai Hoang, Jonghoon Ahn, Jaehoon Bang, and Tongcang Li. Electron spin control of optically levitated nanodiamonds in vacuum. *Nature Communication*, 7(12250), 2016.

[38] ATMA Rahman, A Frangeskou, MS Kim, S Bose, GW Morley, and PF Barker. Burning and graphitization of optically levitated nanodiamonds in vacuum. *Sci. Rep.*, 2016.

[39] MD Simon and AK Geim. Diamagnetic levitation: flying frogs and floating magnets. *J. Appl. Phys.*, 87(9):6200–6204, 2000.

[40] IF Lyuksyutov, DG Naugle, and KDD Rathnayaka. On-chip manipulation of levitated femtodroplets. *Appl. Phys. Lett.*, 85(10):1817–1819, 2004.

[41] Christian Pigot, Hichem Chetouani, Guylaine Poulin, and Gilbert Reyne. Diamagnetic levitation of solids at microscale. *Magnetics, IEEE Transactions on*, 44(11):4521–4524, 2008.

[42] RJA Hill and L Eaves. Shape oscillations of an electrically charged diamagnetically levitated droplet. *Appl. Phys. Lett.*, 100(11):114106, 2012.

[43] Oki Gunawan, Yudistira Virgus, and Kong Fai Tai. A parallel dipole line system. *Appl. Phys. Lett.*, 106(6):062407, 2015.

[44] Jen-Feng Hsu, Peng Ji, Charles W Lewandowski, and Brian D'Urso. Cooling the motion of diamond nanocrystals in a magneto-gravitational trap in high vacuum. *Scientific reports*, 6:30125, 2016.

[45] Jen-Feng Hsu, Shonali Dhingra, Giriraj Jnawali, Mengchen Huang, Feng Bi, Lu Chen, Patrick Irvin, Chang-Beom Eom, Jeremy Levy, and D'Urso Brian. Patterning, transferring and suspension of single-layer graphene by deep-ultraviolet lithography with a single thin layer of poly(methyl methacrylate). *Not published*, 2015.

[46] Jen-Feng Hsu, Peng Ji, MV Dutt, and Brian R D'Urso. Loading an optical trap with diamond nanocrystals containing nitrogen-vacancy centers from a surface. *arXiv preprint arXiv:1506.08215*, 2015.

[47] Shonali Dhingra, Jen-Feng Hsu, Ivan Vlassiouk, and Brian D'Urso. Chemical vapor deposition of graphene on large-domain ultra-flat copper. *Carbon*, 69:188–193, 2014.

[48] Jen-Feng Hsu, Shonali Dhingra, and Brian D'Urso. Design and construction of a cost-efficient arduino-based mirror galvanometer system for scanning optical microscopy. *Submitted*, 2016.

[49] Mengchen Huang, Giriraj Jnawali, Jen-Feng Hsu, Shonali Dhingra, Hyungwoo Lee, Sangwoo Ryu, Feng Bi, Fereshte Ghahari, Jayakanth Ravichandran, Lu Chen, et al. Electric field effects in graphene/laalo3/srtio3 heterostructures and nanostructures. *APL materials*, 3(6):062502, 2015.

[50] Giriraj Jnawali, Mengchen Huang, Jen-Feng Hsu, Hyungwoo Lee, Patrick Irvin, Chang-Beom Eom, Brian D'Urso, and Jeremy Levy. Room-temperature quantum transport signatures in graphene/laalo3/srtio3 heterostructures. *arXiv preprint arXiv:1602.03128*, 2016.

[51] Jianan Li, Jen-Feng Hsu, Hyungwoo Lee, Shivendra Tripathi, Qing Guo, Lu Chen, Mengchen Huang, Shonali Dhingra, Jung-Woo Lee, Chang-Beom Eom, et al. Method for transferring

high-mobility cvd-grown graphene with perfluoropolymers. *arXiv preprint arXiv:1606.08802*, 2016.

[52] Robert Milo Wallace. *Scattering and Chemical Investigations of Semiconductor Surfaces.* PhD thesis, University of Pitsburgh, 1988.

[53] Pythics. http://www.nanomaterials.phyast.pitt.edu/pythics.html.

[54] Brian Richard D'Urso. *Cooling and self-excitation of a one-electron oscillator*. PhD thesis, Harvard University Cambridge, Massachusetts, 2003.

[55] Lowell S Brown and Gerald Gabrielse. Geonium theory: Physics of a single electron or ion in a penning trap. *Reviews of Modern Physics*, 58(1):233, 1986.

[56] Hans Dehmelt. Less is more: experiments with an individual atomic particle at rest in free space. *American Journal of Physics*, 58(1):17–27, 1990.

[57] Wolfgang Paul. Electromagnetic traps for charged and neutral particles. *Reviews of modern physics*, 62(3):531, 1990.

[58] H Winter and HW Ortjohann. Simple demonstration of storing macroscopic particles in a 'paul trap'. *Am. J. Phys*, 59(9):9, 1991.

[59] Dietrich Leibfried, Emanuel Knill, Signe Seidelin, Joe Britton, R Brad Blakestad, John Chiaverini, David B Hume, Wayne M Itano, John D Jost, Christopher Langer, et al. Creation of a six-atom schrödinger catstate. *Nature*, 438(7068):639–642, 2005.

[60] H Häffner, W Hänsel, CF Roos, J Benhelm, M Chwalla, T Körber, UD Rapol, M Riebe, PO Schmidt, C Becher, et al. Scalable multiparticle entanglement of trapped ions. *Nature*, 438(7068):643–646, 2005.

[61] Alec Jenkins. Trapping and cooling silica microspheres. 2013.

[62] A. Ashkin and J. M. Dziedzic. Optical levitation in high vacuum. *Appl. Phys. Lett.*, 28(6):333–335, 1976.

[63] A. Ashkin and J. M. Dziedzic. Feedback stabilization of optically levitated particles. *Appl. Phys. Lett.*, 30(4):202–204, 1977.

[64] A. Ashkin. Trapping of atoms by resonance radiation pressure. *Phys. Rev. Lett.*, 40:729–732, Mar 1978.

[65] S. De Nicola, A. Finizo, P. Mormile, G. Pierattini, S. Martellucci, J. Quartieri, F. Bloisi, and L. Vicari. Experimental results on the photophoretic motion and radiometric trapping of particles by irradiation with laser light. *Appl. Phys. B*, 47(3):247–250, 1988.

[66] Olga Jovanovic. Photophoresislight induced motion of particles suspended in gas. *J. Quant. Spectrosc. Ra.*, 110(11):889 – 901, 2009. Light Scattering: Mie and More Commemorating 100 years of Mie's 1908 publication.

[67] Vladlen G. Shvedov, Andrei V. Rode, Yana V. Izdebskaya, Anton S. Desyatnikov, Wieslaw Krolikowski, and Yuri S. Kivshar. Selective trapping of multiple particles by volume speckle field. *Opt. Express*, 18(3):3137–3142, Feb 2010.

[68] Ze Zhang, Drake Cannan, Jingjiao Liu, Peng Zhang, Demetrios N. Christodoulides, and Zhigang Chen. Observation of trapping and transporting air-borne absorbing particles with a single optical beam. *Opt. Express*, 20(15):16212–16217, Jul 2012.

[69] L. Cacciapuoti, M. de Angelis, G. Pierattini, and G.M. Tino. Single-beam optical bottle for cold atoms using a conical lens. *Eur. Phys. J. D*, 14(3):373–376, 2001.

[70] Vladlen G. Shvedov, Cyril Hnatovsky, Andrei V. Rode, and Wieslaw Krolikowski. Robust trapping and manipulation of airborne particles with a bottle beam. *Opt. Express*, 19(18):17350–17356, Aug 2011.

[71] Ioannis Chremmos, Peng Zhang, Jai Prakash, Nikolaos K. Efremidis, Demetrios N. Christodoulides, and Zhigang Chen. Fourier-space generation of abruptly autofocusing beams and optical bottle beams. *Opt. Lett.*, 36(18):3675–3677, Sep 2011.

[72] Yong-Le Pan, Steven C. Hill, and Mark Coleman. Photophoretic trapping of absorbing particles in air and measurement of their single-particle raman spectra. *Opt. Express*, 20(5):5325–5334, Feb 2012.

[73] A Turpin, V Shvedov, C Hnatovsky, Yu V Loiko, J Mompart, and W Krolikowski. Optical vault: A reconfigurable bottle beam based on conical refraction of light. *Optics express*, 21(22):26335–26340, 2013.

[74] Jan Gieseler, Bradley Deutsch, Romain Quidant, and Lukas Novotny. Subkelvin parametric feedback cooling of a laser-trapped nanoparticle. *Phys. Rev. Lett.*, 109(10):103603, 2012.

[75] Levi P Neukirch, Eva von Haartman, Jessica M Rosenholm, and A Nick Vamivakas. Multi-dimensional single-spin nano-optomechanics with a levitated nanodiamond. *Nat. Photonics*, 9(10):653–657, 2015.

[76] Thai Hoang, Jonghoon Ahn, Jaehoon Bang, and Tongcang Li. Electron spin control of optically levitated nanodiamonds in vacuum. *Bulletin of the American Physical Society*, 2016.

[77] Vijay Jain, Jan Gieseler, Clemens Moritz, Christoph Dellago, Romain Quidant, and Lukas Novotny. Direct measurement of photon recoil from a levitated nanoparticle. *arXiv preprint arXiv:1603.03420*, 2016.

[78] David E Pritchard. Cooling neutral atoms in a magnetic trap for precision spectroscopy. *Physical Review Letters*, 51(15):1336, 1983.

[79] M-O Mewes, MR Andrews, NJ Van Druten, DM Kurn, DS Durfee, and W Ketterle. Bose-einstein condensation in a tightly confining dc magnetic trap. *Physical Review Letters*, 77(3):416, 1996.

[80] L Hau et al. Photonic, electronic ans atomic collisions, edited by f. aumayr and h. winter, 1997.

[81] CJ Myatt, EA Burt, RW Ghrist, EA Cornell, and CE Wieman. Production of two overlapping bose-einstein condensates by sympathetic cooling. *Physical Review Letters*, 78(4):586, 1997.

[82] U Ernst, A Marte, F Schreck, J Schuster, and G Rempe. Bose-einstein condensation in a pure ioffe-pritchard field configuration. *EPL (Europhysics Letters)*, 41(1):1, 1998.

[83] Benjamin Deissler. *A Magnetic Trap for Evaporative Cooling of Rb Atoms*. PhD thesis, Citeseer, 2003.

[84] Samuel Earnshaw. On the nature of the molecular forces which regulate the constitution of the luminiferous ether. *Trans. Camb. Phil. Soc*, 7:97–112, 1842.

[85] J.D. Jackson. *Classical Electrodynamics*. Wiley, 1998.

[86] A.L. Fetter and J.D. Walecka. *Theoretical Mechanics of Particles and Continua*. Dover Books on Physics. Dover Publications, 2003.

[87] http://www.ansys.com/.

[88] Carpenter Technical Datasheet. Hiperco 50a alloy. url-http://cartech.ides.com/datasheet.aspx?i=103&e=199&c=TechArt, 2005.

[89] Tongcang Li. *Fundamental tests of physics with optically trapped microspheres*. Springer Science & Business Media, 2012.

[90] Boris V Derjaguin, Vladimir M Muller, and Yu P Toporov. Effect of contact deformations on the adhesion of particles. *Journal of Colloid and interface science*, 53(2):314–326, 1975.

[91] Lars-Oliver Heim, Jürgen Blum, Markus Preuss, and Hans-Jürgen Butt. Adhesion and friction forces between spherical micrometer-sized particles. *Physical Review Letters*, 83(16):3328, 1999.

[92] Robert R Perron. The design and application of a reliable ultrasonic atomizer. *Sonics and Ultrasonics, IEEE Transactions on*, 14(4):149–152, 1967.

[93] E James Davis and Asit K Ray. Determination of diffusion coefficients by submicron droplet evaporation. *The journal of chemical physics*, 67(2):414–419, 1977.

[94] Thomas E Daubert and Ronald P Danner. *Physical and Thermodynamic Properties of Pure Chemicals: Design institute for physical property data, American institute of chemical engineers. vp*. Hemisphere Publishing Corporation, 1989.

[95] M.J. O'Neil and Royal Society of Chemistry (Great Britain). *The Merck Index: An Encyclopedia of Chemicals, Drugs, and Biologicals*. Merck Index. Royal Society of Chemistry, 2013.

[96] T.E. Furia. *CRC Handbook of Food Additives, Second Edition*. Number v. 2. Taylor & Francis, 1980.

[97] Carl L Yaws. *Handbook of Thermal Conductivity, Volume 3:: Organic Compounds C8 to C28*, volume 3. Gulf Professional Publishing, 1995.

[98] W. Gerhartz and F. Ullmann. *Ullmann's encyclopedia of industrial chemistry*. Number v. 1 in Ullmann's Encyclopedia of Industrial Chemistry. VCH, 1987.

[99] Irwin T Lee, Sewan Fan, Valerie Halyo, Eric R Lee, Peter C Kim, Martin L Perl, Howard Rogers, Dinesh Loomba, Klaus S Lackner, and Gordon Shaw. Large bulk matter search for fractional charge particles. *Physical Review D*, 66(1):012002, 2002.

[100] Sewan Fan, Peter C Kim, Eric R Lee, Irwin T Lee, Martin L Perl, Howard Rogers, and Dinesh Loomba. A device for precision neutralization of electric charge of small drops using ionized air. *Review of scientific instruments*, 74(10):4305–4309, 2003.

[101] Ralph Howard Fowler and L Nordheim. Electron emission in intense electric fields. In *Proceedings of the Royal Society of London A: Mathematical, Physical and Engineering Sciences*, volume 119, pages 173–181. The Royal Society, 1928.

[102] Anne-Sophie Lucier. *Preparation and characterization of tungsten tips suitable for molecular electronics studies*. PhD thesis, McGill University, 2004.

[103] T. L. Van Well, M. Redshaw, N. D. Gamage, and R. M. E. B. Kandegedara. Electrochemical etching and characterization of sharp field emission points for electron impact ionization. *J. Vis. Exp.*, 113:e54030, 2016.

[104] AA Sickafoose, JE Colwell, M Horányi, and S Robertson. Photoelectric charging of dust particles in vacuum. *Physical review letters*, 84(26):6034, 2000.

[105] B Grob, H Burtscher, and R Niessner. Charging of ultra-fine aerosol particles by an ozone-free indirect uv photo-charger. *Aerosol Science and Technology*, 47(12):1325–1333, 2013.

[106] Kuang-Chao Fan, Jhih-Yuan Chen, Ching-Hua Wang, and Wen-Chueh Pan. Development of a drop-on-demand droplet generator for one-drop-fill technology. *Sensors and Actuators A: Physical*, 147(2):649–655, 2008.

[107] JC Yang, W Chien, M King, and WL Grosshandler. A simple piezoelectric droplet generator. *Experiments in fluids*, 23(5):445–447, 1997.

[108] Shane R Hawke. *Effects of a thin, flexible nozzle on droplet formation and impingement*. PhD thesis, 2006.

[109] Barry Michael Cornella, Sean Sawyer Hammerland, and Shawn Laabs. On-demand droplet generation. *URJ-UCCS: Undergraduate Research Journal at UCCS*, 2(2):30–38, 2009.

[110] Hamamatsu s5980 si pin photodiode datasheet. https://www.hamamatsu.com/resources/pdf/ssd/s5980_etc_kpin1012e.pdf.

[111] D Allan, T Caswell, N Keim, and C van der Wel. trackpy 0.3.0. https://github.com/soft-matter/trackpy, 2015.

[112] John C Crocker and David G Grier. Methods of digital video microscopy for colloidal studies. *J. Colloid Interface Sci.*, 179(1):298–310, 1996.

[113] Simon F Nørrelykke and Henrik Flyvbjerg. Harmonic oscillator in heat bath: Exact simulation of time-lapse-recorded data and exact analytical benchmark statistics. *Phys. Rev. E*, 83(4):041103, 2011.

[114] Introduction to fourier transform on mathematica http://mathworld.wolfram.com/FourierTransform.html.

[115] Trevor King. Thermal cantilever calibration http://www.physics.drexel.edu/~wking/rsrch/papers/cantilever_calib/cantilever_calib.pdf. 2009.

[116] S.T. Thornton and J.B. Marion. *Classical Dynamics of Particles and Systems*.

[117] Python fft implementation details http://docs.scipy.org/doc/numpy/reference/routines.fft.html#module-numpy.fft.

[118] Gerhard Heinzel, Albrecht Rüdiger, and Roland Schilling. Spectrum and spectral density estimation by the discrete fourier transform (dft), including a comprehensive list of window functions and some new at-top windows. 2002.

[119] Paul S Epstein. On the resistance experienced by spheres in their motion through gases. *Phys. Rev.*, 23(6):710, 1924.

[120] SA Beresnev, VG Chernyak, and GA Fomyagin. Motion of a spherical particle in a rarefied gas. part 2. drag and thermal polarization. *J. Fluid Mech.*, 219:405–421, 1990.

[121] Ngoc Diep Lai, O Faklaris, D Zheng, V Jacques, HC Chang, JF Roch, and F Treussart. Quenching nitrogen–vacancy center photoluminescence with an infrared pulsed laser. *New J. Phys.*, 15(3):033030, 2013.

[122] Wayne M Itano, JC Bergquist, JJ Bollinger, and DJ Wineland. Cooling methods in ion traps. *Physica Scripta*, 1995(T59):106, 1995.

[123] D Wineland and Hans Dehmelt. Proposed 1014 delta upsilon less than upsilon laser fluorescence spectroscopy on t1+ mono-ion oscillator iii. In *Bulletin of the American Physical Society*, volume 20, pages 637–637. AMER INST PHYSICS CIRCULATION FULFILLMENT DIV, 500 SUNNYSIDE BLVD, WOODBURY, NY 11797-2999, 1975.

[124] Theodor W Hänsch and Arthur L Schawlow. Cooling of gases by laser radiation. *Optics Communications*, 13(1):68–69, 1975.

[125] David J Wineland, Robert E Drullinger, and Fred L Walls. Radiation-pressure cooling of bound resonant absorbers. *Physical Review Letters*, 40(25):1639, 1978.

[126] Claude Cohen-Tannoudji. Laser cooling and trapping of neutral atoms: theory. *Physics reports*, 219(3):153–164, 1992.

[127] DJ Heinzen and DJ Wineland. Quantum-limited cooling and detection of radio-frequency oscillations by laser-cooled ions. *Physical Review A*, 42(5):2977, 1990.

[128] JMW Milatz, JJ Van Zolingen, and BB Van Iperen. The reduction in the brownian motion of electrometers. *Physica*, 19(1-12):195–202, 1953.

[129] J-M Courty, Antoine Heidmann, and Michel Pinard. Quantum limits of cold damping with optomechanical coupling. *EPJ D*, 17(3):399–408, 2001.

[130] B Rodenburg, LP Neukirch, AN Vamivakas, and M Bhattacharya. Quantum model of cooling and force sensing with an optically trapped nanoparticle. *Optica*, 3(3):318–323, 2016.

[131] M Hamdi and W. Y. Aribah. Probability density for a classical harmonic oscillator.

[132] Brian Lantz, Peter Fritschel, Haisheng Rong, Ed Daw, and Gabriela González. Quantum-limited optical phase detection at the 10^{-10}-rad level. *JOSA A*, 19(1):91–100, 2002.

[133] Alexei Ourjoumtsev, Hyunseok Jeong, Rosa Tualle-Brouri, and Philippe Grangier. Generation of optical 'schrödinger cats' from photon number states. *Nature*, 448(7155):784–786, 2007.

[134] Zaki Leghtas, Steven Touzard, Ioan M Pop, Angela Kou, Brian Vlastakis, Andrei Petrenko, Katrina M Sliwa, Anirudh Narla, Shyam Shankar, Michael J Hatridge, et al. Confining the state of light to a quantum manifold by engineered two-photon loss. *Science*, 347(6224):853–857, 2015.

[135] Carlton M Caves, Kip S Thorne, Ronald WP Drever, Vernon D Sandberg, and Mark Zimmermann. On the measurement of a weak classical force coupled to a quantum-mechanical oscillator. i. issues of principle. *Reviews of Modern Physics*, 52(2):341, 1980.

[136] Roberto Onofrio and Alessandro Rioli. Quantum nondemolition stroboscopic scheme for coupled harmonic oscillators. *Physical Review D*, 47(6):2176, 1993.

[137] B D'Urso, MV Gurudev Dutt, S Dhingra, and NM Nusran. Quantum measurements between a single spin and a torsional nanomechanical resonator. *New Journal of Physics*, 13(4):045002, 2011.

[138] Shonali Dhingra. *Quadratic coupling between a classical nanomechanical oscillator and a single spin*. PhD thesis, University of Pittsburgh, 2015.

[139] L Cacciapuoti, M De Angelis, G Pierattini, and GM Tino. Single-beam optical bottle for cold atoms using a conical lens. *The European Physical Journal D-Atomic, Molecular, Optical and Plasma Physics*, 14(3):373–376, 2001.

[140] DuPont. Summary of properties for kapton polyimide films http://www.dupont.com/content/dam/dupont/products-and-services/membranes-and-films/polyimde-films/documents/DEC-Kapton-summary-of-properties.pdf.

[141] Terry Quinn. Fundamental constants: measuring big g. *Nature*, 408(6815):919–921, 2000.

[142] Thorlabs. Ldc205c manual. https://www.thorlabs.com/thorcat/15900/LDC205C-Manual.pdf, 20165.